2008

A High-resolution Storm Surge Model For The Pascagoula Region, Mississippi

Naeko Takahashi
University of Central Florida

A HIGH-RESOLUTION STORM SURGE MODEL FOR THE PASCAGOULA REGION, MISSISSIPPI

by

NAEKO TAKAHASHI
B.S. Chuo University, JAPAN, 2001

A thesis submitted in partial fulfillment of the requirements
for the degree of Master of Science
in the Department of Civil, Environmental and Construction Engineering
in the College of Engineering and Computer Science
at the University of Central Florida
Orlando, Florida

Fall Term
2008

ABSTRACT

The city of Pascagoula and its coastal areas along the United States Gulf Coast have experienced many catastrophic hurricanes and were devastated by high storm surges caused by Hurricane Katrina (August 23 to 30, 2005). The National Hurricane Center reported high water marks exceeding 6 meters near the port of Pascagoula with a near 10-meter high water mark recorded near the Hurricane Katrina landfall location in Waveland, MS. Although the Pascagoula River is located 105 km east of the landfall location of Hurricane Katrina, the area was devastated by storm surge-induced inundation because of its low elevation.

Building on a preliminary finite element mesh for the Pascagoula River, the work presented herein is aimed at incorporating the marsh areas lying adjacent to the Lower Pascagoula and Escatawpa Rivers for the purpose of simulating the inland inundation which occurred during Hurricane Katrina. ADCIRC-2DDI (ADvanced CIRCulation Model for Shelves, Coasts and Estuaries, Two-Dimensional Depth Integrated) is employed as the hydrodynamic circulation code. The simulations performed in this study apply high-resolution winds and pressures over the 7-day period associated with Hurricane Katrina. The high resolution of the meteorological inputs to the problem coupled with the highly detailed description of the adjacent inundation areas will provide an appropriate modeling tool for studying storm surge dynamics within the Pascagoula River. All simulation results discussed herein are directed towards providing for a full

accounting of the hydrodynamics within the Pascagoula River in support of ongoing flood/river forecasting efforts.

In order to better understand the hydrodynamics within the Pascagoula River when driven by an extreme storm surge event, the following tasks were completed as a part of this study:

1) Develop an inlet-based floodplain DEM (Digital Elevation Model) for the Pascagoula River. The model employs topography up to the 1.5-meter contour extracted from the Southern Louisiana Gulf Coast Mesh (SL15 Mesh) developed by the Federal Emergency Management Agency (FEMA).

2) Incorporate the inlet-based floodplain model into the Western North Atlantic Tidal (WNAT) model domain, which consists of the Gulf of Mexico, the Caribbean Sea, and the entire portion of the North Atlantic Ocean found west of the 60 degree West meridian, in order to more fully account for the storm surge dynamics occurring within the Pascagoula River. This large-scale modeling approach will utilize high-resolution wind and pressure fields associated with Hurricane Katrina, so that storm surge hydrographs (elevation variance) at the open-ocean boundary locations associated with the localized domain can be adequately obtained.

3) Understand the importance of the various meteorological forcings that are attributable to the storm surge dynamics that are setup within the Pascagoula River. Different

implementations of the two model domains (large-scale, including the WNAT model domain; localized, with its focus concentrated solely on the Pascagoula River) will involve the application of tides, storm surge hydrographs and meteorological forcing (winds and pressures) in isolation (i.e., as the single forcing mechanism) and collectively (i.e., together in combination).

The following conclusions are drawn from the research presented in this thesis: 1) Incorporating the marsh areas into the preliminary in-bank mesh provides for significant improvement in the astronomic tide simulation; 2) the large-scale modeling approach (i.e., the localized floodplain mesh incorporated into the WNAT model domain) is shown to be most adequate towards simulating storm surge dynamics within the Pascagoula River. Further, we demonstrate the utility of the large-scale model domain towards providing storm surge hydrographs for the open-ocean boundary of the localized domain. Only when the localized domain is forced with the storm surge hydrograph (generated by the large-scale model domain) does it most adequately capture the full behavior of the storm surge. Finally, we discover that while the floodplain description up to the 1.5-m contour greatly improves the model response by allowing for the overtopping of the river banks, a true recreation of the water levels caused by Hurricane Katrina will require a floodplain description up to the 5-m contour.

ACKNOWLEDGMENTS

As I finalized my work at the University of Central Florida, I realized that I am blessed with invaluable support. First of all, I am sincerely grateful to Dr. Scott C. Hagen for directing me throughout the process of this graduate research and for his invaluable suggestions. In addition, I appreciate his patience and understanding during my time as a member of the CHAMPS (Coastal Hydrodynamics, Analysis, Modeling and Predictive Simulations) Laboratory. I would also like to thank Drs. Manoj Chopra and Gour-Tsyh Yeh for agreeing to serve on my committee. I have also experienced the joy of learning and understanding science and engineering in their classrooms, and this will continue to help me in my career as an engineer. Also, I would like to emphasize that this thesis is a collaborative effort with Qing Wang who has been working with me on this project. I am thankful for her intelligence and friendship over the past two years.

Further, I gratefully acknowledge the help of all of current members in CHAMPS Lab: Peter Bacopoulos for overseeing my studies with his qualified suggestions. His participation allowed us to overcome and learn from the many obstacles that Qing and I encountered in completing this work. He also helped me to improve my English skills since I first joined the lab as an ESOL student; Stephen Medeiros for sharing his knowledge as a professional engineer and serving as my thesis editor; David Coggin, Derek Giardino, Alfredo Ruiz, and Hitoshi Tamura. I wish them success in their academics and bright futures after they graduate. I also thank former lab members, Yuji

Funakoshi, Michael Parrish, Mike Salisbury, and Satoshi Kojima, for their additional advice.

I extend special thanks to Mr. David Welch, Mr. Dave Reed and Mr. Dave Ramirez of the Lower Mississippi River Forecast Center for their cooperation in providing the cross sectional data and background papers that were used in the preparation of this project.

Last but not least, I am very grateful to my parents for allowing me to study abroad. My family (especially my newborn niece) and friends always cheer me up. Without the generous thoughts of these individuals, this investigation would not have been possible.

This research was funded in part by award NA04NWS4620013 from the National Oceanic and Atmospheric Administration (NOAA), U.S. Department of Commerce. The statements, findings, conclusions and recommendations are those of the author and do not necessarily reflect those of the NOAA, the Department of Commerce and its affiliates.

TABLE OF CONTENTS

LIST OF FIGURES

LIST OF TABLES

LIST OF ABBREVIATIONS

1D	One Dimensional
2D	Two Dimensional
ADCIRC-2DDI	Advanced Circulation Model for Oceanic, Coastal, and Estuarine Waters (Two-Dimensional, Depth-Integrated Option)
CPP	Carte Parallelogrammatique Project
DEM	Digital Elevation Model
FEMA	Federal Emergency Management Agency
FIRM	Flood Insurance Rate Map
GIS	Geographic Information System
GPS	Global Positioning System
GWCE	Generalized Wave Continuity Equation
LMRFC	Lower Mississippi River Forecast Center
LTEA	Localized Truncation Error Analysis
MEOW	Maximum Envelope of Water
NAVD 88	North American Vertical Datum of 1988
NOAA	National Oceanic and Atmospheric Administration
NOS	National Ocean Service
RMS	Root Mean Square
SLOSH	Sea, Lake and Overland Surges from Hurricanes model
SMS	Surface-water Modeling System
USGS	United States Geological Survey

CHAPTER 1. INTRODUCTION

Disaster prediction and protection has been recognized as one of the most important and critical issues in today's world since natural disasters such as earthquakes, floods, and hurricanes impact our lives and economies. Therefore, the nation's emergency management systems must be capable of handling and preparing future regional master plans, insurance plans, and emergency evacuation plans. It is the duty of civil engineers and scientists to provide reliable resources and solutions to assist in this effort to serve the public good.

This study presents simulated storm surges for the Pascagoula River, located in lower Mississippi along the Gulf of Mexico, caused by Hurricane Katrina (2005). The Pascagoula River is located 105 km east of the landfall location of Hurricane Katrina; despite the distance from the eye of the storm, the area was inundated by an approximate 5-meter storm surge due to its vast low-lying coastal plain. The majority of the fatalities in Mississippi (reported as 238; Knabb et al., 2005) were directly caused by the storm surge. This study is motivated by the absence of an existing model that can accurately describe storm tide propagation up the Pascagoula River and over its banks into the adjacent floodplains. All research presented herein is directed towards providing for a full accounting of the hydrodynamics within the Pascagoula River in support of ongoing flood/river forecasting efforts.

The University of Central Florida is cooperating with the Hydrology Laboratory of the NWS Office of Hydrologic Development and the Lower Mississippi River Forecast

Center (LMRFC) to develop a two-dimensional storm tide model for the Pascagoula River. The major goals of this overall project are to: 1) include the Pascagoula River in a modification of an existing model domain encompassing the entire east coast of the United States, Gulf of Mexico and Caribbean Sea such that astronomic tides and storm surge can be accurately modeled; 2) develop localized domain for the Pascagoula River that will produce results comparable to the large-scale domain from Goal 1. This research will result in a model that more completely accounts for the hydraulic conditions in flood forecasts and flood forecast mapping in the study area.

Recently, as the first report of this project, Wang (2008) has presented a preliminary finite element model domain for the Pascagoula River, which is capable of accurately describing the hydrodynamics of the astronomic tides within the banks of the Pascagoula River (Figure 1.1). This portion of the study concluded that: 1) the comprehensive Pascagoula River model domain is able to reproduce the hydrodynamics for in-bank flow driven by astronomic tides; 2) the tides propagate up the river system to Graham Ferry, 55 km (34.5 miles) upstream from the inlets. To expand on the in-bank mesh used by Wang (2008), it is presented in this thesis the refinement of the comprehensive model domain to include the inundation areas, mainly those contained within the Lower Pascagoula and Escatawpa regions. This floodplain model domain will then be applied in tidal and storm surge simulations in order to investigate the role of the inundation areas in tidally driven processes and storm surge dynamics in the Pascagoula River. Additional experimentation with the floodplain model domain will realize knowledge of the tidal and meteorological forcings and their influence on the local system response.

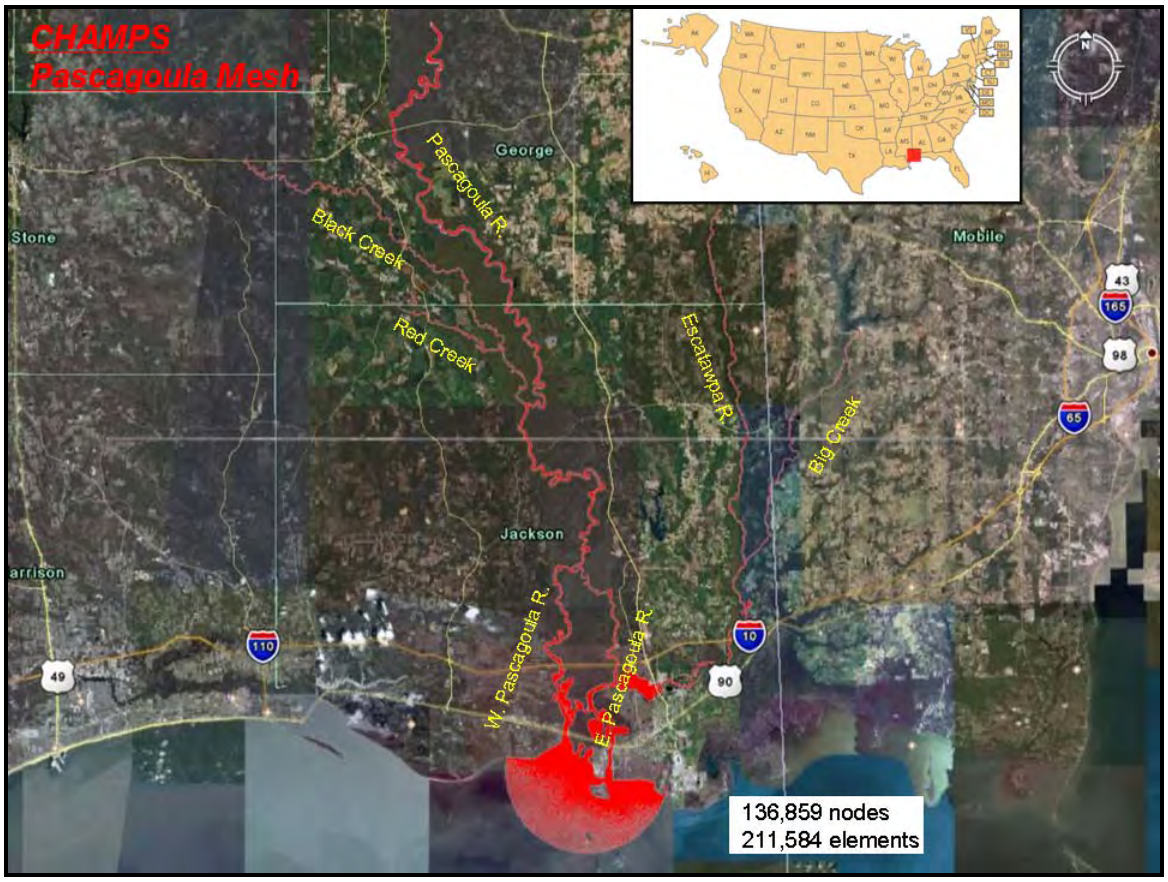

Figure 1.1 Comprehensive Pascagoula River Mesh (shown in red) overlaid on aerial photography of the region (image courtesy of Google Earth).

Therefore, as the second report of this project, three major objectives have been completed:

1) Develop a Pascagoula floodplain model domain that includes the inundation areas up to the 1.5-meter NAVD88 contour.

2) Incorporate the Pascagoula floodplain model domain in the Western North Atlantic Tidal (WNAT) model domain (Figure 1.2), which encompasses the entire east coast of the United States, Gulf of Mexico and Caribbean Sea, such that astronomic tides and storm surge can be simulated using a large-domain modeling approach.

3) Apply the large-scale (WNAT-based) and local-scale (inlet-based) model domains in a variety of tidal and storm surge simulations. Different implementations of the two model domains will involve the application of tides, storm surge hydrographs and meteorological forcing (winds and pressures) in isolation (i.e., as the single forcing mechanism) and collectively (i.e., together in combination). The knowledge gained from these experiments will yield knowledge of the forcing mechanisms for the Pascagoula River and the manner in which they are incorporated into a numerical model.

The study presented herein provides storm surge simulation results and floodplain mapping values for the Pascagoula River that are valuable to many applied modeling efforts for various topics. This study serves as a thesis in partial fulfillment of the requirements for a Master of Science degree in Civil Engineering at the University of Central Florida in the fall semester 2008. The project as a whole is in pursuit of an operational forecasting model for the Pascagoula region that was conducted in conjunction with LMRFC. The computations were performed in the UCF CHAMPS Laboratory.

1.1 Advanced Circulation Model

Astronomic and meteorological tides are calculated using the ADCIRC-2DDI (ADvanced CIRCulation Model for Shelves, Coasts and Estuaries, Two-Dimensional Depth Integrated) hydrodynamic circulation code (Westerink, Blain, Luettich, & Scheffner, 1994). This finite element based model solves the shallow water equations in their full nonlinear form. It can be forced with elevation boundary conditions, flux boundary conditions, and tidal potential terms, all of which result in the full simulation of astronomic tides. In addition, dynamic wind fields for a given hurricane or tropical storm event (e.g. Hurricane Katrina) are converted to spatially variable and time-dependent wind surface stresses and then incorporated into the ADCIRC-2DDI model along with atmospheric pressure variations that permit for the simulation of a storm surge. Further, the ADCIRC-2DDI model allows for wetting and drying of nearshore and inland elements to simulate flood inundation and recession.

ADCIRC-2DDI solves the linear algebraic equations that result from the finite element discretization of the GWCE (Generalized Wave Continuity Equation) formulation using pre-conditioned conjugate gradient solvers. The number of iterations required per time step is very low and the computational cost in terms of CPU and memory increase linearly with the number of nodes. This allows the application of grids with very large numbers of nodes. To further enhance the computational capability of ADCIRC-2DDI, a parallel version has been developed and is installed on multiple high performance computing clusters in the UCF CHAMPS Laboratory.

1.2 The WNAT (Western North Atlantic Tidal) Model Domain

Previous efforts by Hagen et al. (2006) have resulted in the development of a finite element mesh for tidal computations in the Western North Atlantic Tidal (WNAT) model domain. The model domain consists of the Gulf of Mexico, the Caribbean Sea, and the entire portion of the North Atlantic Ocean found west of the 60 degree West meridian (Figure 1.2). The finite element mesh was developed using node spacing guidelines generated from a Localized Truncation Error Analysis (LTEA) (Hagen et al. 1998). The high resolution mesh contains 332,582 computational modes and 647,018 triangular elements (WNAT-333K) with node spacings of 1.0 to 25 km. Consequently, the model is capable of a highly accurate simulation; however, it requires approximately 13 days to complete a full 90-day simulation (on a twelve-node cluster of 600 MHz processors running in parallel), which is not appropriate for a real-time simulation. To resolve this issue, studies applied LTEA and resulted in a mesh constructed of 52,774 computational nodes and 98,365 triangular elements (WNAT-53K) (Hagen et al., 2005), satisfying the modeling accuracy and computational efficiency requirements. Additionally, the time step used in a simulation on this domain has been increased from 5 seconds to 30 seconds, enhancing the computational efficiency of the model.

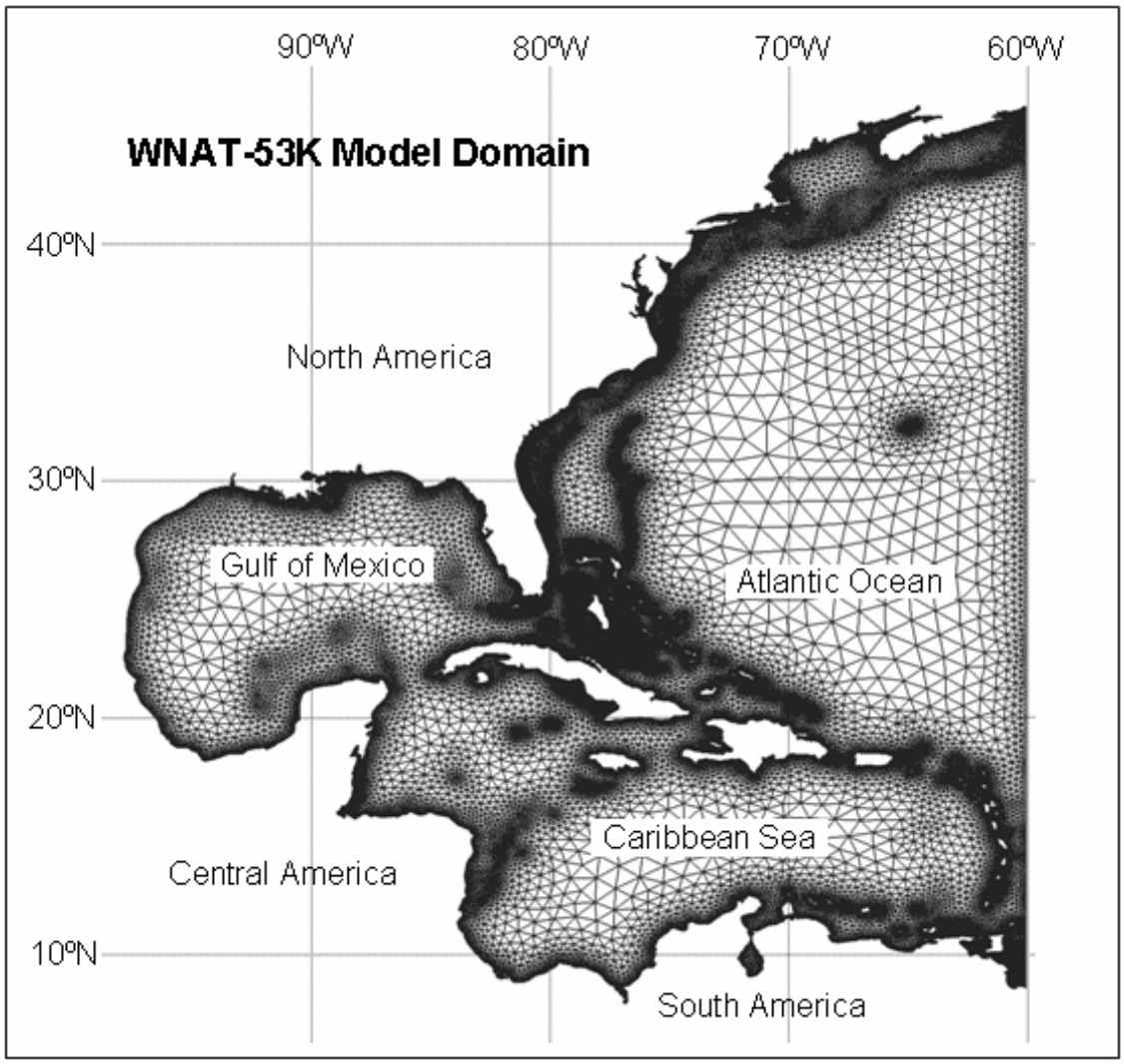

Figure 1.2 WNAT-53K Model Domain

Table 1.1 WNAT-53K Mesh Properties

Domain Area	8.347×10^6 km^2
Computational Nodes	52,774
Triangular Elements	98,365
Minimum Node Spacing	0.5 km
Maximum Node Spacing	160 km
Boundary Spacing	6.0 km
Boundary Nodes	7,111

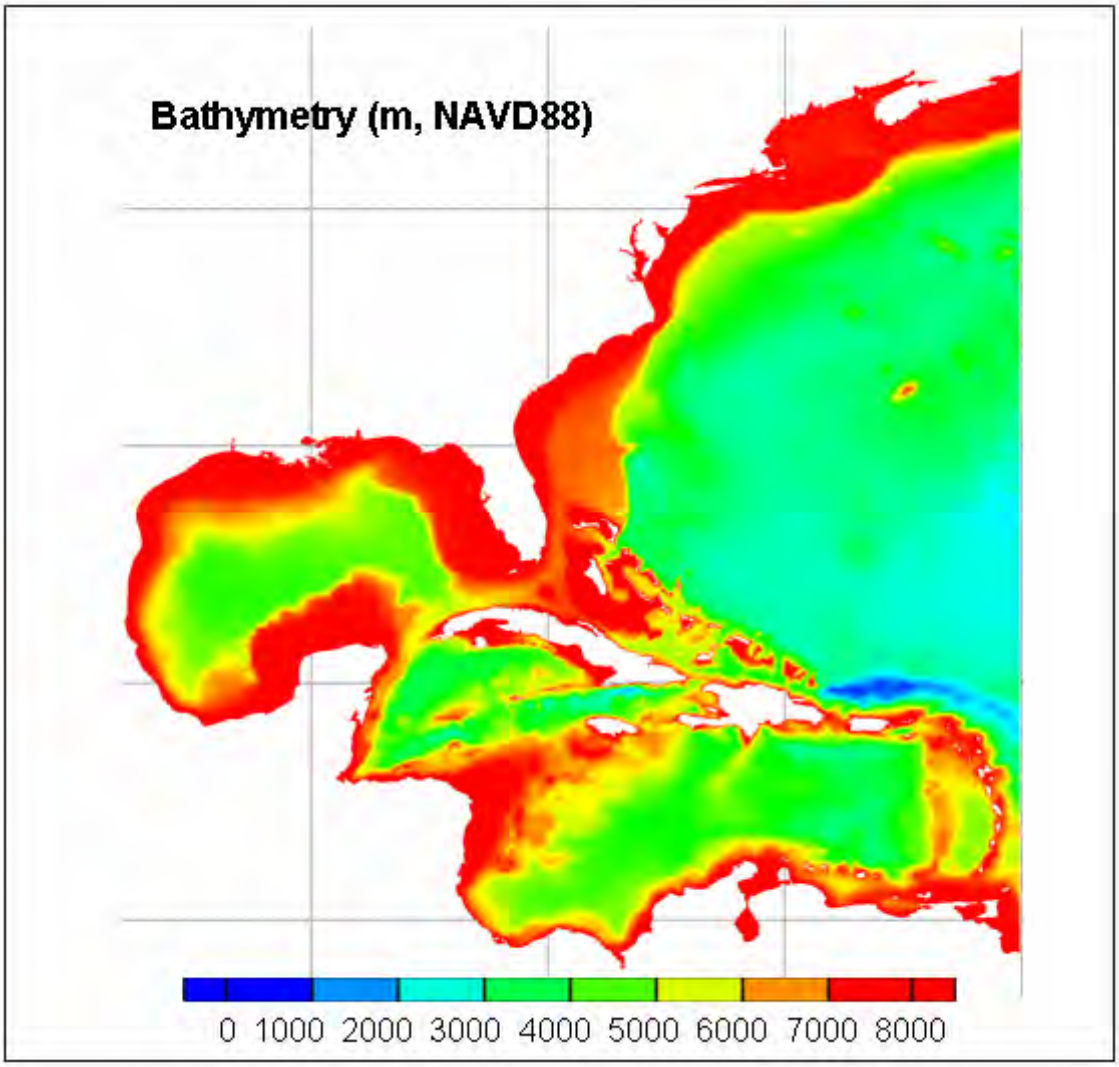

Figure 1.3 WNAT-53K Model Bathymetry Contours. Positive values represent depths below NAVD88

1.3 The Pascagoula River

The Pascagoula River drains the Pascagoula Basin located in the southeastern region of the State of Mississippi. The Pascagoula Basin has a drainage area of about 25,000 km^2 (9700 mi^2) and contains the Pascagoula River and its two principal tributaries: the Chickasawhay River and Leaf River (Figure 1.4). The Chickasawhay drains 7,700 km^2 (2,970 mi^2) in the northeastern part of the basin, and the Leaf drains 9,280 km^2 (3,580 mi^2) in the northwestern part of the basin. From the confluence of the two tributaries, near Gage MRRM6 in Merrill, MS, the Pascagoula River stretches southward connecting to the Mississippi Sound and Gulf of Mexico through the swampy lands in George and Jackson Counties. The topography of the Pascagoula Basin is generally rolling with low to moderate relief. The highest elevation in the northern part of the Chickasawhay is more than 180 m (600 ft).

The Pascagoula River consists of two inlet systems, the East Pascagoula and West Pascagoula, and several tributaries: the Black Creek, Red Creek, Escatawpa River and Big Creek. Since the river is shallow, slow-moving, and with low slope, it spreads out to a wide cross-section for much of its course, and the river can be influenced by tides from the Gulf of Mexico as far north as 55 km (34.5 miles) inland, just south of the Graham Ferry (Gage PGFM6 in Figure 1.4). The extremely slow flow of the river makes it difficult for pollutants to be flushed from the waters, which has become a serious issue for the local environment. Therefore, there have been many conservation and research projects to address this issue. In recent years, many hurricanes and tropical storms have

affected Mississippi; for instance, the city of Pascagoula experienced severe flooding damage by the storm surge during the 2005 hurricane season.

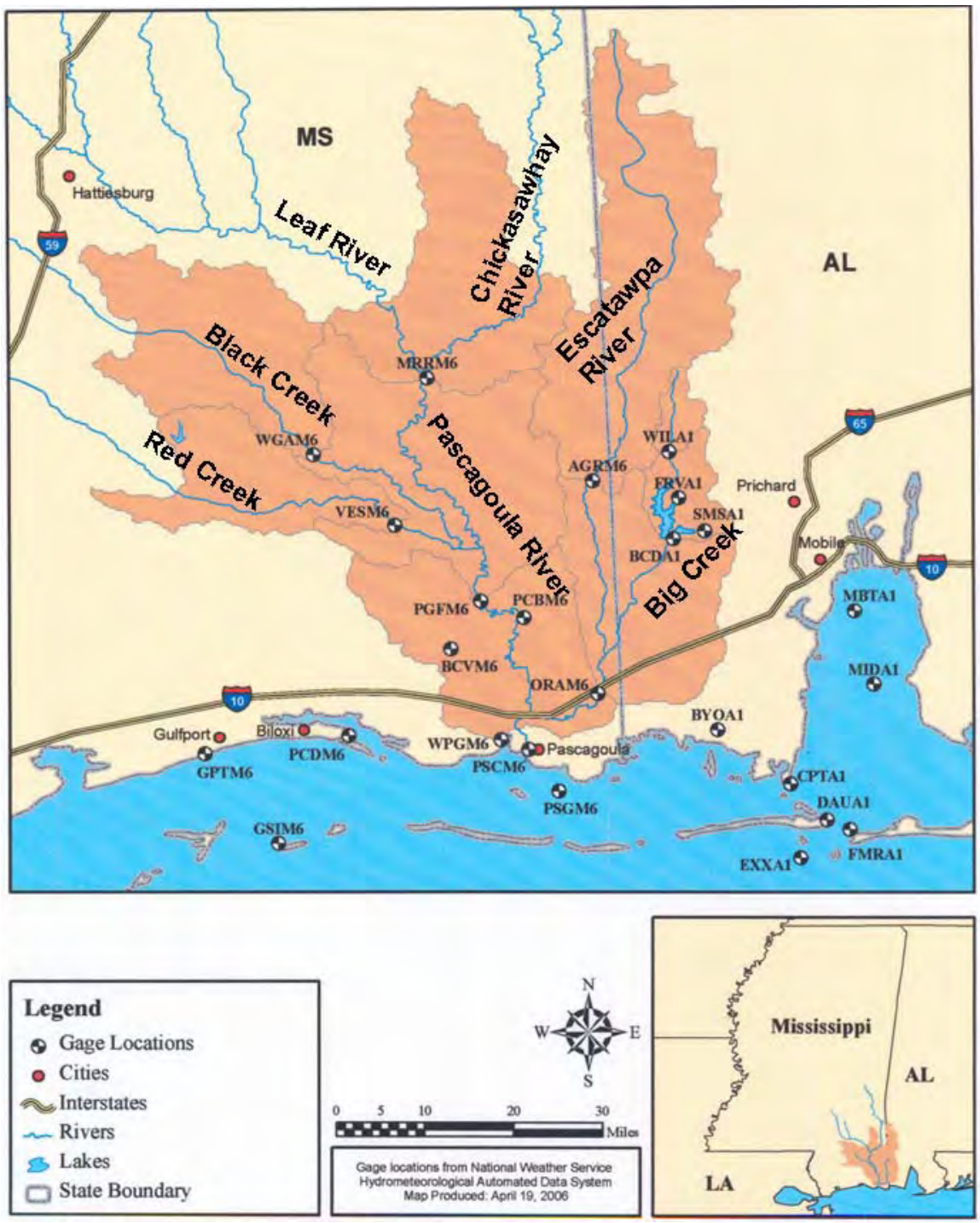

Figure 1.4 Study Area and Gages in Lower Pascagoula
(Original image was provided by the LMRFC)

1.4 Hurricane Katrina

Hurricane Katrina was the costliest hurricane to impact the coast of the United States during the past 100 years, reaching Category 5 (APPENDIX A for Saffir-Simpson Scale) strength during the 2005 Atlantic hurricane season. This devastating hurricane made three landfalls in the U.S. (Figure 1.5) between August 23 to 30 before being downgraded to a tropical depression near Clarksville, TN, causing severe destruction and huge loss of life across the entire northern Gulf Coast (southeast Louisiana to Florida Panhandle, through the states of Mississippi and Alabama). According to the Tropical Cyclone Report (Knabb et al., National Hurricane Center, 2005), Hurricane Katrina caused $40.6 billion in insured losses as estimated by the American Insurance Services Group (AISG) and a preliminary estimate of the total damage has risen to about $81 billion. The total number of fatalities attributed to the storm rose to 1,833 (including those both directly and indirectly related to Katrina). This includes 238 deaths in Mississippi, the majority of which was directly caused by the storm surge; 1,577 in Louisiana where the loss of life and property damage occurred as a direct result of widespread storm-surge flooding and its aftermath in New Orleans; 14 in Florida; 2 in Georgia; 2 in Alabama. Also, several hundred residents of the impacted communities are still listed as missing.

1.4.1 History of the Storm

The best track of Hurricane Katrina is illustrated in Figure 1.5 (Knabb, NHC, 2005) beginning on August 23, 2005 when the storm was classified as a tropical depression about 175 miles south of Nassau, Bahamas. At 2330 UTC (Coordinated Universal Time) on August 25, the storm made its first landfall near Miami-Dade, FL as a Category 1

hurricane, and then it crossed the Florida Peninsula causing fatalities and damage as it moved west. On August 26, the strength of the storm decreased to a tropical storm while over land; however it continued moving into the Gulf of Mexico, and Katrina intensified again to a Category 2 hurricane later that day.

The formation of the storm changed considerably from August 28 to 29 as it approached the northern Gulf Coast. During this period, the hurricane force winds extended out to 125 miles from the center and the tropical storm force winds were observed 230 miles away from the eye. The peak intensity on August 28 resulted in a minimum central pressure 902 mb (this was the sixth most intense hurricane based on central pressure in the Atlantic basin from 1851 to 2005) and maximum sustained winds of 175 mph, making Katrina a Category 5 hurricane. According to the National Data Buoy Center (NDBC), buoy station 42040, located at 29°11'03"N, 88°12'48"W, approximately 118 km (64 nautical miles) south of Dauphin Island Alabama (Figure 1.7), reported a significant wave height of 16.91 m (55.5 ft) at 1100 UTC, August 29 (Figure 1.8). Noting that the maximum wave height may be statistically approximated by 1.9 times the significant wave height (World Meteorological Organization, 1998), the maximum wave height would be 32.1 m (105 ft).

Katrina became an extraordinarily intense hurricane with a maximum (1-minute sustained) wind speed 127 mph and a minimum central pressure of 920 mb at the second landfall at 1110 UTC on August 29, at Buras in Plaquemines Parish, LA, which was the third lowest landfalling pressure on record. At this landfall, the storm was at Category 3

strength with wind speed significantly reduced; however, the storm surge maintained the level close to that of a Category 5 hurricane.

Maintaining Category 3 strength with its maximum wind speed at 120 mph and the minimum central pressure at 928 mb, Katrina moved ashore near the Louisiana and Mississippi border and made the its final landfall at about 0000 UTC on August 29, near mouth of the Pearl River, in Pearlington, MS. Moving inland over southern and central Mississippi, Katrina weakened to Category 1 by 1800 UTC, August 29, finally turning into a tropical depression near Tennessee Valley, TN. Besides the devastation caused by winds and storm surges, even after it became a tropical depression, Katrina went on to produce 62 tornadoes in 8 states along with high rainfall, which caused immense losses. In fact, wind gusts of 80 to 110 mph were observed well inland over southeastern and central Mississippi.

1.4.2 Reported High Water Marks

Even though Katrina had weakened from Category 5 to Category 3 after the previous day's landfall at Buras, LA, the staggering storm surges ravaged the coastline along the northern Gulf of Mexico, on an area that is particularly vulnerable to storm surge. This is attributable to the massive size of the storm during its time at Category 5 intensity. Due to the large wind field, the Category 5 (or 4) storm caused extensive wave setup along the northern Gulf Coast prior to landfall. As shown in the previous section, buoy 42040 recorded 9.1 m (30 ft) significant wave height as early as 0000 UTC 29 August and 16.91 m (55.5 ft) significant wave height at 1100 UTC. Katrina's massive storm surge was

produced by the total water level being further increased by waves, including those generated the previous day when Katrina was a Category 5 hurricane (Figure 1.8). Furthermore, buoy station 42007 located at 30°5'25" N 88°46'7" W, 41 km (22 nautical miles) from the coastline (Figure 1.7) recorded the maximum significant wave height of 5.64 m (the maximum wave height can be 10.73 m) (Figure 1.8). Soon afterward, the station broke its mooring and went adrift.

Fritz et al. (2008) illustrated Katrina's storm surge height in comparison with Hurricane Camille (1969) at the major cities along the Gulf Coast (Figure 1.10). It is noted that the storm surge was relatively high to the east of the Katrina's path, near and including our main interest, the Pascagoula region along with Mobile Bay which experienced nearly twice the storm surge height than during Camille. Although the city of Pascagoula is located about 105 km (65 miles) away from the landfall location and lower winds and storm surge were expected, the relatively low elevation of the town enabled for the severe storm surge flooding. APPENDIX B presents the complete high water mark database gathered during the survey, excluding additional transect and shoreline points. It indicates that the Pascagoula region received a 5.80 to 6.30 m storm surge according to vertical survey, and cites that inland water marks of 57.7 to 92.2 m were observed. Like many areas along the Mississippi coastline, this area was completely flooded except for small high ground areas next to Interstate 10 (about 10 km north of the port of Pascagoula) (Figure 1.11 and Figure 1.12). On the west, storm surge ran up the river estuary, with the bayous of Gautier receiving maximum water levels of 4.6 m, and the communities along the river such as Gautier and Vancleave were also extensively flooded. Furthermore, on

the east side, flooding was far-reaching up the Escatawpa River. Cities of Moss Point and Escatawpa received from 2.7 to 4.3 m of storm surge. The city of Moss Point is surrounded by water: the Gulf of Mexico to the south, the Pascagoula River estuary to the west, the Escatawpa River to the north, and various bayous and areas of protected marshland to the east. Further to the east, areas that are known to flood in just a heavy rainstorm, such as Grand Bay, Alabama, received extensive flooding as well.

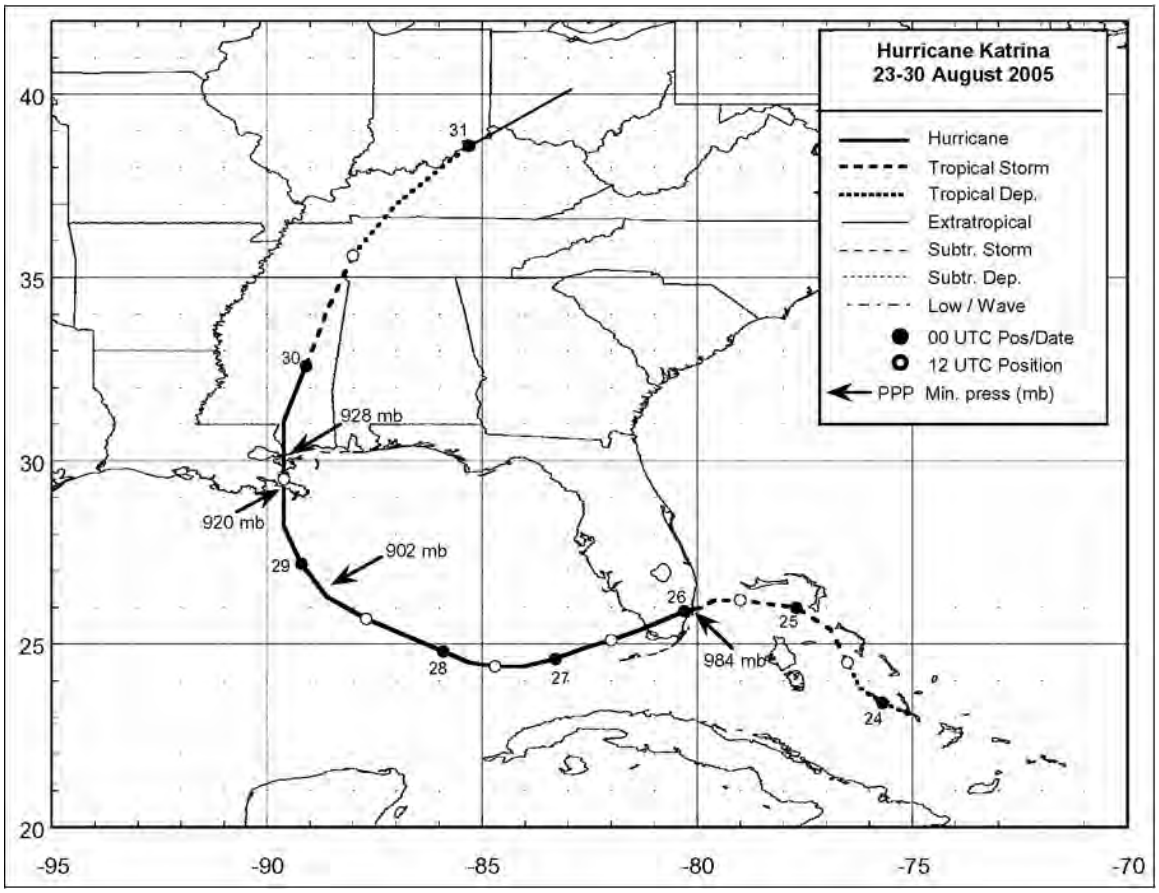

Figure 1.5 Best Track Position for Hurricane Katrina, 23-30 August 2005

Figure 1.6 Hurricane Katrina Track: Zoomed in the Gulf shoreline

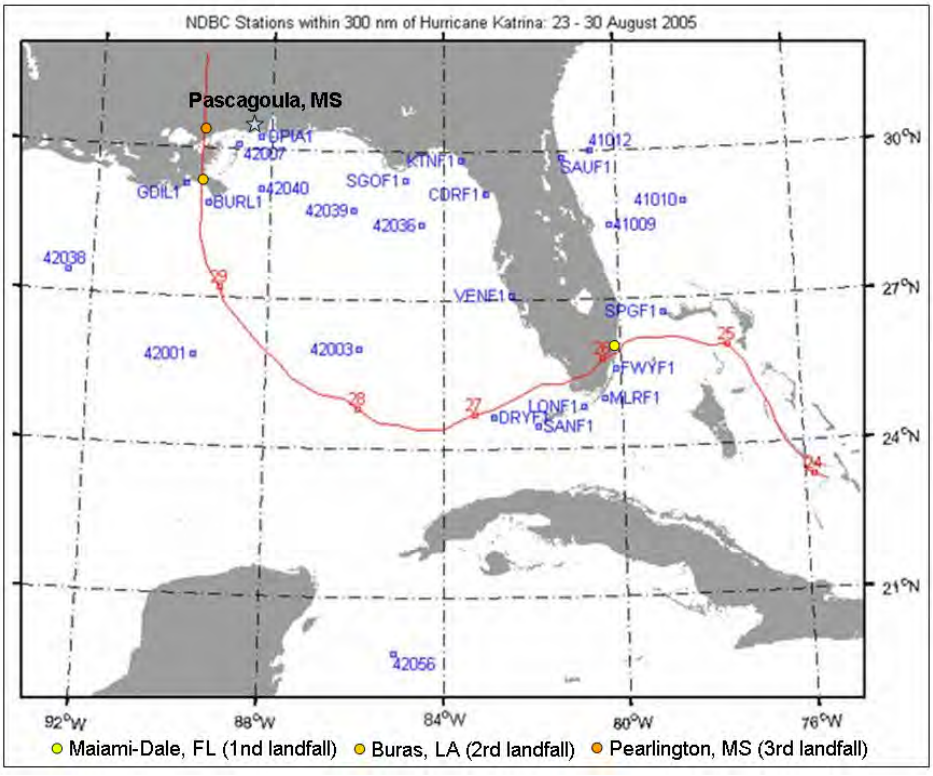

Figure 1.7 NDBC Stations and Hurricane Katrina's Track (in red with the start of each day numbered)

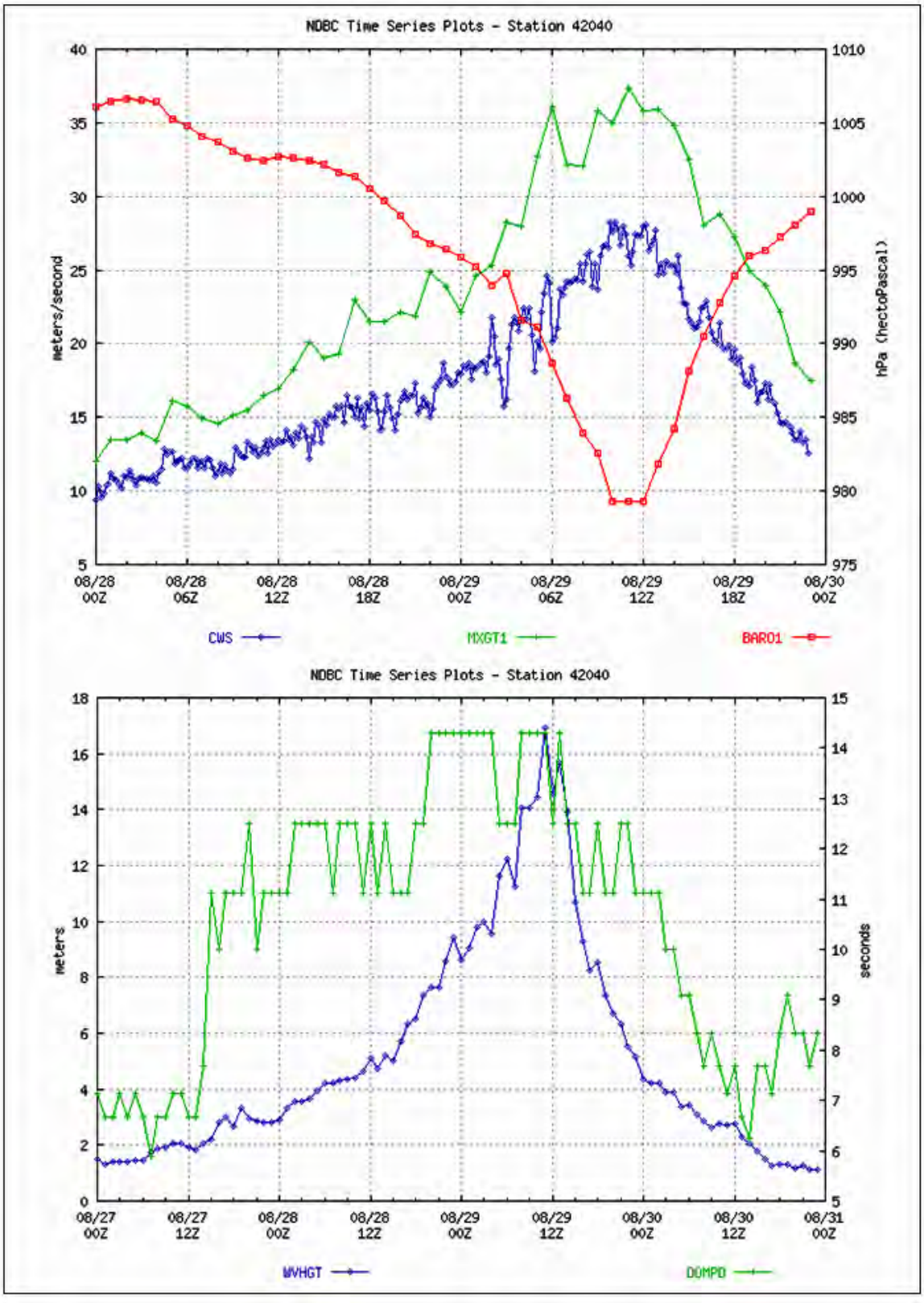

Figure 1.8 NDBC Station 42040: (Top) Winds (Anemometer Height 5m) and Sea-level Pressure/ (Bottom) Significant Wave Height and Dominant Period

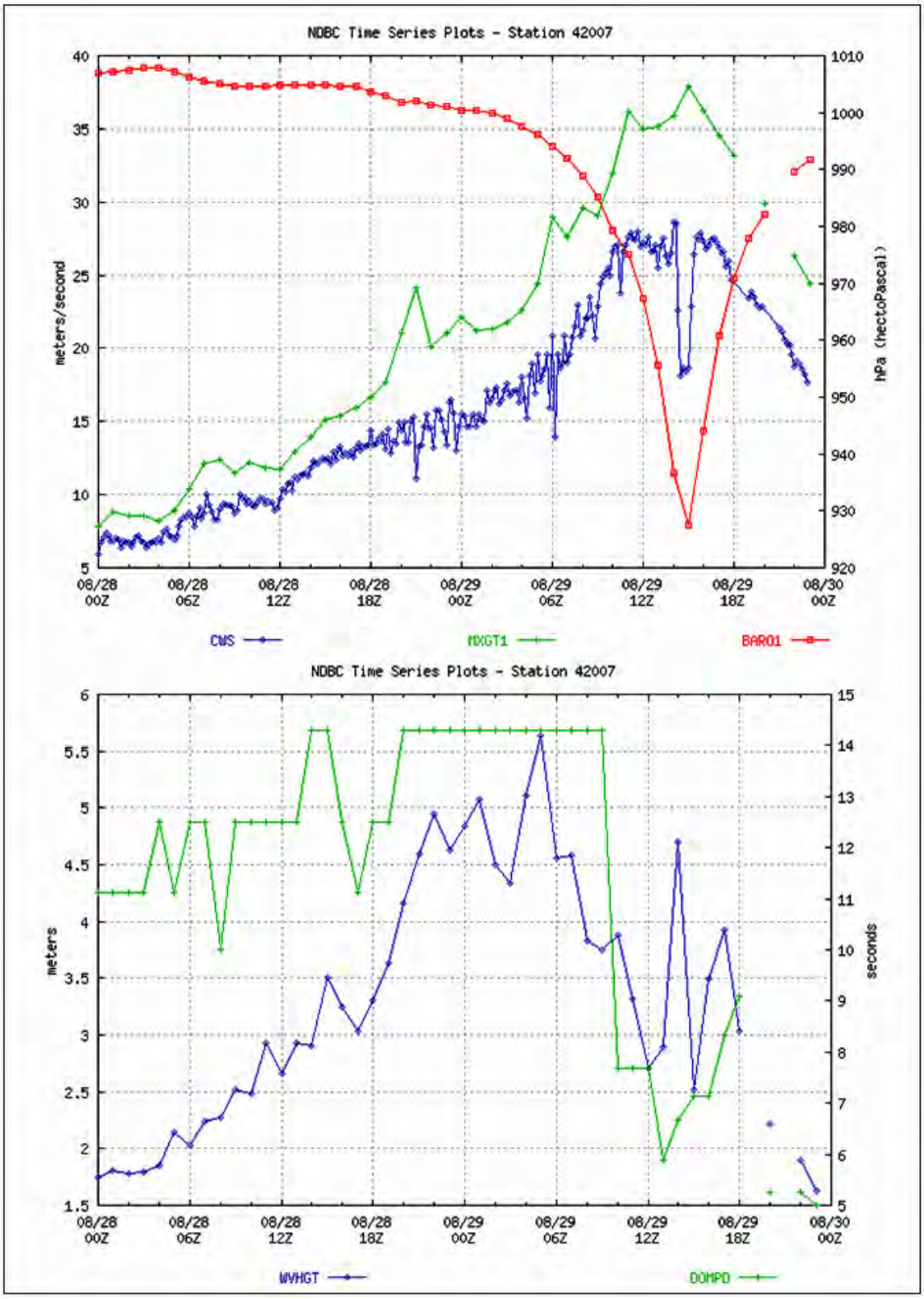

Figure 1.9 NDBC Station 42007: (Top) Winds (Anemometer Height 5m) and Sea-level Pressure/ (Bottom) Significant Wave Height and Dominant Period

Table 1.2 Legend for Figure 1.8 and Figure 1.9

CWS	The average wind speed over a 10-minute period at the anemometer height.
MXGT1	The Peak 5-second gust during the past hour at the anemometer height.
BAR01	The Average Sea-level Pressure over 8-minutes.
WVHGT	The significant wave height that represents the average of the highest one-third of the waves during the wave sampling period.
DOMPD	The Dominant Period that represents the wave period (time from between consecutive passes of the wave crests) of the waves with the most energy.

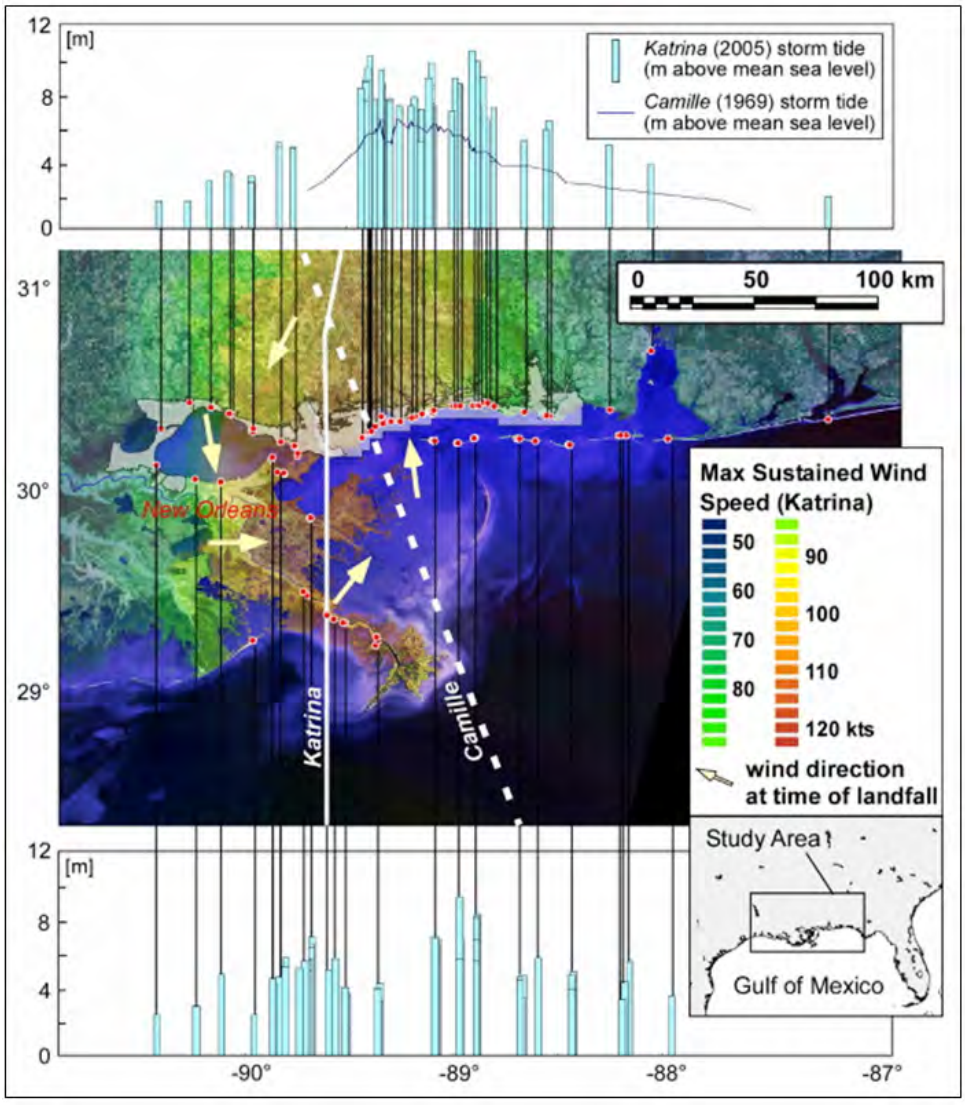

Figure 1.10 Hurricane Katrina (2005) storm surge height measurements and Hurricane Camille (1969) high water mark profile (Fritz, 2008)

Figure 1.11 Foods in Pascagoula, MS over 1/2 mile inland (Weather Underground, Inc)


Figure 1.12 Highway 90 (rear) and partially damaged railway (front) on the West Pascagoula River (USGS Center for Coastal & Watershed Studies)

Following this introduction, Chapter 2 presents the literature review associated with the storm surge modeling efforts. Chapter 3 presents finite element mesh development and Chapter 4 presents the numerical modeling code used in this study, ADCIRC-2DDI. The model set up including discussions about model forcings and boundary conditions is presented in Chapter 5. The model results are presented and discussed in Chapter 6. Finally, conclusions and future work are presented in Chapter 7.

CHAPTER 2. LITERATURE REVIEW

This chapter presents a literature review of the following two topics: 1) a general introduction to storm surge generation, 2) storm surge modeling, including previous modeling studies for the United States Gulf Coast.

2.1 Storm Surge Generation

Storm tide is defined as a high water level created by the combination of a storm surge (the change in water level due to the wind and pressure effects caused by a tropical storm) and the astronomic tide (the normal rise and fall movement of the water due to Earth's gravitational interaction with the moon and sun). Storm tide is greatest when the arrival of the storm surge coincides with the occurrence of an astronomic high tide. Figure 2.1 shows an example of a normal high tide of 2 ft in a particular area and storm surge of 15 ft producing a storm tide of 17 ft. Therefore, it is necessary to construct and test a numerical model that is capable of accurately describing tidal hydrodynamics and meteorologically driven storm surge in order to provide a reasonable prediction of the storm tide.

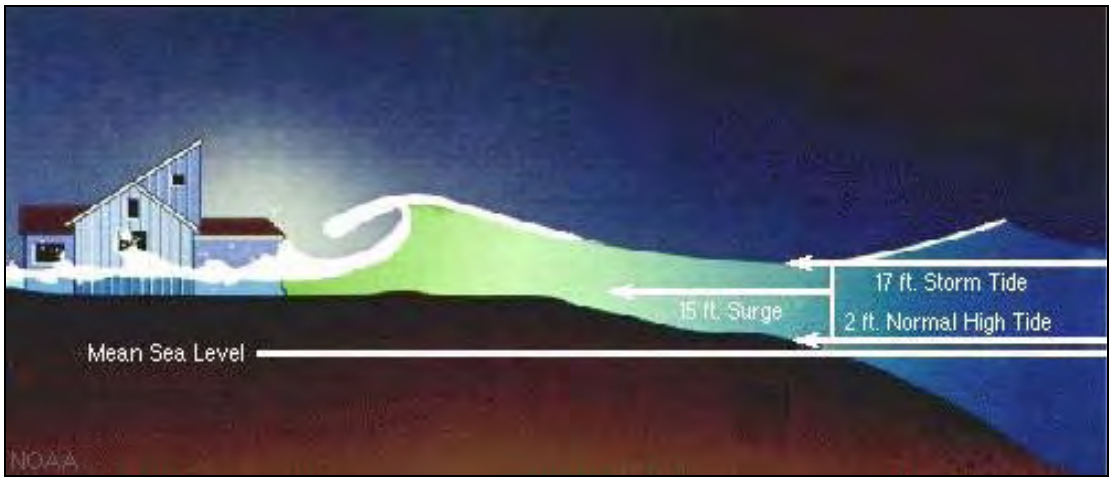

Figure 2.1 Graphical Depiction of Storm Surge (NOAA)

A storm surge is comprised of the following four basic mechanisms at or near the shoreline: 1) a wind-driven surge caused by a strong onshore wind, 2) inverted barometric effect (pressure surge), 3) geostrophic tilt, a result of alongshore current, and 4) set-up from a short wave (wind-induced wave) (Reid,1990).

Most storm surge is typically driven by sustained wind during a storm event on shallow coastal regions (Figure 2.2). Pressure surge resulting from reduced atmospheric pressure is also responsible for a small part of the storm surge, since the lower central pressure causes the ocean levels to rise (e.g. a 1 mb drop in pressure will produce a 1 cm increase in water level height; Figure 2.3). The pressure is lowest in the eye of the storm; the lower the pressure, the more intense the winds are and in turn higher storm surges are produced. It is then necessary to include in the numerical model the combined meteorological effect of the winds and pressures.

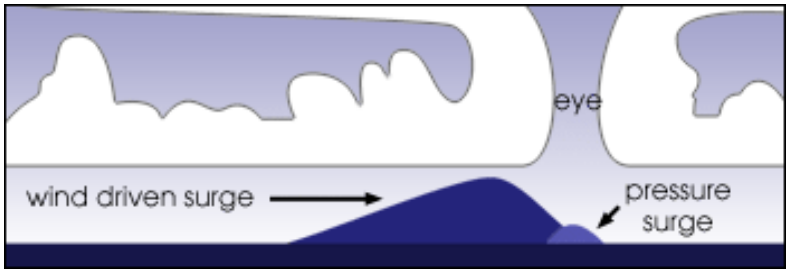

Figure 2.2 Storm Surge cased by Wind and Pressure (Simmon, NASA Goddard Space Flight Center)

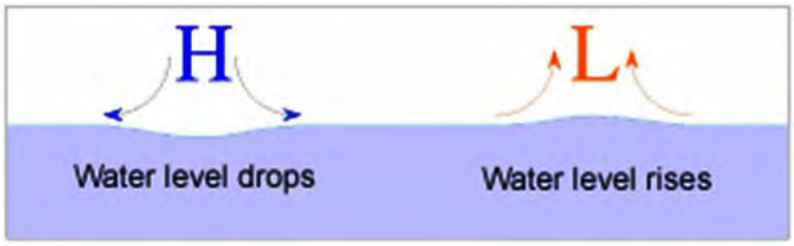

Figure 2.3 Inverted Barometric Effect (http://www.oc.nps.edu/)
(During periods of low pressure, the water level tends to be higher than normal.)

Elsner and Kara (1999) prescribe that the size and extent of the surge is attributable to: 1) the configuration (shape and topography) of the coastline, 2) the path and angle of the storm against the coastline, and 3) the duration of the maximum winds. Also, Simpson (2003) explains that high surge elevations occur where the bathymetry inclines more smoothly as it is the case for the continental shelf. As the storm surge moves overland inundation occurs including breaching of dunes or coastal protection structures such as levees. Breaking waves and wave run-up also contribute to the storm surge level. Further, inundation effects caused by storm surge are intensified by wave overtopping and localized intense rainfalls which can result in coincident freshwater flooding.

2.2 Storm Surge Modeling

Like many hydrodynamic models, ADCIRC, the model used in this study, is capable of simulating storm surge including the pressure surge, the wind-driven surge, geostrophic tilt as well as astronomic tides. It should be noted that short wave set-up and run-up are not described by the code, however, since ADCIRC can incorporate output information from a short-wave model in form of radiation stress terms, there are also several coupling techniques that have been developed. Dietsche (2004) summarized the wave property and availability of ADCIRC model (Table 2.1).

Table 2.1 Wave Property and Availability of ADCIRC Model Code

Wave Name	Wave Type	Caused by	ADCIRC included
Wind-driven Surge	Long	Storm Winds	Yes
Pressure Surge	N/A	Low Pressure	Yes
Geostrophic Tilt	Long	Alongshore Currents	Yes
Astronomic Tides	Long	Gravity	Yes
Short Wave Set-up	Short	Wave Radiation	No
Short Wave Run-up	Short	Non-breaking Waves	No

In the late 1990s, the U.S. Army Corp of Engineers New Orleans District and the ADCIRC development group started their collaboration on developing a storm surge model for New Orleans and the southern Louisiana coast. Since then, the group has constructed a sequence of models for southern Louisiana with varying degrees of detail and resolution, which they continue to refine today. The Corps applies the resulting model as their design tool to optimize levee construction in Southern Louisiana (Westerink et al., 2004). Presently, ADCIRC is being applied to a number of flood studies conducted by FEMA, including the update to FEMA's Flood Insurance Rate Map (FIRM) in Hawaii and the examination of the devastating effects of Hurricane Katrina and Rita in Mississippi and Louisiana. So far these two projects indicate that flood

elevations shown in the current FIRMs are significantly under-predicted (Massey et al. 2007).

There are distinct advantages to using the ADCIRC model for applications such as those performed in this study (Ceyhan et al., 2007). One clear advantage of using ADCIRC is its capability of simulating storm surge over a large computational domain, from the deep ocean into shallow coastal regions, with variably sized elements. The unstructured meshing approach allows for high-resolution descriptions of coastal areas with complex shorelines and bathymetry. Various boundary conditions are prepared such as mainland, island and ocean which are driven by models with or by observations. From a computational perspective, the model is well optimized and efficient, and it is available in single thread and parallel versions which can be chosen depending on the machine precision. Furthermore, a Discontinuous Galerkin based algorithm will be utilized in place of current Continuous Galerkin based algorithm in the near future.

Blain and Westerink (1994) investigated the influence of the domain size on storm surge modeling with a sensitivity analysis on the boundary condition specification. The study suggests that selecting a large enough model domain be capable of properly describing propagation of the storm surge throughout the computational domain from the continental shelf to the coastal regions. For instance, three domains are examined for a Hurricane Kate (1985) storm surge simulation using ADCIRC-2DDI. The smallest Florida coast domain is relatively small with a 175 km radius semi-circular open-ocean boundary lying on the Florida panhandle coastline centered on Panama City, FL and is situated on the

continental shelf. The second smallest domain includes the entire Gulf of Mexico. It has two open boundaries from Florida peninsula to Havana, Cuba, and from Havana to Cancun, Mexico. The largest domain (Eastcoast domain) encompasses the western North Atlantic Ocean, the Caribbean Sea, and the Gulf of Mexico (which is the same scale as the WNAT-53K). The resulting storm surge model using the smallest domain is significantly underestimated and not adequate because the cross-shelf boundary cannot capture the storm surge generation. The Gulf of Mexico model performed well, however, was not able to model resonant modes correctly since it is dependant on interactions between the Gulf and contiguous regions (e.g. the Caribbean Sea, North Atlantic Ocean). The largest model is the best representation of the storm surge and resonant modes. The model utilizes the basin to basin interaction as well as the basin resonant modes. It also minimizes the influence of the boundary conditions on storm surge generation in coastal areas by using a single deep-ocean boundary.

In addition, Blain et al. (1995) and Blain et al. (1998) determined the relationship between grid resolution and the model accuracy. It is concluded that discretization of the computational domain affects the model accuracy and adequate representation of storm surge requires high level resolution especially at the coastline and near shore regions. To demonstrate this, two mesh domains were prepared; the first included 23,566 nodes and 43,238 elements (SG01), and the second was a byproduct SG01, containing a two-fold increase in resolution, with 90,435 nodes and 172,952 elements (CG01). The model performance was tested using ADCIRC-2DDI with an application of Hurricane Camille in the northern Gulf of Mexico along the Mississippi coastline. Regardless of the storm

characteristics such as path, spatial scale and forward velocity, the most critical factor for an accurate storm surge prediction was shown to be refinement of the coastline and increased grid resolution in coastal regions.

Chen et al. (2007) have developed a coupling approach using ADCIRC as an advanced surge model and SWAN (the third generation spectral wave model) as a wave model to study storm tides on coastal highways (HW193 and HW 90) in Mobile Bay estuary caused by Hurricane George (1998). Mobile bay is a semienclosed estuary about 50 km long with a maximum width of 36 km. The bathymetry is relatively shallow with an average depth of 3 m and the tides are minimal, with tidal ranges on the order of tens of centimeteres. Hurricane George formed in the eastern Atlantic Ocean on September 25, 1998 and moved into the Gulf of Mexico at Category 3 strength. On September 28, the storm made landfall in Biloxi, Mississippi at Category 2 strength. At Dauphin Island, located at the entrance of Mobile Bay, the recorded wind speed intensified from 22.9 to 30.2 m/s within 3 hours and a sustained wind speed above 27.5 m/s lasted for about 6 hours. As a result, a 1.4 to 1.8 m storm surge was observed near the entrance of the Bay and 2.8 m of storm surge was observed at the coastline. The finite element mesh used in the study was developed using the Surface-water Modeling System (SMS). The computational domain encompasses the northern Gulf of Mexico, from the city of Gulf Shores, Alabama to the Mississippi-Alabama state border, including Mobile Bay and its delta. It should be emphasized that the land boundary is extended from the 0-m contour to the 5-m contour above the mean sea level to simulate inundation. The resulting computational mesh contained 36,021 computational nodes with minimum node spacing

of 40 m on the highways and maximum node spacing of 2 km in the offshore region. The SWAN domain nests over the ADCIRC domain only where higher grid resolution is required, and the short-wave simulation is driven by boundary conditions derived from the ADCIRC simulation. There are several model forcings applied: 1) water levels at open-ocean boundaries from measured stage data, 2) wind and atmospheric pressure calculated from the C-MAN. 3) gradients of radiation stress determined by SWAN serve as a forcing agent for the ADCIRC simulation. Consequently, the coupled model approach was used to provide valuable wave information as well as inland flooding conditions which became useful to shore design and protection. The model results from ADCIRC demonstrate the flooding with 1.8 height storm surge on the HW 193, a hurricane evacuation route with a surface elevation only 1 m above NAVD88. Although HW 90 runs across several rivers and has complex geometry, the nested SWAN model indicates that 1.5-m wind-driven waves with peak periods of 4.5 seconds were produced by Hurricane George.

The National Hurricane Center performs storm surge prediction using the SLOSH model (Sea, Lake and Overland Surges from Hurricanes). SLOSH is able to utilize several input information such as central pressure of a tropical storm, storm size, the storm's forward speed, track, and maximum sustained winds. Local topography, bay and river configurations, water depth, and other physical features are taken into account, in a predefined grid referred to as a SLOSH basin. Also, overlapping SLOSH basins are defined for the southern and eastern coastline of the continental U.S. Some storm simulations are calculated by using more than one SLOSH basin. For instance, Katrina

SLOSH model for the northern Gulf of Mexico landfall used two basins, the Lake Ponchartrain/New Orleans basin and the Mississippi Sound basin. The result from the model will produce the MEOW (Maximum Envelope of Water) that occurred at each location. Usually, several simulations with varying input parameters are generated to create a map of MOMs (Maximum of Maximums) to allow for inaccuracy of the hurricane forecast track. Also, for hurricane evacuation studies, a family of storms with representative tracks, diameter, and speed for the at-risk areas is modeled to define the potential maximum water heights.

CHAPTER 3. FINITE ELEMENT MESH DEVELOPMENT

This chapter presents the development of the unstructured finite element meshes that are used in this study: 1) a brief review of the Pascagoula in-bank model development process (Wang, 2008), 2) floodplain model domain development, including the inlet- and WNAT-based models.

3.1 Preliminary In-bank Mesh

Wang (2008) and the CHAMPS Lab at the University of Central Florida developed an inlet-based comprehensive mesh to model in-bank flow in the Pascagoula River (Figure 1.1). The inlet-based comprehensive in-bank mesh, and all byproducts and modifications of this mesh presented herein, are generated using the Surface-water Modeling System (SMS). A three-step procedure is followed within SMS in order to develop all meshes discussed in this thesis: 1) digitize the boundaries, 2) generate the two-dimensional finite element mesh, and 3) interpolate interpolate onto the resulting triangulation the bathymetric data provided by the Federal Emergency Management Agency (FEMA) Southern Louisiana Gulf Coast Mesh (SL15 Mesh, Figure 3.1) and the U.S. Army Corps Mobile District.

The SL15 mesh was developed by Dr. Joannes Westerink and his team using data from LIDAR mapping projects covering the southern Louisiana region. Some of the topographic and bathymetric data were calibrated using modern GPS technology and

grand measurements for quality control purposes (IPET Force - U.S. Army Corps of Engineers, 2007).

The final comprehensive in-bank mesh contains 136,676 computational points and 211,312 triangular elements (Figure 1.1). The nodal spacing varies from 100 meters downstream to only several meters upstream in the tributaries. It is noted that the minimum spacing is only about 1.4 meters due to the requirement that at least three elements be used across the river width to adequately define the river cross-section and describe propagation of the river flow. The shoreline, river, and island boundaries are assigned with no-flow boundary constraints. This means the boundaries act like vertical walls and do not permit for any flow through the no-flow boundaries.

Following, the comprehensive mesh was adapted to decrease the total number of computational nodes, with the motivation of increasing the computational time step. This was accomplished by removing the tributaries lying above the North American Vertical Datum of 1988 (NAVD88) and those containing an unnecessary high resolution. The final version of this modified mesh, herein referred to as Mesh A, has 40,060 computational nodes and 66,442 triangular elements, which is less than one third the size (measured in terms of number of computational nodes) of the original comprehensive mesh (Figure 3.2).

Additionally, during the process of bathymetry data assignment, the Cross Section Interpolation Toolbox was developed in order to interpolate 1D channel-bed cross section

data provided by the LMRFC into the 2D model (Figure 3.2). (The field survey was conducted by USGS.) This newly developed function has the potential to serve in the absence of a more intelligent interpolation function in the current version of SMS.

As a result of the model development effort, it was demonstrated that the depth updated Mesh A showed a significant improvement on the model and historical data comparisons and illustrated the importance of accurate bathymetry data for developing the astronomic tide model.

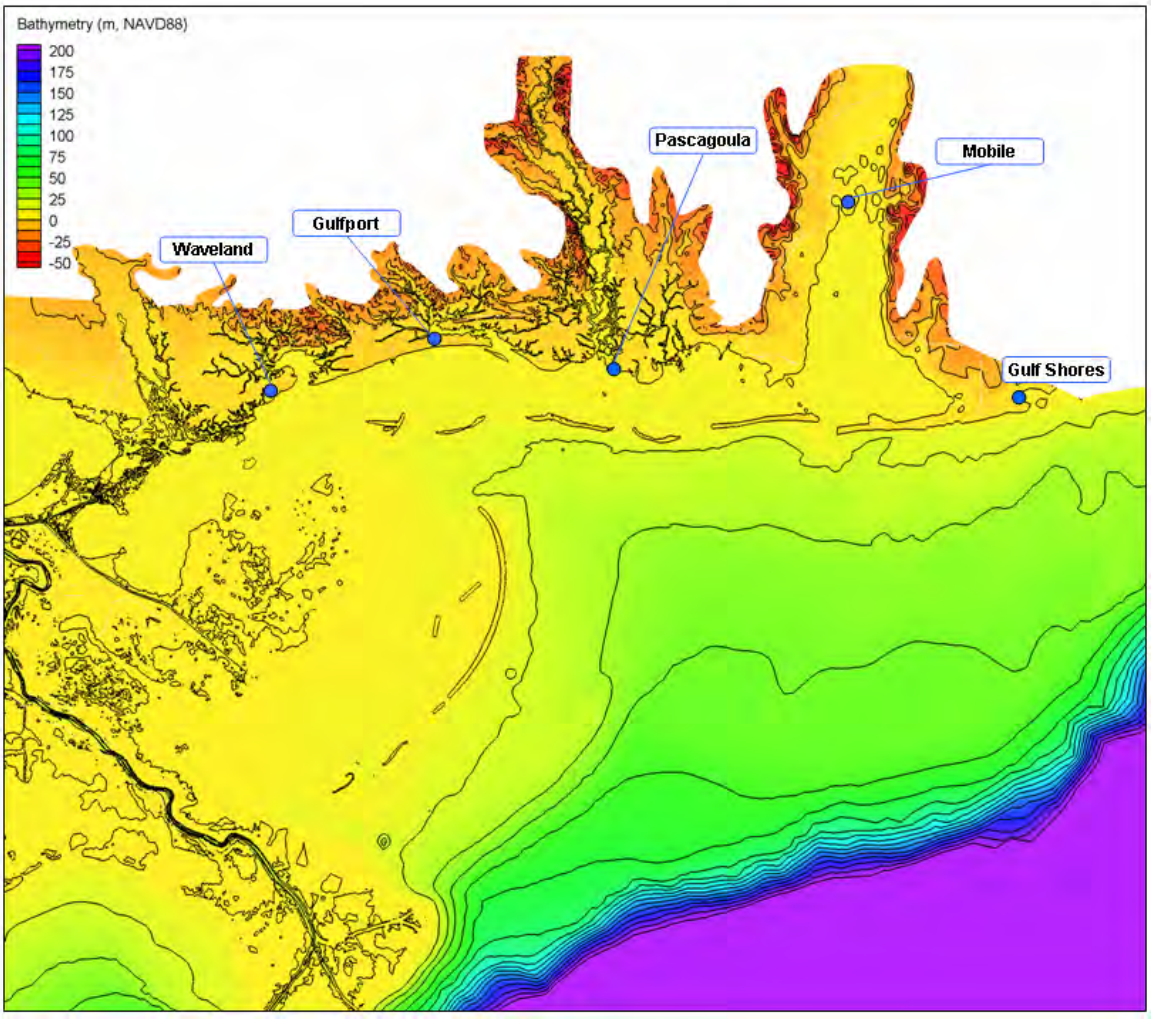

Figure 3.1 SL15 Mesh: Zoomed in the Pascagoula River Region

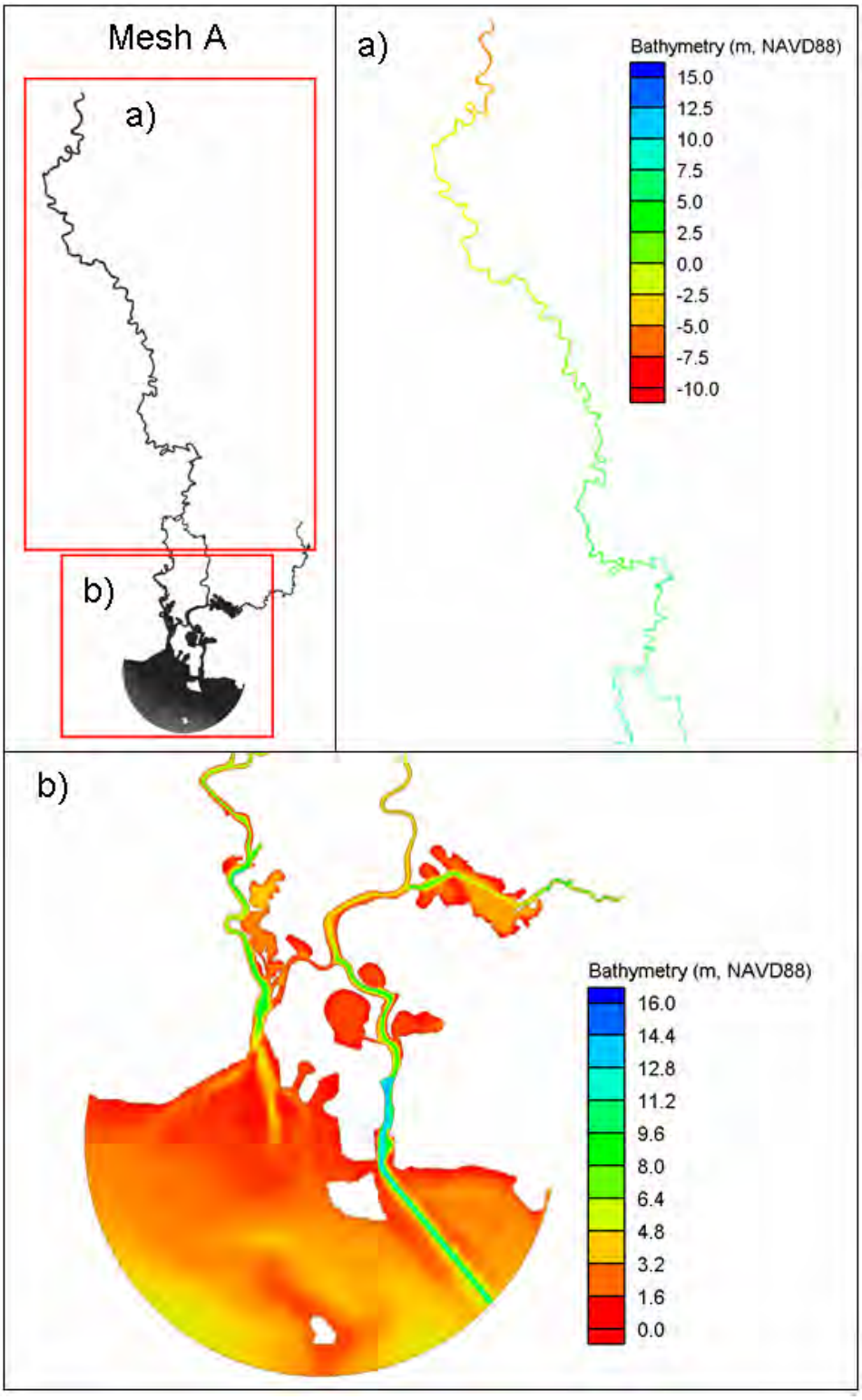

Figure 3.2 Pascagoula River Preliminary In-bank Mesh (Mesh A)

3.2 Floodplain Mesh Development

For storm surge simulations expected to produce water flooding over inland areas, complex coastal and inland geometry, as well as bathymetry must be well represented. In this study, modifications to the preliminary in-bank mesh concerning the Lower Pascagoula and Escatawpa Region have been completed by generating additional computational regions inland, where much of the marsh region is inundated during storm surge events (Figure 3.3). SMS 9.2 is utilized throughout the mesh development process employed herein.

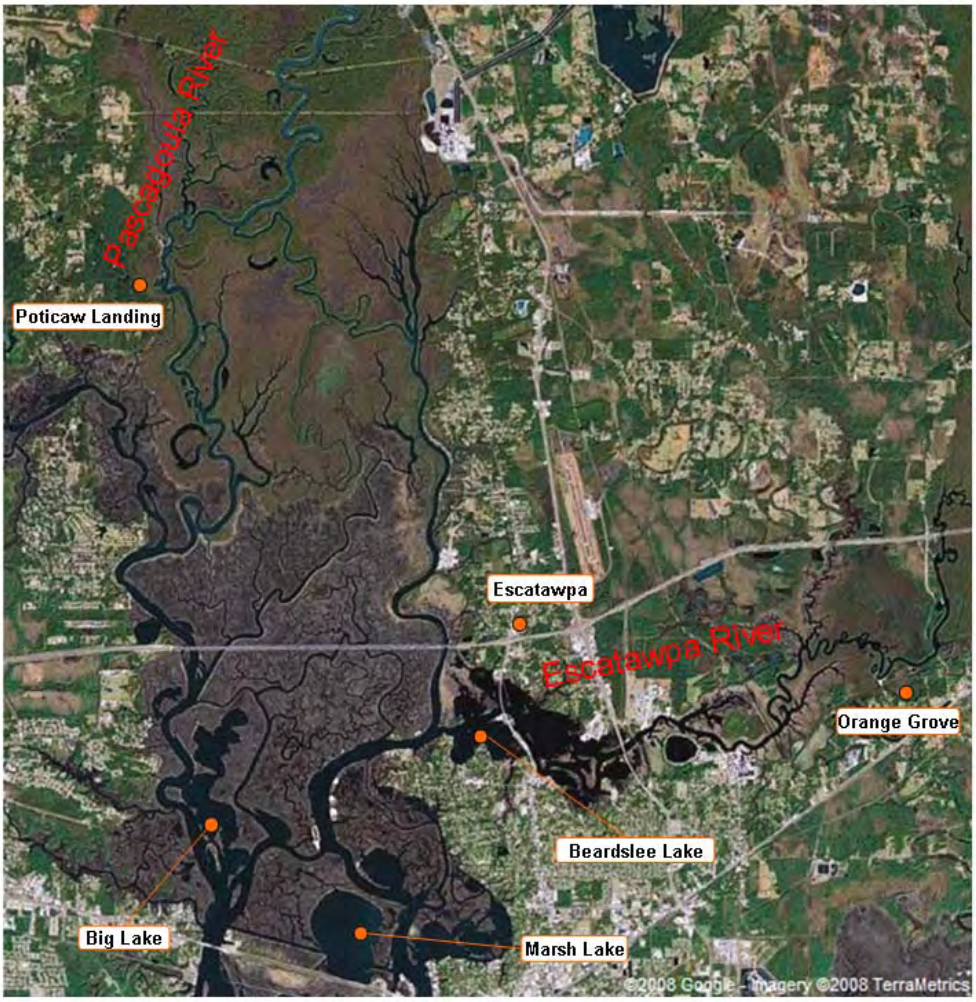

Figure 3.3 Figure 3.4 Satellite Images of Marsh Areas in the Lower Pascagoula and Escatawpa Rivers (image courtesy of Google Earth)

An initial development of the floodplain model employs topography up to the 1.5-meter contour, where all topography data used in the floodplain mesh originates from the SL15 mesh (Figure 3.4). One target of this model is improve upon the tide-only model results presented by Wang (2008), which implied the necessity to include the marsh areas in order to sufficiently describe tide-driven flows within the river bank. The resolution of the marsh area is based on that used by the SL15 mesh. Bathymetry within the preliminary in-bank mesh remains from that of Wang (2008), and the bathymetry within the additional inland area and refined transition area has been interpolated from the SL15 mesh. With this initial version of the floodplain model (herein referred to as FP1.5_INLET_A; Figure 3.5, Figure 3.6), it will be demonstrated in Chapter 6 that the floodplain mesh provides for an improved result with respect to the astronomic tide solution in the Pascagoula River.

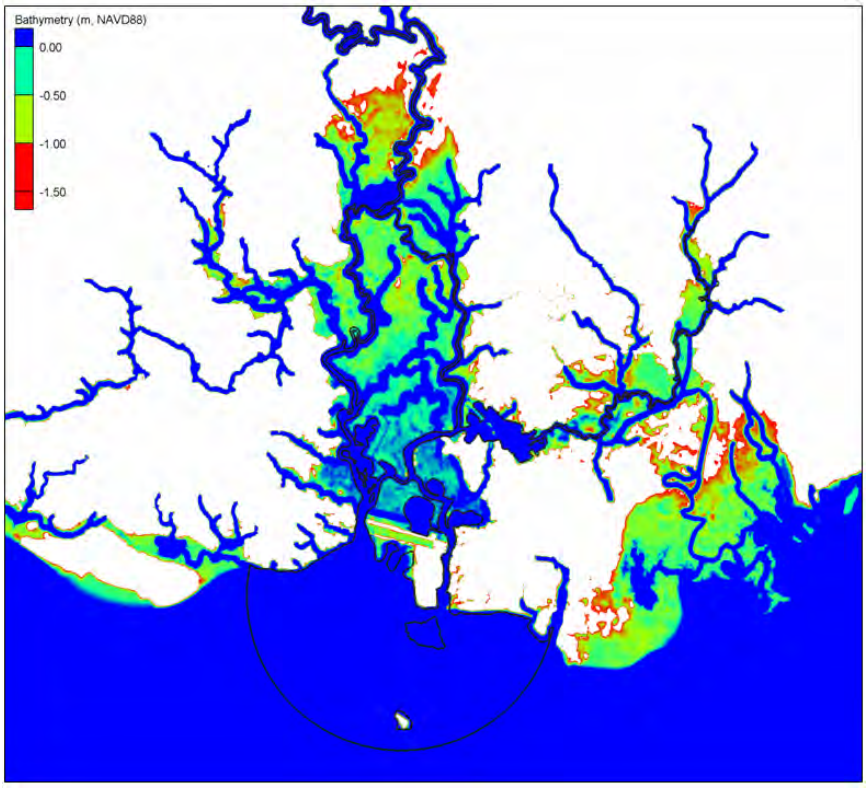

Figure 3.5 SL15 Mesh: Topography Contours Up to 1.5 m above NAVD88

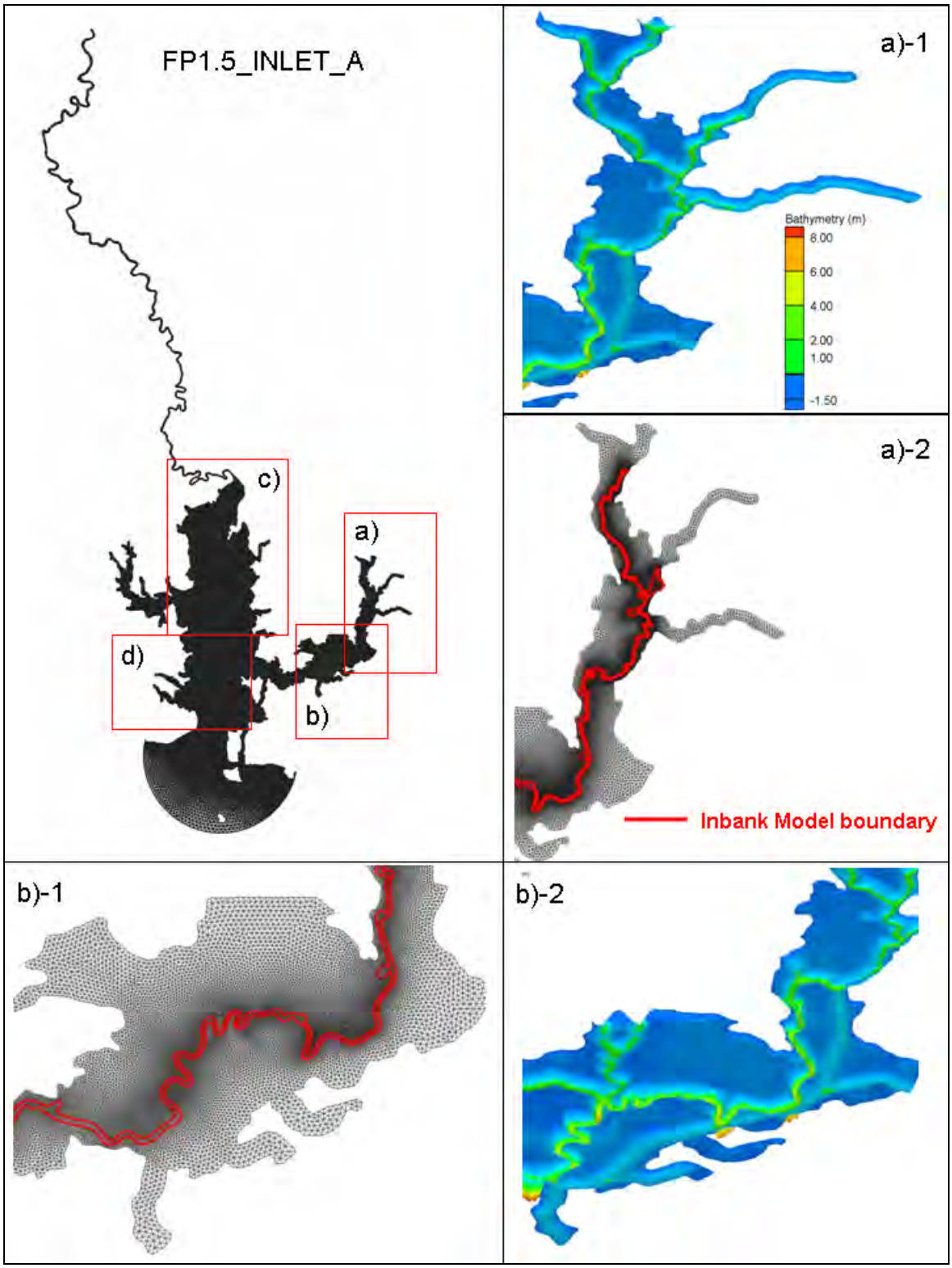

Figure 3.6 Inlet-based 1.5 m Floodplain Mesh (FP1.5_INLET_A; Used for Astronomic Tide Simulation)

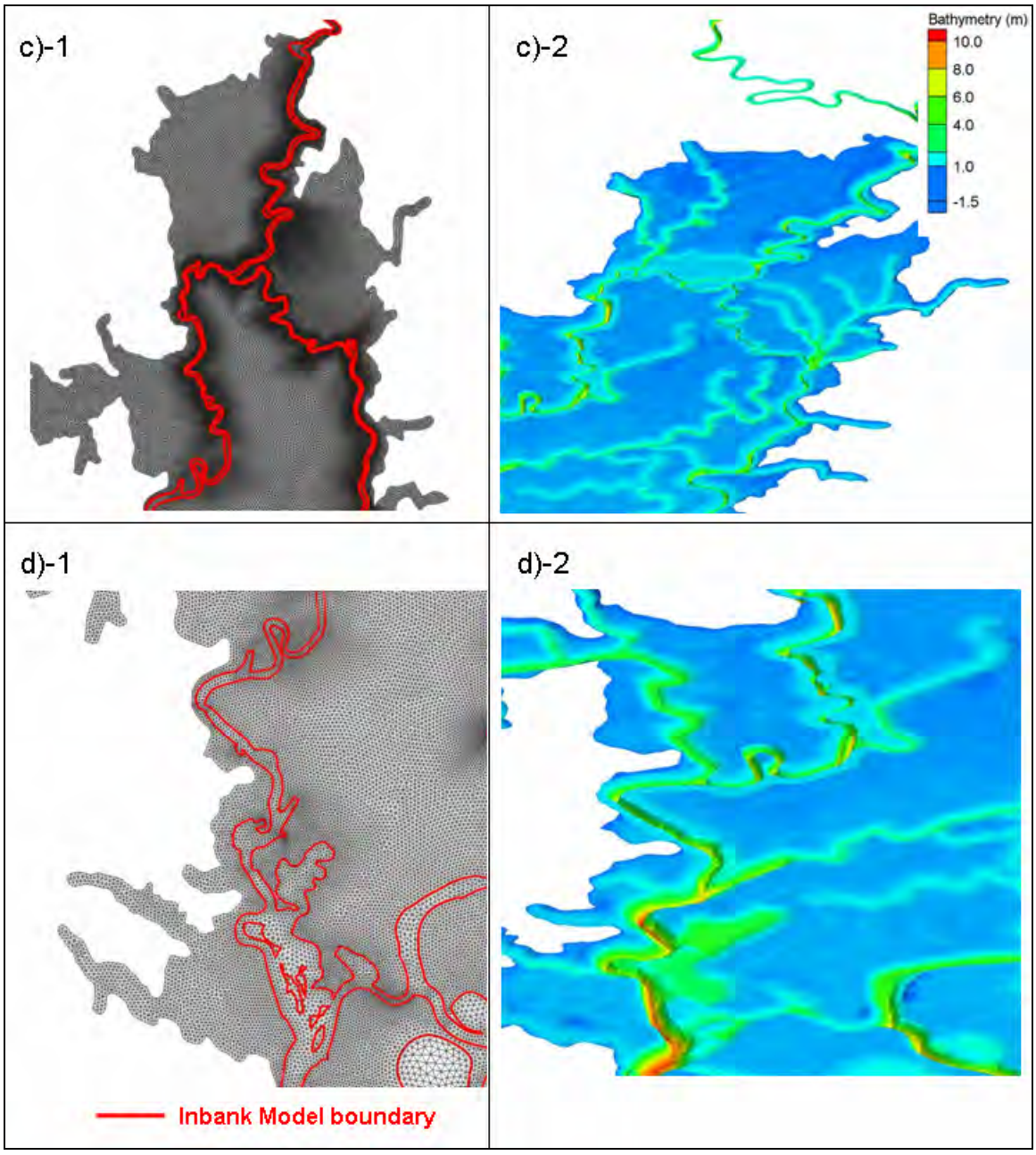

Figure 3.7 Inlet-based 1.5 m Floodplain Mesh (FP1.5_INLET_A; Typically for Astronomic Tide Simulation)

However, in order to simulate storm surge events, it is necessary for some river islands located at and near the inlets within the floodplain area be meshed over to allow for the wetting/drying of elements. Four islands within the FP1.5_INLET_A mesh were meshed over using SMS with the respective topography interpolated from the SL15 mesh. The resulting mesh consists of 112,451 computational nodes and 217,358 triangular elements (FP1.5_INLET_B; Figure 3.7).

Next, the 1.5-m floodplain mesh was incorporated into the WNAT-53K model domain (Figure 1.2). The coastline and barrier island boundaries are refined by digitized shoreline data retrieved from the Coastline Extractor (National Geophysical Data Center [NGDC]). Approximately 160 km of coastline from Waveland, Mississippi (just west of St. Louis Bay) at the west to Gulf Shores, Alabama (just east of Mobile Bay) at the east is selected since it is expected to influence the storm surge dynamics in the Pascagoula River during a hurricane event (Figure 3.8). Furthermore, it was necessary to reconstruct the mesh region within 80 km of the Pascagoula Inlet in order to obtain a reasonably smooth transition between the local (1.5-m floodplain) and the global (WNAT-53K) mesh boundaries. It is noted that the mesh resolution at the shipping channel through one of barrier islands (Petit Bois Island) is increased to capture the deeper bathymetry. For barrier islands, we have obtained two variations; one has a no-flow boundary and values at the boundary nodes are adjusted to 0.5 m (FP1.5_WNAT_A; Figure 3.9), while the other has meshed over islands and its topography is directly interpolated from the SL15 mesh (FP1.5_WNAT_B; Figure 3.10). Table 3.1 present a summary of the mesh variations.

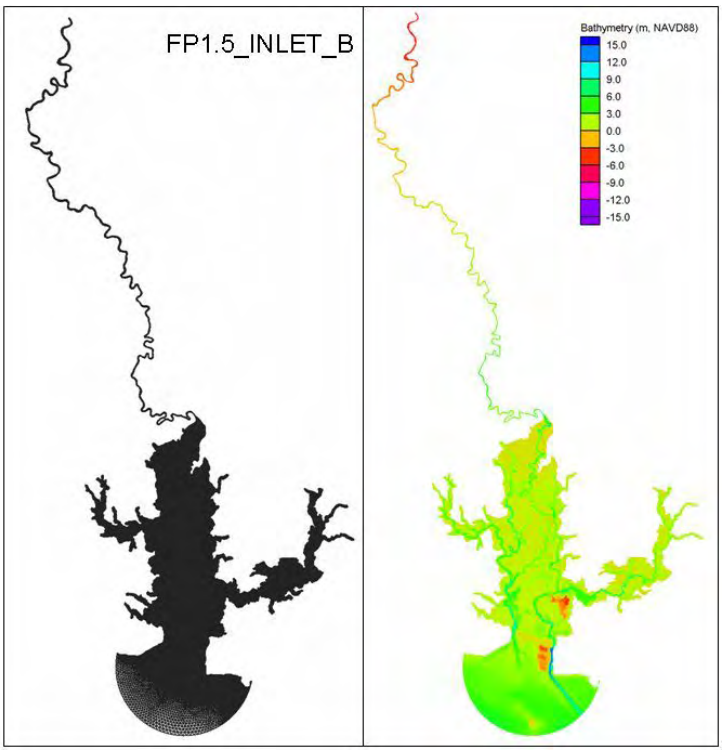

Figure 3.8 Inlet-based 1.5 m Floodplain Mesh (FP1.5_INLET_B; River Islands Meshed Over)

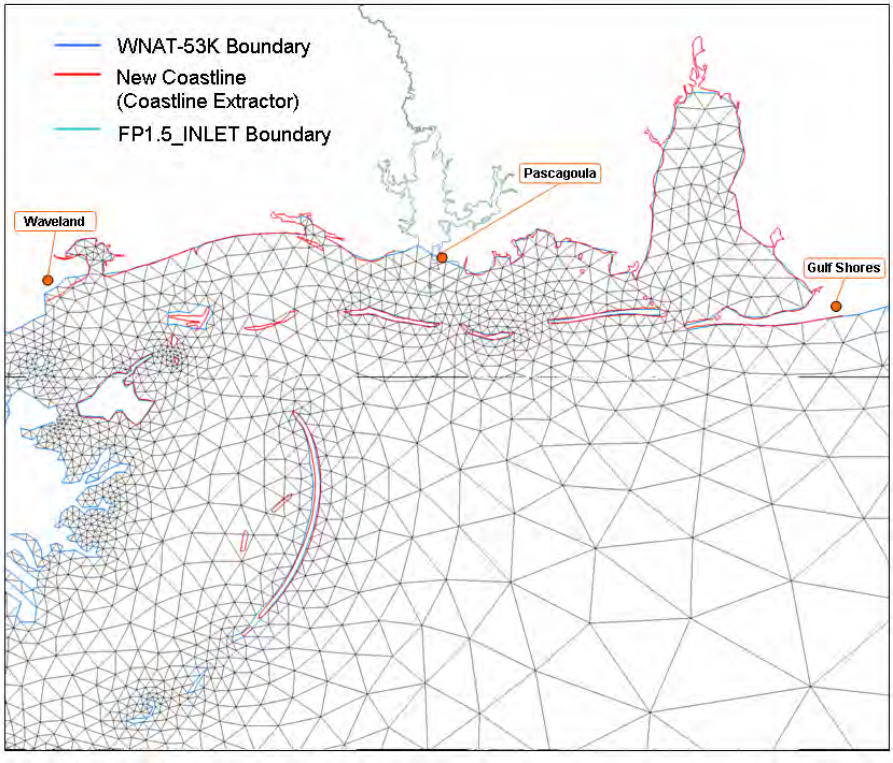

Figure 3.9 Coastline Boundary Comparisons

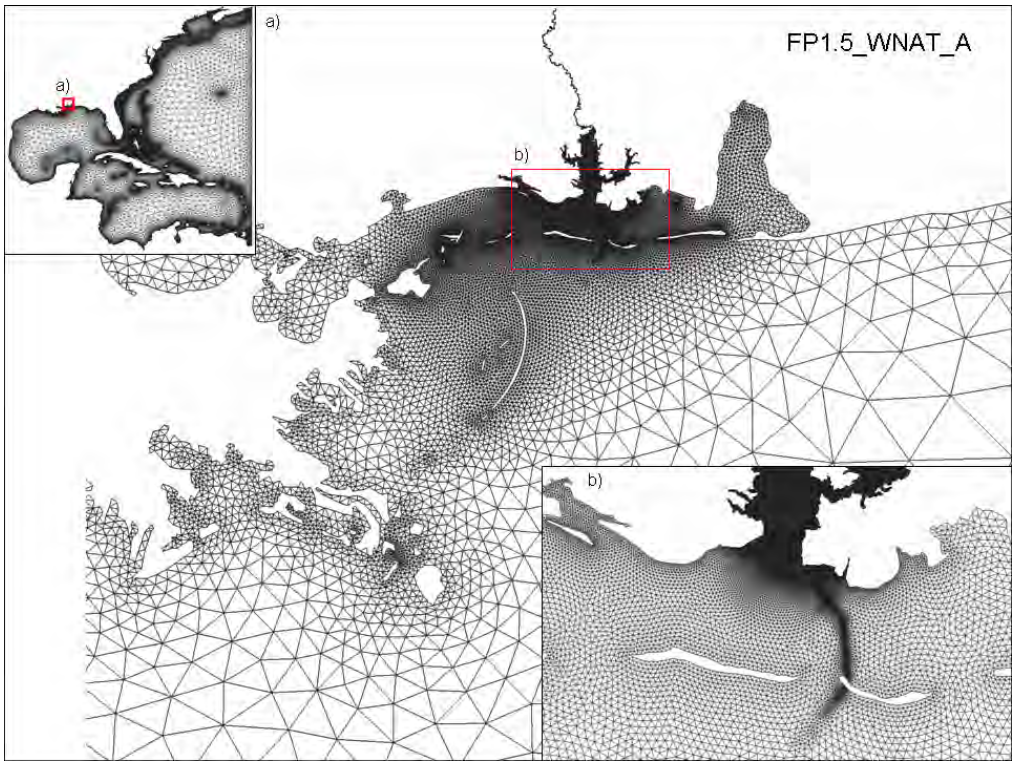

Figure 3.10 WNAT-based 1.5 m Floodplain Mesh (FP1.5_WNAT_A)

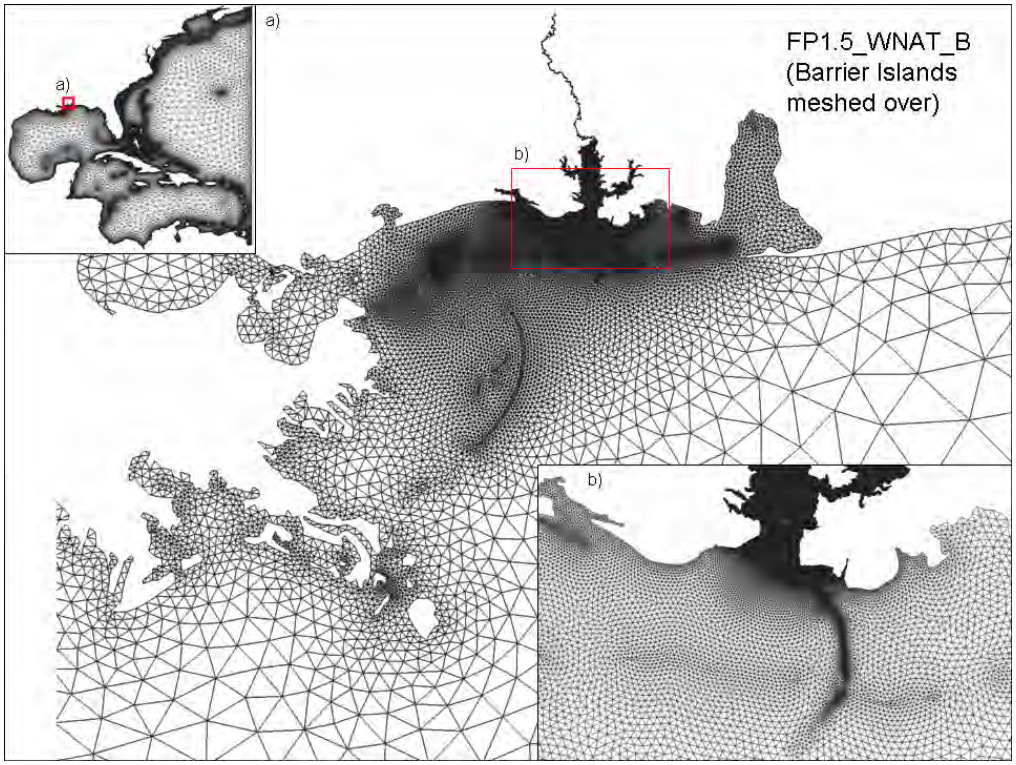

Figure 3.11 WNAT-based 1.5 m Floodplain Mesh (FP1.5_WNAT_B; Barrier Islands Meshed Over)

Table 3.1 Summary of Mesh Variations

	Mesh			Boundary				
#	ID	# of nodes	# of elements	Floodplain	Coastline	Open Ocean	River Islands	Barrier Islands
0	WNAT-53K	52,774	98,365	-	-	WNAT-53K	-	No-flow
1	FP1.5_INLET_A	109,820	211,689	SL15 1.5 m contour	Coastline extractor	2.5 km radius	No-flow	-
2	FP1.5_INLET_B	112,466	217,388			2.5 km radius	Meshed over	-
3	FP1.5_WNAT_A	175,928	336,286			WNAT-53K		No-flow
4	FP1.5_WNAT_B	176,418	337,906			WNAT-53K		Meshed over

CHAPTER 4. MODEL DESCRIPTION

This chapter represents a description of the numerical code, ADCIRC-2DDI (Advanced Circulation Two-dimensional Depth-integrated software) along with the following two topics: 1) hydrodynamic model, 2) tropical wind stress and pressure field.

4.1 Hydrodynamic Model

To compute the water-surface elevations and currents during Hurricane Katrina, ADCIRC-2DDI, a finite element hydrodynamic model which solves the nonlinear shallow water equations, is applied to the shallow-water river and estuarine systems concerning the Pascagoula River.

The depth integrated equations of mass and momentum conservation are used in ADCIRC-2DDI, subject to the incompressibility, Boussinesq, and hydrostatic pressure approximations. In a spherical coordinate system, the following equations are set up: the continuity equation (4.1) and momentum equations (4.2) and (4.3).

$$\frac{\partial \zeta}{\partial t} + \frac{1}{R\cos\phi}\left[\frac{\partial UH}{\partial \lambda} + \frac{\partial (VH\cos\phi)}{\partial \phi}\right] = 0 \tag{4.1}$$

$$\begin{aligned} &\frac{\partial U}{\partial t} + \frac{U}{R\cos\phi}U\frac{\partial U}{\partial \lambda} + \frac{1}{R}V\frac{\partial U}{\partial \phi} - \left(\frac{\tan\phi}{R}U + f\right)V \\ &= -\frac{1}{R\cos\phi}\frac{\partial}{\partial \lambda}\left[\frac{p_s}{p_0} + g(\zeta - \eta)\right] + \frac{\tau_{s\lambda}}{p_0 H} - \tau_* U \end{aligned} \tag{4.2}$$

$$\frac{\partial \boldsymbol{V}}{\partial \boldsymbol{t}} + \frac{\boldsymbol{U}}{\boldsymbol{R}\cos\boldsymbol{\phi}}\boldsymbol{U}\frac{\partial \boldsymbol{U}}{\partial \boldsymbol{\lambda}} + \frac{1}{\boldsymbol{R}}\boldsymbol{V}\frac{\partial \boldsymbol{V}}{\partial \boldsymbol{\phi}} - \left(\frac{\tan\boldsymbol{\phi}}{\boldsymbol{R}}\boldsymbol{U} + \boldsymbol{f}\right)\boldsymbol{U}$$
$$= -\frac{1}{\boldsymbol{R}}\frac{\partial}{\partial \boldsymbol{\phi}}\left[\frac{\boldsymbol{p}_s}{\boldsymbol{p}_0} + \boldsymbol{g}(\boldsymbol{\zeta} - \boldsymbol{\eta})\right] + \frac{\boldsymbol{\tau}_{s\boldsymbol{\phi}}}{\boldsymbol{p}_0\boldsymbol{H}} - \boldsymbol{\tau}_*\boldsymbol{U} \qquad (4.3)$$

where

$\boldsymbol{t}$ = time

$\boldsymbol{\phi}, \boldsymbol{\lambda}$ = degrees longitude and degrees latitude

$\boldsymbol{\zeta}$ = free surface elevation

$\boldsymbol{U}, \boldsymbol{V}$ = depth-averaged horizontal velocities in the $\boldsymbol{\lambda}$ and $\boldsymbol{\phi}$ directions

$\boldsymbol{R}$ = radius of the Earth,

$\boldsymbol{H} = \boldsymbol{\zeta} + \boldsymbol{h}$ = total height of the water column

$\boldsymbol{h}$ = bathymetric depth

$\boldsymbol{f} = 2\Omega\sin\boldsymbol{\phi}$ = Coriolis parameter

Ω = angular speed of the Earth

$\boldsymbol{p}_s$ = atmospheric pressure at the free surface

$\boldsymbol{g}$ = acceleration due to gravity

$\boldsymbol{\eta}$ = effective Newtonian equilibrium tide potential

$\boldsymbol{p}_0$ = reference density of water

$\boldsymbol{\tau}_{s\lambda}, \boldsymbol{\tau}_{s\phi}$ = applied free surface stresses (e.g., wind and wave radiation stresses)

$\boldsymbol{\tau}_* = \boldsymbol{C}_f \dfrac{\left(\boldsymbol{U}^2 + \boldsymbol{V}^2\right)}{\boldsymbol{H}}$ = bottom stress

C_f = bottom friction coefficient

In these governing equations of the hydrodynamic model, continuity (see Eq. (4.1)) provides a balance between the water level and the flux into/out of the water column. Momentum (see Eqs. (4.2) and (4.3)) provides a balance between the location acceleration (left-most term) and the following effects (given in the order as presented in Eqs. (4.1) and (4.2)): 2) advection; 3) Coriolis; 4) atmospheric pressure; 5) pressure; 6) tidal potential; 7) surface wind stress; 8) bottom friction.

The effective expression for the effective Newtonian equilibrium tide potential is given by Reid (1990) as:

$$\eta(\lambda,\phi,t) = \sum_{n,j} \alpha_{jn} C_{jn} f_{jn}(t_0) L_j(\phi) \cos\left[\frac{2\pi(t-t_0)}{T_{jn} + j\lambda + v_{jn}(t_0)}\right] \tag{4.4}$$

where

C_{jn} = constant characterizing the amplitude of tidal constituent n of species j

α_{jn} = effective earth elasticity factor for tidal constituent n of species j

f_{jn} = time-dependent nodal factor

v_{jn} = time-dependent astronomical argument

j = 0, 1, 2 = tidal species (0: declinational; 1: diurnal; 2: semidiurnal)

$L_0 = 3\sin^2\phi - 1$

$L_1 = \sin(2\phi)$

$L_2 = \cos^2(\phi)$

λ, ϕ = degrees longitude and degrees latitude

t_0 = reference time

T_{jn} = period of constituent n of species j

Reid (1990) suggests typical values for C_{jn}, and a value of 0.69 is suggested for the effective earth elasticity factor α for all the tidal constituents, although it has been proven to be slightly constituent dependent (Schwiderski, 1980; Hendershott, 1981; Wahr, 1981).

Equations (4.1) to (4.3) are transformed from spherical into Cartesian coordinate system using a Carte Parallelo-grammatique cylindrical map projection (CPP) as part of the solution procedure (Westerink 1994):

$$x' = R(\lambda - \lambda_0)\cos\phi_0 \tag{4.5}$$

$$y' = R\phi \tag{4.6}$$

where

λ_0, ϕ_0 = center point of the projection

Applying the CPP, (4.5) and (4.6), to the original fully nonlinear shallow water equations, (4.1) to (4.3), leads to the primitive nonconservative expressions in a CPP coordinate system:

$$\frac{\partial \zeta}{\partial t} + \frac{\cos\phi_0}{R\cos\phi}\frac{\partial (UH)}{\partial x'} + \frac{1}{\cos\phi}\frac{\partial (VH\cos\phi)}{\partial y'} = 0 \tag{4.7}$$

$$\frac{\partial \boldsymbol{U}}{\partial \boldsymbol{t}} + \frac{\cos \boldsymbol{\phi}_0}{\cos \boldsymbol{\phi}} \boldsymbol{U} \frac{\partial \boldsymbol{U}}{\partial \boldsymbol{x}'} + \boldsymbol{V} \frac{\partial \boldsymbol{U}}{\partial \boldsymbol{y}'} - \left(\frac{\tan \boldsymbol{\phi}}{\boldsymbol{R}} \boldsymbol{U} + \boldsymbol{f} \right) \boldsymbol{V}$$
$$= -\frac{\cos \boldsymbol{\phi}_0}{\cos \boldsymbol{\phi}} \frac{\partial}{\partial \boldsymbol{x}'} \left[\frac{\boldsymbol{p}_s}{\boldsymbol{\rho}_0} + \boldsymbol{g}(\boldsymbol{\zeta} - \boldsymbol{\eta}) \right] + \frac{\boldsymbol{\tau}_{s\lambda}}{\boldsymbol{\rho}_0 \boldsymbol{H}} - \boldsymbol{\tau}_* \boldsymbol{U} \tag{4.8}$$

$$\frac{\partial \boldsymbol{V}}{\partial \boldsymbol{t}} + \frac{\cos \boldsymbol{\phi}_0}{\cos \boldsymbol{\phi}} \boldsymbol{U} \frac{\partial \boldsymbol{V}}{\partial \boldsymbol{x}'} + \boldsymbol{V} \frac{\partial \boldsymbol{V}}{\partial \boldsymbol{y}'} - \left(\frac{\tan \boldsymbol{\phi}}{\boldsymbol{R}} \boldsymbol{U} + \boldsymbol{f} \right) \boldsymbol{U}$$
$$= -\frac{\partial}{\partial \boldsymbol{y}'} \left[\frac{\boldsymbol{p}_s}{\boldsymbol{\rho}_0} + \boldsymbol{g}(\boldsymbol{\zeta} - \boldsymbol{\eta}) \right] + \frac{\boldsymbol{\tau}_{s\phi}}{\boldsymbol{\rho}_0 \boldsymbol{H}} - \boldsymbol{\tau}_* \boldsymbol{V} \tag{4.9}$$

Solving the finite element method in the primitive form, (4.7) to (4.9), can lead to numerical instability and noise (Gray, 1982). To resolve this issue, the Generalized Wave Continuity Equation (GWCE) is applied in ADCIRC. The GWCE is derived by combining a time-differentiated form of the primitive continuity equation (4.7) and a spatially differentiated form of the primitive momentum equations (4.8) (4.9). Consequently, the GWCE in the CPP coordinate system is given as follows, where a constant in time and space, τ_0, is prescribed as a weighting factor to adjust the functionality of the GWCE between a primitive continuity equation and a pure wave equation:

$$\frac{\partial^2 \zeta}{\partial t^2} + \tau_0 \frac{\partial \zeta}{\partial t}$$

$$+ \frac{\cos\phi_0}{\cos\phi} \frac{\partial}{\partial x'} \frac{\partial \zeta}{\partial t} \left\{ U - \frac{\cos\phi_0}{\cos\phi} UH \frac{\partial U}{\partial x'} - VH \frac{\partial U}{\partial y'} + \left(\frac{\tan\phi}{R} U + f \right) VH \right.$$
$$\left. - H \frac{\cos\phi_0}{\cos\phi} \frac{\partial}{\partial x'} \left[\frac{p_s}{\rho_0} + g(\zeta - \eta) \right] - (\tau_* - \tau_0) UH + \frac{\tau_{s\lambda}}{\rho_0} \right\}$$

$$+ \frac{\partial}{\partial y'} \left\{ V \frac{\partial \zeta}{\partial t} - \frac{\cos\phi_0}{\cos\phi} UH \frac{\partial v}{\partial x'} - VH \frac{\partial V}{\partial y'} - \left(\frac{\tan\phi}{R} U + f \right) UH \right.$$
$$\left. - H \frac{\partial}{\partial y'} \left[\frac{p_s}{\rho_0} + g(\zeta - \eta) \right] - (\tau_* - \tau_0) VH + \frac{\tau_{s\phi}}{\rho_0} \right\}$$

$$- \frac{\partial}{\partial t} \left(\frac{\tan\phi}{R} VH \right) - \tau_0 \left(\frac{\tan\phi}{R} VH \right)$$

$$= 0 \qquad (4.10)$$

This study applies the hybrid bottom friction function which is more accurate in shallow water. The quadratic bottom friction equation that is used with the hybrid bottom friction formulation is defined τ_* = bottom stress as:

$$\tau_* = \frac{C_f \left(U^2 + V^2 \right)^{1/2}}{H} \qquad (4.11)$$

where

C_f = bottom friction factor

with the hybrid bottom friction, the bottom friction coefficient is defined as:

$$C_f = C_{f_{\min}} \left[1 + \left(\frac{H_{break}}{H} \right)^{\theta} \right]^{\frac{\lambda}{\theta}} \qquad (4.12)$$

where

$C_{f_{\min}}$ = minimum friction factor that is approached in deep water when the hybrid bottom friction function reverts to the quadratic bottom friction function

H_{break} = break depth to determine if hybrid function will act like a quadratic function or increase with depth similar to a Manning's type friction

θ = dimensionless parameter that determines how rapidly the hybrid function approaches its upper and lower limits

λ = dimensionless parameter that describes how quickly the friction factor increases as water depth decreases

As bathymetric depth approaches zero, the friction factor becomes $C_{f_{\min}}\left(\frac{H_{break}}{H}\right)^{\lambda}$. Also, as the depth approaches infinity, the friction factor approaches $C_{f_{\min}}$.

Wang (2008) calibrated spatially varied $C_{f_{\min}}$ values throughout the Pascagoula region and concluded that 0.0025(ocean region)-0.0075(marsh area)-0.0055(middle stream & upstream) is suggested as a good starting point with respect to astronomic tide simulation; however, in this study a value of 0.0025 is used as the standard value (Luettich et al., 1992).

4.2 Tropical Wind Stress and Pressure Field

The lower layer of the troposphere where continuous turbulent processes occur is known as the planetary boundary layer (PBL), while the upper layer is known as the free atmosphere since there are no frictional influences (Figure ?4.1). The thickness of PBL is about 1 to 2 km but varies diurnally depending on the energy budget between the land surface and the upper layer, which is affected by variable parameters such as heat, moisture, buoyancy, wind shear, and surface roughness. Wind is turbulent and gusty within the PBL, and the surface friction causes eddies and develops chaotic wind patterns. Most of the relevant weather and climate phenomena, including hurricanes, we experience on the Earth are driven by changes of the physical and chemical conditions within the PBL; therefore, it is necessary to translate these meteorological features into a forcing mechanism that can be incorporated into the numerical model in order to accomplish an accurate forecasting system.

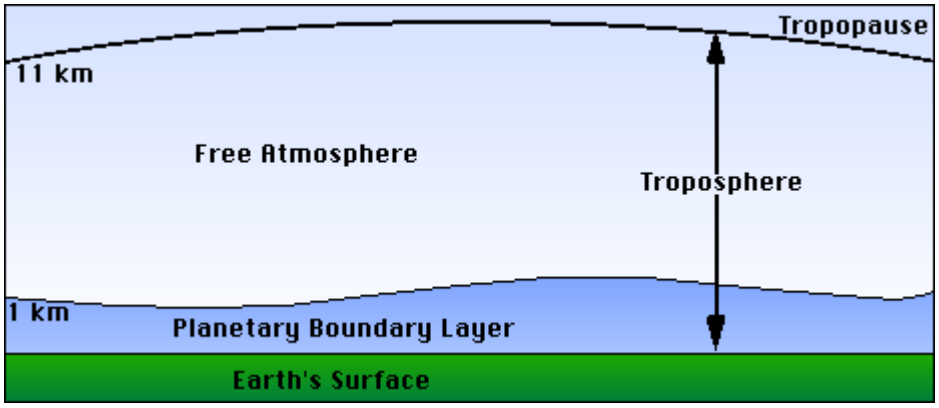

Figure 4.1 Planetary Boundary Layer (http://www.shodor.org)

Chow's vortex model (1971) was primarily introduced as a theoretical basis of the numerical schemes used to solve the primitive equations on a high resolution and

considered the asymmetry airflow in the PBL, which is important since the frictionally induced convergence in the layer leads to moist convection and ultimately produces the instability responsible for the development of tropical cyclones. The model is termed by the equation of horizontal motion, vertically averaged through the depth of the PBL in coordinates fixed to the Earth:

$$\frac{\boldsymbol{dV}}{\boldsymbol{dt}} + \boldsymbol{f}\hat{\boldsymbol{k}} \times \boldsymbol{V} = -\left(\frac{1}{\boldsymbol{\rho}}\nabla \boldsymbol{P}\right) + \nabla \cdot \boldsymbol{K}_{\boldsymbol{H}} \nabla \boldsymbol{V} + \left(-\frac{\boldsymbol{C}_{\boldsymbol{D}}}{\boldsymbol{h}}\right)|\boldsymbol{V}|\boldsymbol{V} \qquad (4.13)$$

where

$$\frac{\boldsymbol{dV}}{\boldsymbol{dt}} = \frac{\partial}{\partial \boldsymbol{t}} + \boldsymbol{V} \cdot \nabla$$

$\frac{\partial}{\partial \boldsymbol{t}}$ = local time change relative to fixed coordinates

∇ = two-dimensional del operator

$\boldsymbol{V}$ = vertically averaged horizontal wind velocity

$\boldsymbol{f}$ = Coriolis parameter

$\hat{\boldsymbol{k}}$ = unit vector in the vertical direction

$\boldsymbol{\rho}_{\boldsymbol{air}}$ = mean air density

$\boldsymbol{P}$ = depth-averaged pressure in the PBL

$\boldsymbol{H}$ = horizontal eddy viscosity coefficient

$\boldsymbol{C}_{\boldsymbol{D}}$ = surface drag coefficient

$\boldsymbol{h}$ = depth of the PBL

These approximations consider that the vertical advection of momentum is small enough to be neglected compared to the horizontal advection and that the shear stress at the top of the PBL is assumed to be zero.

The total pressure $\boldsymbol{P}$ is defined as

$$\boldsymbol{P} = \boldsymbol{P}_c + \overline{\boldsymbol{P}} \tag{4.14}$$

where

$\boldsymbol{P}_c$ = pressure field associated with the tropical cyclone translating with the storm at a speed $\boldsymbol{V}_c$

$\overline{\boldsymbol{P}}$ = large scale pressure field which is given by the corresponding constant geostrophic velocity $\boldsymbol{V}_g$ as:

$$f\hat{\boldsymbol{k}} \times \boldsymbol{V}_g = -\left(\frac{1}{\rho}\nabla\overline{\boldsymbol{P}}\right) \tag{4.15}$$

Substituting these pressure specification equations (4.14) and (4.15) into (4.13) yields

$$\frac{d\boldsymbol{V}}{dt} + f\hat{\boldsymbol{k}} \times \left(\boldsymbol{V} - \boldsymbol{V}_g\right) = -\left(\frac{1}{\rho}\nabla\boldsymbol{P}_c\right) + \nabla \cdot \boldsymbol{K}_H \nabla\boldsymbol{V} + \left(-\frac{\boldsymbol{C}_D}{h}\right)|\boldsymbol{V}|\boldsymbol{V} \tag{4.16}$$

The governing equations used in the model are formed with respect to a moving Cartesian coordinate system (x, y) whose origin is located at the low pressure center of the storm (storm's eye).

It is also noted that the pressure field $\boldsymbol{P}_c$ is radially symmetric and prescribed by the well-known exponential pressure law:

$$P_c = P_0 + \Delta p e^{-(R/r)} \tag{4.17}$$

where

P_0 = pressure at the center of the storm

$\Delta p = \overline{P} - P_0$ = pressure anomaly

R = scale radius ≈ radius to the maximum wind

r = radial distance from the center

With an option specifying Δp and R by storm quadrant, an asymmetrical pressure field results after smoothing between the pressure variations specified for each quadrant.

ADCIRC incorporates the PBL model that has been modified to directly interface. Internally, ADCIRC applies the Garratt (1977) formulation to convert the wind velocities that is computed over the nested grid of the PBL model to wind stress:

$$\frac{\tau_x}{\rho_0} = C_D \frac{\rho_{air}}{\rho_0} |W| W_x \tag{4.18}$$

and

$$\frac{\tau_y}{\rho_0} = C_D \frac{\rho_{air}}{\rho_0} |W| W_y \tag{4.19}$$

where

τ_x, τ_y = wind stress in the x and y directions

$\frac{\rho_{air}}{\rho_0}$ = ratio of sir density to average density of seawater, 0.001293

$C_D = (0.75 + 0.067W)0.001$ = frictional drag coefficient

$|W|$ = magnitude of wind velocity

W_x, W_y = components of the wind velocity vector in the x and y directions

The PBL model does not compute pressure but rather determines the pressure gradient, however, ADCIRC requires a pressure file expressed as an equivalent height of water $P/(\rho_w g)$ as an input; therefore the PBL model has been modified to provide hourly wind stress and $P/(\rho_w g)$ values, where all data are linearly interpolated onto all nodal points in the finite element computational grid used by ADCIRC.

CHAPTER 5. MODEL SETUP

This chapter presents the model setup used in ADCIRC simulations. First, the forcings assigned to the open-ocean boundary and each computational nodal point over the mesh are discussed. In this study, 1) astronomic tides, 2) winds and pressures, and 3) storm surge hydrographs are prescribed individually or collectively. Next, the model parameters involved in the simulations, such as bottom friction and wetting and drying, are introduced. These model settings remain constant in all simulations (except when noted in Table 5.2).

5.1 Model Forcings

5.1.1 Astronomic Tides

Astronomic tides are the cyclical rise and fall of the ocean water level due to earth's gravitational interaction with the moon and sun. Tides are periodic in nature primarily due to the cyclical influence of the Earth's rotation and may be semidiurnal (two high waters and two low waters each day) or diurnal (one tidal cycle per day). In most locations along the coastline, the tides are semidiurnal; however, throughout much of the Gulf of Mexico, the tides are diurnal in their behavior. A tidal analysis is a linear regression of a sea level time series in terms of harmonic tidal constituents which can be represented as a superposition of multiple sinusoids. The amplitudes and phase lags for each tidal constituent are determined from the harmonic analysis.

For the WNAT-based models involving the Western North Atlantic, an open-ocean boundary at the 60 degree West meridian is assigned and forced with seven tidal forcings (K1, O1, M2, S2, N2, K2, Q1; Table 5.1) These same constituents are applied over the interior of the computational domain in the form of tidal potentials (Reid, 1990).

Table 5.1 Seven tidal constituents used to force the WNAT-based model

Constituent	Name	Period (hr)	Frequency (rad/s)
K1	Luni-solar diurnal	23.93	0.000072921158358
O1	Principal Lunar Diurnal	25.82	0.000067597744151
M2	Principal Lunar Semidiurnal	12.42	0.000140518902509
S2	Principal Solar Semidiurnal	12.00	0.000145444104333
N2	Larger Lunar Elliptic	12.66	0.000137879699487
K2	Luni-solar Semidiurnal	11.97	0.000145842317201
Q1	Larger Lunar Elliptic Diurnal	26.87	0.000064958541129

For the localized (i.e. inlet-based) model, an open-ocean boundary is assigned at the semi-circular boundary and forced with twenty-three tidal constituents (STEADY, MN4, SM, O1, K1, MNS2, 2MS2, N2, M2, 2MN2, S2, 2SM2, MN4, M4, MS4, 2MN6, M6, MSN6, M8, M10, P1, K2, and Q1; APPENDIX C). No tidal potential forcings are applied over the interior of the computational domain due to the local extent of the inlet-based mesh (Reid, 1990). Amplitudes and phases associated with the twenty-three tidal constituents listed in Appendix C are generated for the open-ocean boundaries of the localized domains, based on a harmonic analysis of a tide-driven simulation using the WNAT-based model domain.

5.1.2 Wind and Pressure

Storm surge is mainly driven by the sustained winds acting during a storm event. Further, due to the decreasing bathymetry as the coast is approached, storm surge can accumulate greatly in shallow coastal regions. It is evident that the meteorological influence caused by local winds and pressures should be included in a storm surge model.

Wind and pressure field data associated with Hurricane Katrina (for the dates August 23 to 30, 2005) (provided by Oceanweather Inc.) is incorporated into the numerical model. The provided data are 30-minute-sustained meteorological effects and are calculated by a tropical wind field model (TC96, Thompson and Cardone, 1996) governed by vertically averaged equations of motion that describe horizontal airflow through the planetary boundary layer. It is assumed that the structure of the tropical cyclone changes relatively slowly over time. TC96 calculates “snapshots” (in time) that represent distinct phases of the storm’s evolution. In order to determine a circularly symmetric pressure field centered at the eye of the storm, an exponential pressure law is employed (Holland, 1980). The extent of the wind and pressure field data coverage is shown in Figure 5.1, where it covers the WNAT-53K model domain in its entirety.

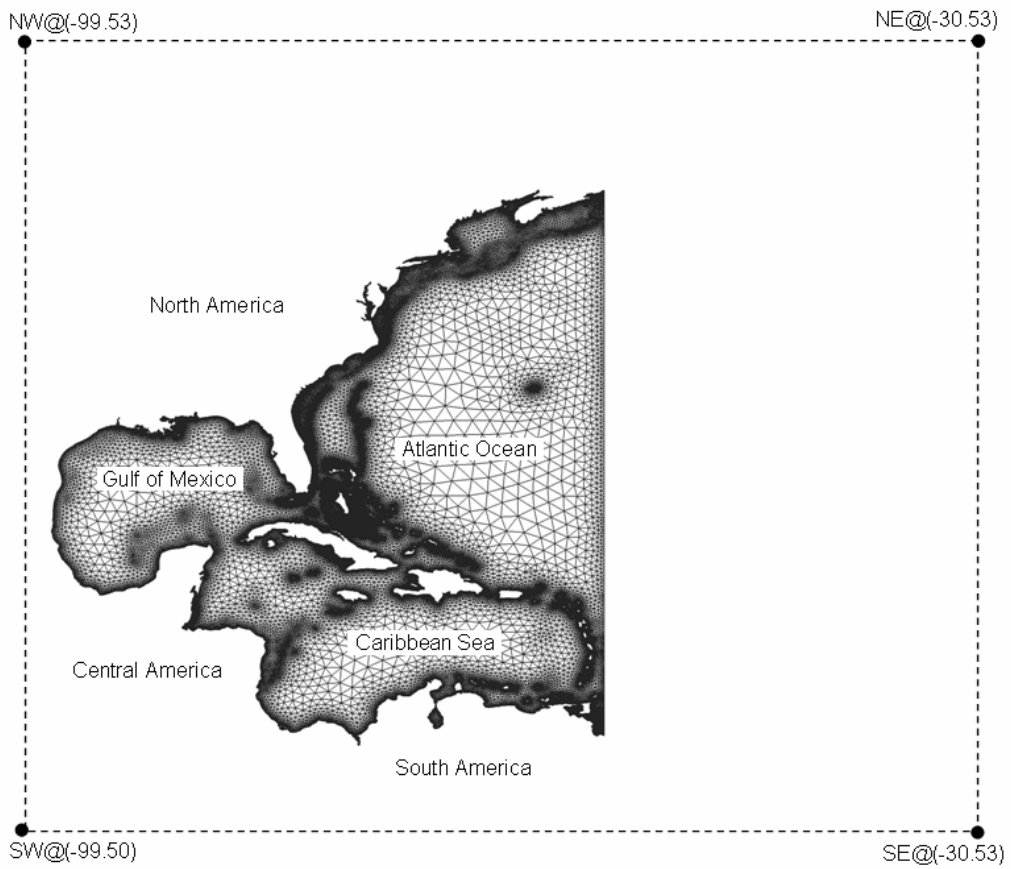

Figure 5.1 Wind Field Extent Shown Relative to the WNAT-Pascagoula Mesh. Note that all nodes of the mesh are located within the extent of the wind field.

The wind speeds (in the x- and y-directions) are transformed to wind stresses by using the relationship proposed by Garratt (1977):

$$\tau_s = \rho_u C_D V_{10}^2; \qquad C_D = 0.001(0.75 + 0.067 V_{10}) \tag{5.1}$$

where

ρ_u = density of air

C_D = wind speed-dependent wind drag coefficient

V_{10} = wind speeds acting 10 meters over the surface

The computed wind stresses are interpolated to the nodes of the mesh using a linear interpolation scheme. In order to transform the atmospheric pressures (in stress units) into equivalent water heights p_η, an inverted barometer effect is applied:

$$p_\eta = \frac{p_\sigma}{\rho_w g} \tag{5.2}$$

where

ρ_w = density of seawater

g = acceleration due to gravity

In the resulting file, a Single Meteorological Input File (fort.22, APPENDIX D), wind stresses and atmospheric pressures during Hurricane Katrina are specified at all grid nodes associated with the ADCIRC Grid and Boundary Information File (fort.14). Figure 5.2 and Figure 5.3 show the direction and magnitude of the wind speed associated with Hurricane Katrina at 02:30 GMT on August 29, 2005. The meteorological forcing data in fort.22 is read into the simulation every 30 minutes over the 7 day simulation period (August 23, 2005, 0:00 GMT to August 30, 0:00 GMT). Other principal parameters specified in the Model Parameter and Periodic Boundary Condition File (fort.15) are discussed in the following Section 5.2. Note that the open-ocean boundary specified in fort.14 must be changed to a land (no-flow) boundary if winds and pressures are used alone as boundary conditions.

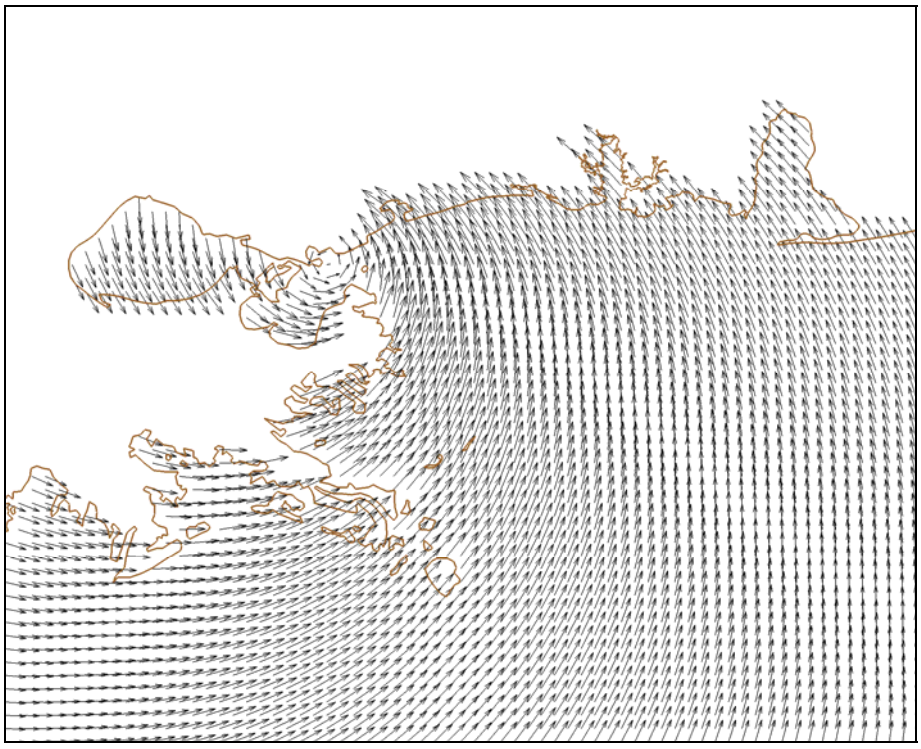

Figure 5.2 Direction of the wind

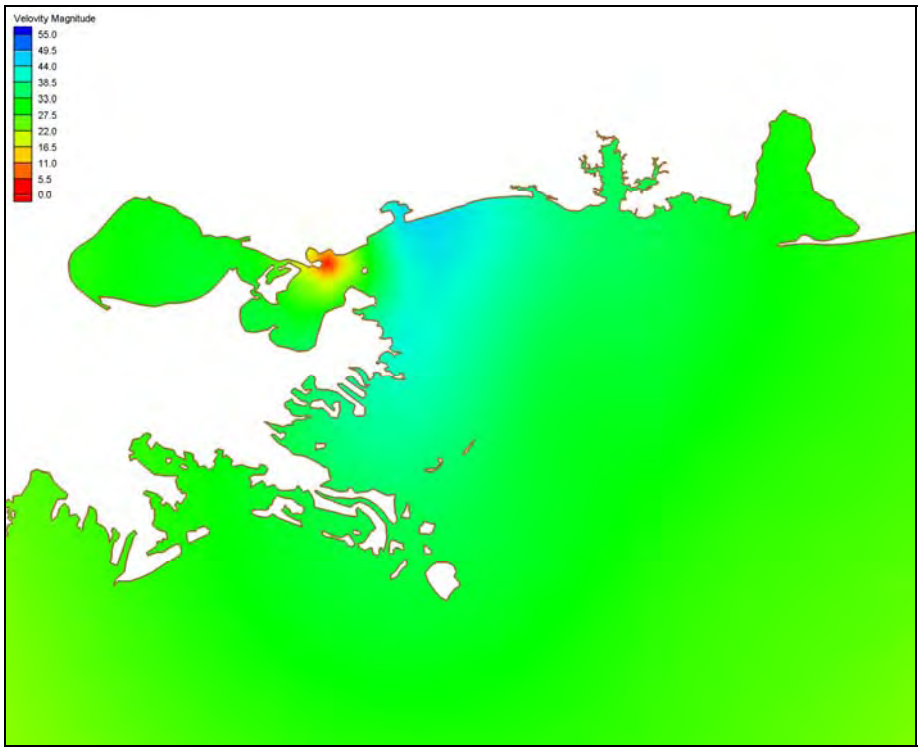

Figure 5.3 Magnitude of the wind

5.1.3 Storm Surge Hydrograph

A large-scale modeling approach that describes the hydrodynamics from the deep ocean into the local estuary ensures an adequate description of the storm surge dynamics (Bacopoulos et al., 2008); however, in order to increase computational efficiency while maintaining this level of accuracy, a localized domain (e.g. an inlet-based model) is selected as the operational storm surge model. Instead of applying wind and pressure data directly into the localized domain, the storm surge hydrograph approach allows for time varying elevation boundary conditions which are read from an input file (Non-periodic Elevation Boundary Condition File, fort.19). The elevation forcing data at specified nodes and incremental time step are described in the fort.19.

In order to obtain the elevation boundary conditions (fort.19) at the various open-ocean boundaries of the localized domains, Hurricane Katrina's wind and pressure data described in the previous section are applied to the WNAT-53K model domain. In this simulation, the open-ocean boundary of the localized mesh domain is specified as output locations for the generation of the storm surge hydrograph (Model Parameter and Periodic Boundary Condition File, fort.15). As a result, the elevation time series at the specified boundary output (fort.61) is obtained and used as an input forcing for the localized domain (fort.19). The calculated storm surge hydrographs that are applied to the open-ocean boundaries of the localized model domains are presented in Chapter 6.

5.2 Model Parameters

The following model parameterizations are set up in the Model Parameter and Periodic Boundary Condition File (fort.15): simulations are begun from a cold start; the wetting and drying algorithm is enabled with the minimum bathymetric depth set to 0.1 m. (i.e. computational nodes and the accompanying elements with water depths less than the prescribed minimum bathymetric depth are considered to be dry); the hybrid bottom friction formulation is employed varying the minimum bottom friction factor according to the simulation results that follow and specifying the remaining hybrid bottom friction parameter values as determined by Hagen et al. (2005a): $\boldsymbol{H_{break}} = 1.0\boldsymbol{m}$, $\boldsymbol{\theta} = 10$, and $\boldsymbol{\lambda} = \frac{1}{3}$; and the horizontal eddy viscosity is set to $5.0\boldsymbol{m}/\boldsymbol{s}^2$. Other principal parameters which vary depending on model domain and forcings are tabulated in Table 5.2. For the localized domains, a Cartesian coordinate system is used; the simulation period is 90 days for the astronomic tides and 7 days for Hurricane Katrina (e.g. winds and pressures and/or storm surge hydrographs) with 20- and 0.5-day ramping periods, respectively; the advection terms are turned off for the WNAT-based models and all Hurricane Katrina runs since the resulting velocities are not evaluated in this study. A computational time step is specified for each simulation to ensure that the Courant number criterion is satisfied throughout the computational domain.

$$\boldsymbol{C}_{\#} = \sqrt{\boldsymbol{gh}}\left(\frac{\Delta \boldsymbol{t}}{\Delta \boldsymbol{x}}\right) \leq 1.0$$

where

$\boldsymbol{C}_{\#}$ = Courant number

$\boldsymbol{g}$ = gravity acceleration

$\boldsymbol{h}$ = bathymetric depth

$\Delta\boldsymbol{t}$ = applied computational time step

$\Delta\boldsymbol{x}$ = nodal spacing

A zero-flux boundary condition (similar to infinite vertical walls) is applied to mainland coastlines and island shorelines and specified in the ADCIRC Grid and Boundary Information File (fort.14).

Table 5.2 Model Parameters

#	Domain	Forcing	Coordinate system	Simulation period (day)	Ramp period (day)	Time step (sec)	Advection	Tau0	Interior tidal potential forcing (*1)	Open ocean boundary tidal forcing (*1)
1	53K	TIDE	Spherical	90	20	5	OFF	0.006	7	7
2	53K	WIN/PRE	Spherical	7	0.5	0.5	OFF	-0.01	0	0
3	WNAT-based	WIN/PRE	Spherical	7	0.5	0.5	OFF	-0.01	0	0
4	Inlet-based	TIDE	Cartesian	60	20	0.5	ON	0.006	0	23
5	Inlet-based	SSH B.C.	Cartesian	7	0.5	0.5	OFF	-0.01	0	0
6	Inlet-based	SSH B.C. + Win&Pre	Cartesian	7	0.5	0.5	OFF	-0.01	0	0

*1 : number of tidal coefficients

(τ_0 is the GWCE weighting parameter.)

CHAPTER 6. MODEL RESULTS

This chapter presents the ADCIRC model results. Table 6.1 shows a summary of the simulations conducted in this study. First, the inlet-based floodplain meshes (FP1.5_INLET_A and FP1.5_INLET_B in Table 3.1) are each applied in a tidal simulation (Experiments No.1 and No.2). The floodplain (tide-only) model results are compared with the preliminary in-bank (tide-only) model results to observe the effect of the inundation areas on tidal elevations in the Pascagoula River. Next, Experiments No.3 and No.4 apply winds and pressures over the WNAT-53K and FP1.5_WNAT_B model domains, respectively. Products of Experiments No.3 and No.4 will be storm surge hydrographs which will be used as boundary forcings for the inlet-based model applications performed in Experiments No.5, No.6, and No.7. Experiment No.5 examines the inlet-based 1.5-m floodplain model (FP1.5_INLET_B in Table 3.1) that is forced by storm surge hydrograph provided by using the WNAT-53K mesh domain at the open-ocean boundary. Next, the storm surge hydrographs produced from Experiment No.4 are applied on the inlet-based model: Experiment No.6 uses a hydrograph only; Experiment No.7 uses the hydrograph in combination with a local wind and pressure forcing.

Table 6.1 Simulation Table

	Domain			Forcing	
Experiments #	Pascagoula Floodplain	Ocean extent	Islands (*1)	Surface	Boundary
1	1.5	INLET	A	None	TIDE
2	1.5	INLET	B	None	TIDE
3	-	WNAT-53K	A	Win/Pre	None
4	1.5	WNAT-53K	B	Win/Pre	None
5	1.5	INLET	B	None	Hydrograph from Experiment 3
6	1.5	INLET	B	None	Hydrograph from Experiment 4
7	1.5	INLET	B	Win/Pre	Hydrograph from Experiment 4

(*1) A: islands with no-flow boundary
B: meshed over islands

6.1 Astronomic Tide Simulation (Experiments 1 and 2)

In order to assess the model in terms of astronomic tide simulation, visual interpretations of tidal resynthesis plots and statistical measures are utilized. Tidal resynthesis plots display 14-day resyntheses of historical and model tidal constituents. (This 14-day time period is chosen in order to include a complete spring-neap tidal cycle in the tidal resynthesis.) Historical data were obtained from two NOS stations and five USGS stations (Figure 6.1 and Table 6.2). The thirty-seven tidal constituents associated with the historical NOS data are listed in APPENDIX C. At the USGS stations, water level data with a total length of 31-day were utilized to perform the harmonic analysis. Thirty-five tidal constituents were extracted using a least-squares fitting procedure called T_TIDE (Pawlowicz et al., 2002). Lastly, the tidal results in ADCIRC are harmonically analyzed using the 23 tidal constituents listed in APPENDIX C.

Each tidal signal is resynthesized through the following summation:

$$T(z) = Z_0 + \sum_N H_n f_n \cos\left[\omega_n t - g_n + \left(V_n + u_n\right)\right]$$

where

Z_0 = local mean sea level (MSL)

(H_n, g_n) = (tidal constituent amplitude and phase)

Also, the nodal adjustment factors are given as f_n and u_n and the terms $\omega_n t$ and V_n together determine the phase angle of the equilibrium tidal constituent. V_n is the equilibrium phase angle for the tidal constituent at the arbitrary time origin. The accepted convention is to take V_n as the Prime Meridian and t in the standard time zone of the observation station.

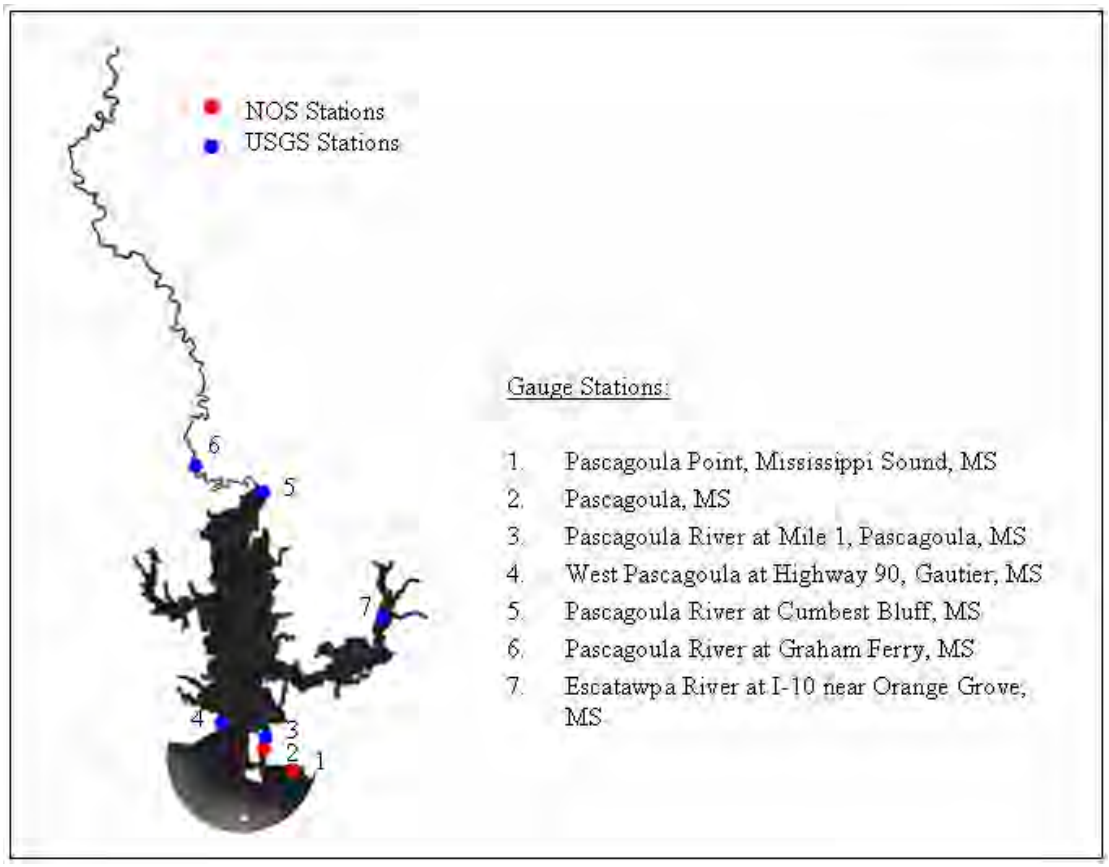

Figure 6.1 Historical Data Stations

Table 6.2 Historical Data Stations

#	Longitude (*1)	Latitude (*2)	Station Name	
1	-88.533333333	30.340000000	NOS Harmonics Station 8741196	Pascagoula Point, Mississippi Sound, MS
2	-88.566666667	30.358333333	NOS Harmonics Station 8741533	Pascagoula, MS
3	-88.608889000	30.382778000	USGS Water Levels Station 02480285	West Pascagoula at Highway 90, Gautier, MS
4	-88.563403550	30.367986665	USGS Water Levels Station 02480212	Pascagoula River at Mile 1, Pascagoula,MS
5	-88.451389000	30.458611000	USGS Water Levels Station 0248018020	Escatawpa River at 1-10 near Orange Grove, MS
6	-88.570000000	30.583889000	USGS Water Levels Station 02479330	Pascagoula River at Cumbest Bluff, MS
7	-88.641389000	30.610556000	USGS Water Levels Station 02479310	Pascagoula River at Graham Ferry, MS

(*1) spherical coordinates in degrees of longitude (east of Greenwich is positive and west of Greenwich is negative)

(*2) spherical coordinates in degrees of latitude (north of the equator is positive and south of the equator is negative)

Wang (2008) has suggested that incorporating the marsh areas into the preliminary in-bank mesh may yield more accurate results in the tidal resynthesis; therefore, this section demonstrates an improved inlet-based astronomic tide model for the Pascagoula River using floodplain meshes, FP1.5_INLET_A and FP1.5_INLET_B (Figure 3.6 to Figure

3.8). Recall that the FP1.5_INLET_A mesh describes river islands as no-flow boundaries while the FP1.5_INLET_B mesh describes river islands with elements that are allowed to wet and dry.

Figure 6.2 to Figure 6.5 show resynthesized plots at the seven recording stations based on the model output from Experiments 1 and 2. The first four stations (shown in Figure 6.2 and Figure 6.3) reveal little difference for when the inundation areas are included in the model domain. (We note that for station No.1 at Pascagoula, MS, no model result is provided for the FP1.5_INLET_B mesh application since the location dries out during the simulation.) While there is a slight improvement in the model result at Station No.4 (Gautier, MS) (see Figure 6.3), we conclude that tidal elevations near the coast are dominated by the deep-ocean tide and are weakly influenced by the inundation areas. On the other hand, the upstream locations (Station Nos. 5-7) are shown to be strongly influenced by the inundation areas (see Figure 6.4 and Figure 6.5). There is a significant reduction in the modeled tidal amplitude, which can be explained by the wetting and drying that is occurring in the floodplains. The wetting and drying of the inundation areas also appears to have an effect on the phase of the tide in the upstream regions of the Pascagoula River. Not only do the marsh areas of the Lower Pascagoula River need be included in the computational domain (see modeled tide results for Stations 5 and 6 in Figure 6.4), but the inundation areas lying adjacent to the Escatawpa River need be considered (see modeled tide results for Station 7 in Figure 6.5).

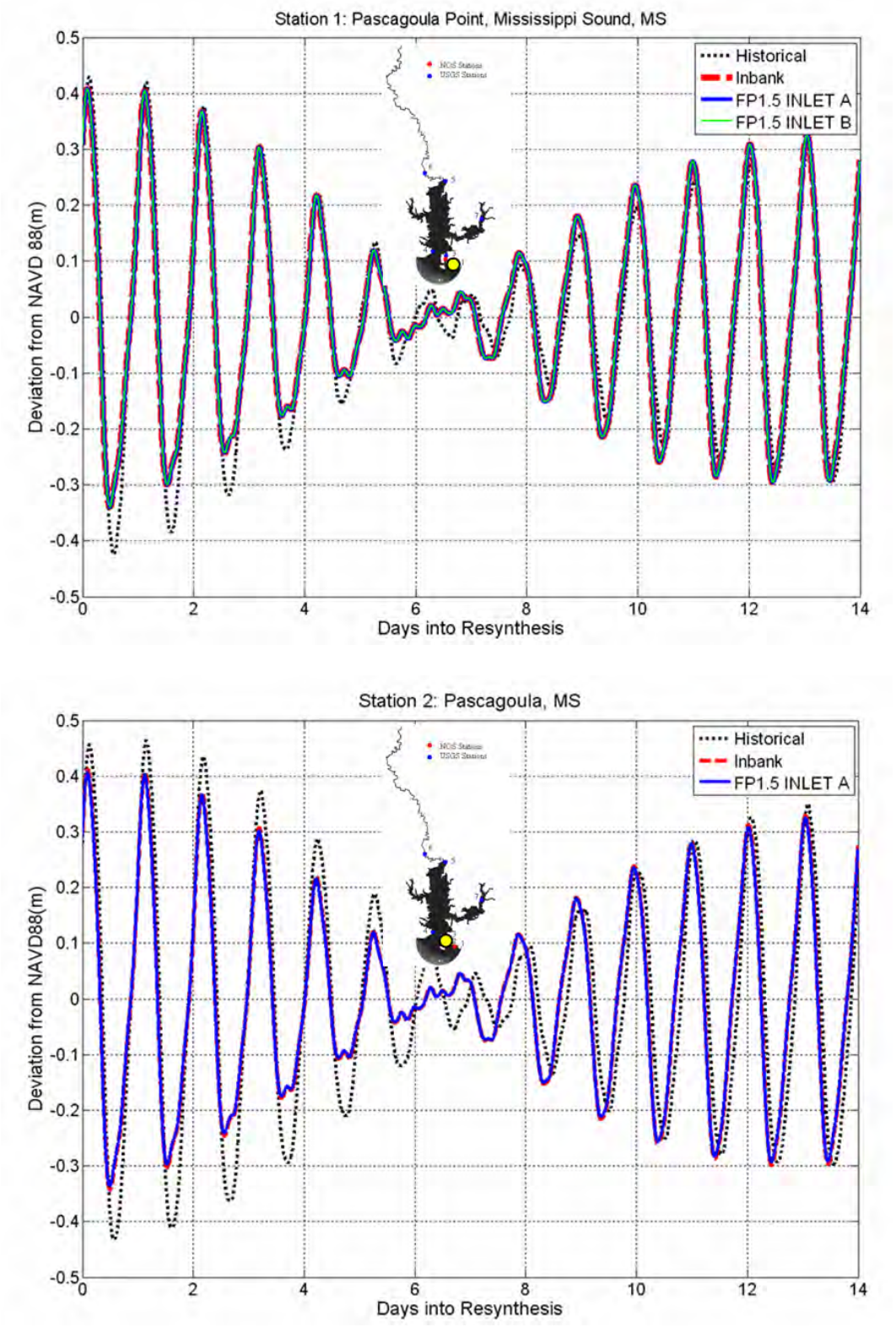

Figure 6.2 Resyntheses of historical and model tidal constituents, corresponding to the stations located at Pascagoula Point, Mississippi Sound, MS and Pascagoula, MS.

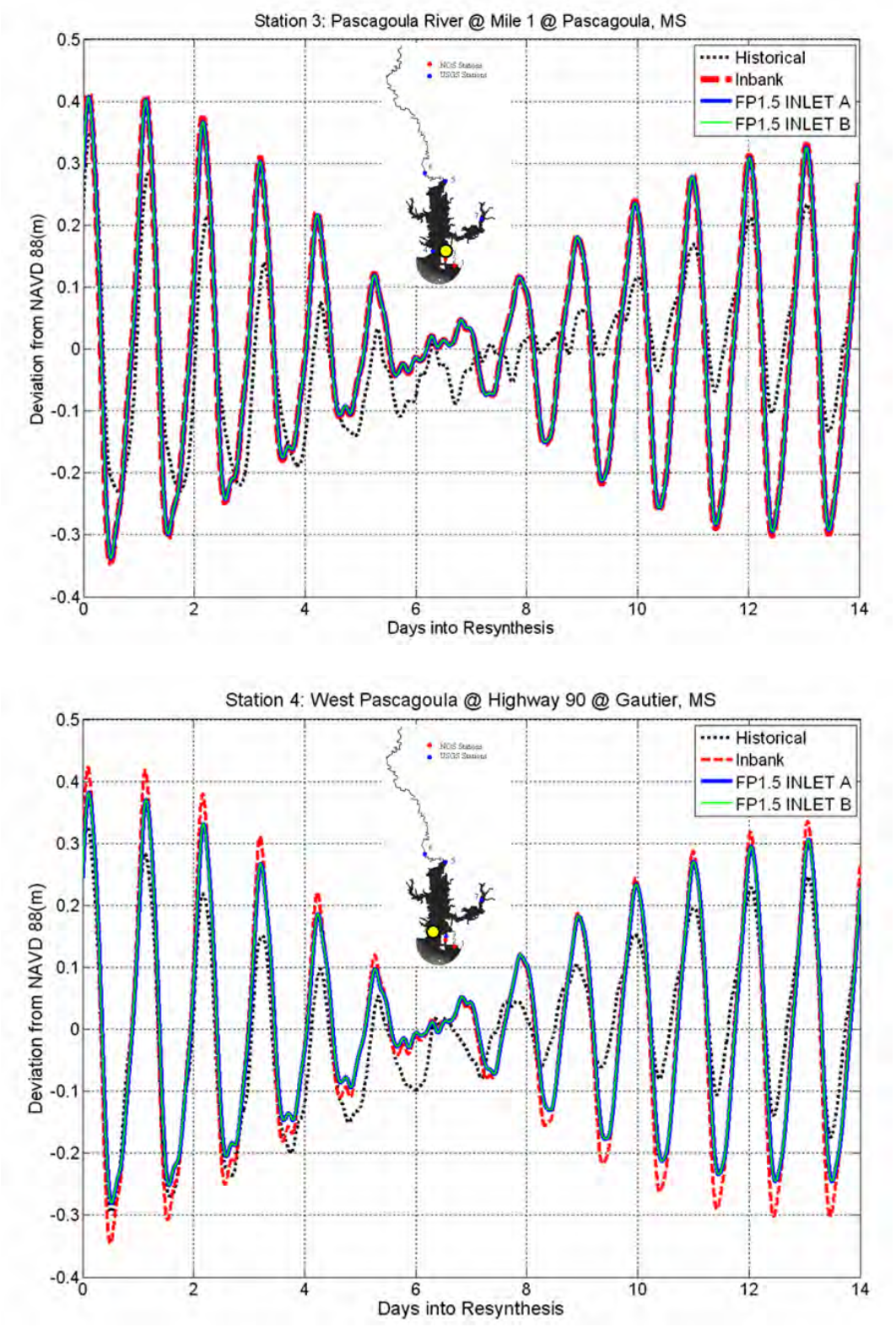

Figure 6.3 Resyntheses of historical and model tidal constituents, corresponding to the stations located at Pascagoula River Mile 1, MS and West Pascagoula at Gautier, MS.

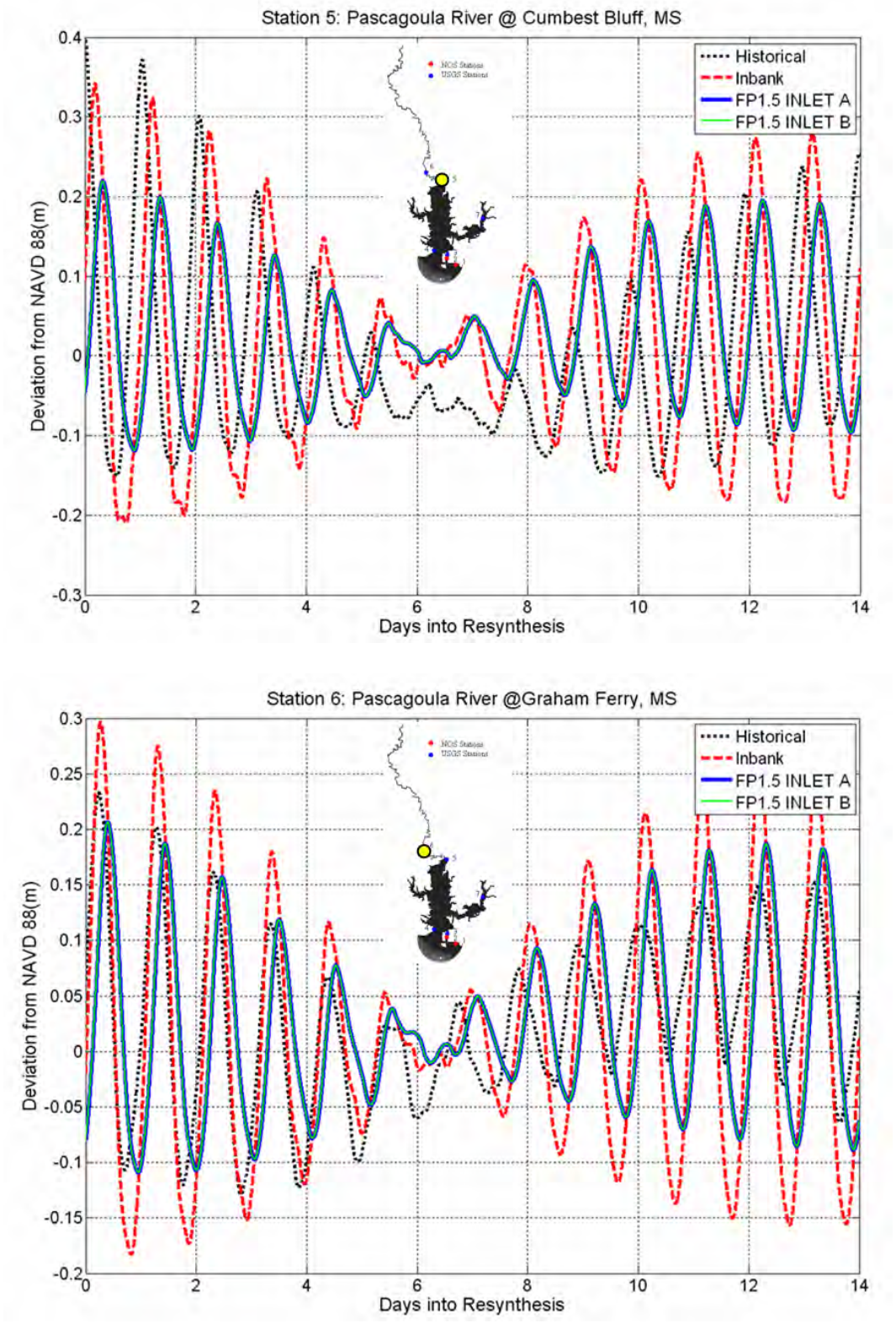

Figure 6.4 Resyntheses of historical and model tidal constituents, corresponding to the stations at Pascagoula River at Cumbest Bluff and Graham Ferry, MS.

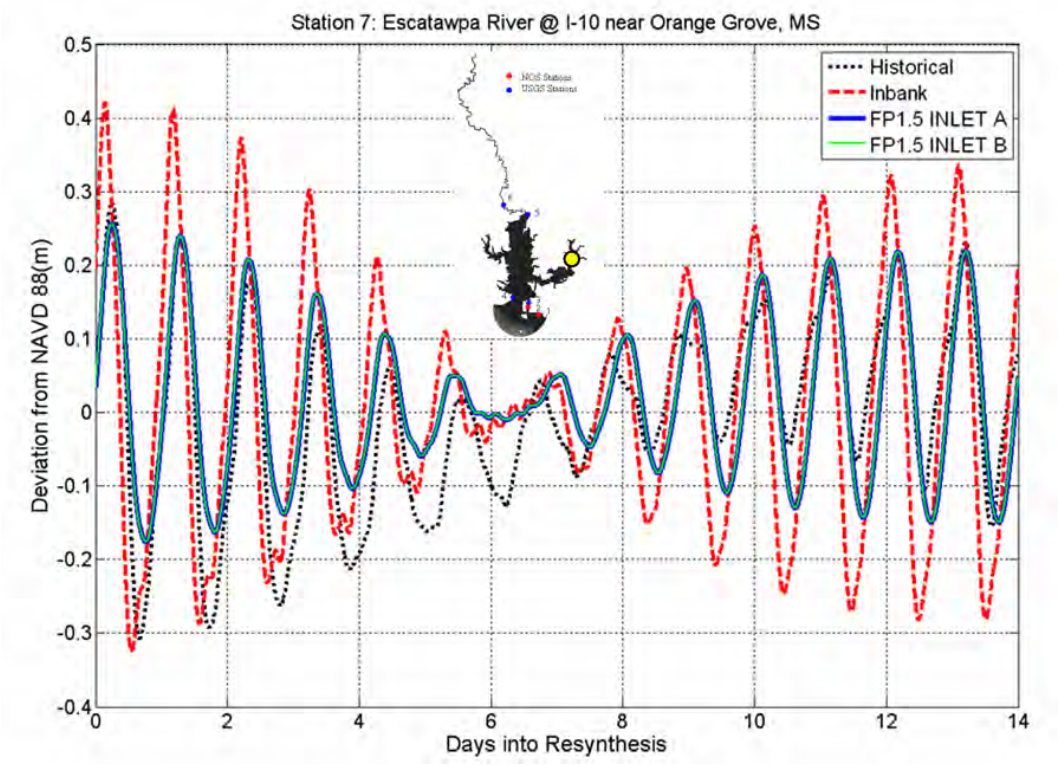

Figure 6.5 Resyntheses of historical and model tidal constituents, corresponding to the station located at Escatawpa River at I-10 near Orange Grove, MS.

6.2 Storm Surge Model

6.2.1 WNAT-based Model and Storm Surge Hygrograph Extraction (Experiments 3 and 4)

In order to obtain storm surge hydrographs (elevation variance) at the open-ocean boundary locations associated with the localized domain, a large-scale modeling approach will utilize high-resolution wind and pressure fields of Hurricane Katrina. First, Experiment 3 applies winds and pressures over the WNAT-53K model domain to produce results (storm surge hydrographs) at the ninety-nine open-ocean boundary nodes of inlet-based mesh (Figure 6.6). Then Experiment 4 applies winds and pressures over the WNAT-based Pascagoula floodplain mesh (FP1.5_WNAT). It should be noted that the WNAT-53K mesh contains a coarse discretizations of the Gulf Coast with Mississippi barrier islands assigned as no-flow boundaries while the FP1.5_WNAT mesh employs a refined coastline and meshes over barrier islands to allow for storm surge overtop.

Figure 6.7 to Figure 6.17 show calculated storm surge hydrographs at ten (of the ninety-nine) boundary nodes by both Experiments 3 and 4. Since the landfall position of Hurricane Katrina located west of the study area, the modeled surge height is the highest at the position 1, which is about 3.5 m (Figure 6.7). Then the modeled height of the storm surge gradually decreases as one progresses eastward on the open-ocean boundary (i.e. from number 1 to 99). Each result shows that the modeled surge level of the WNAT-53K model domain (in red line) is higher than the model surge level produced by the FP1.5_WNAT mesh (in blue dashed line). In fact, for the greatest storm surge height on the westernmost point of the open-ocean boundary, the WNAT-53K mesh can over-

predict the water level (relative to that produced by the FP1.5_WNAT mesh) by nearly as much as 0.5 meter. There are multiple suggestions for the significant differences in the storm surge hydrographs presented in Figure 6.7 to Figure 6.17. First, the FP1.5_WNAT mesh contains a high-resolution description of the inland waterbody and floodplain features of the Pascagoula River, where the WNAT-53K mesh does not include the estuary. Second, the coastline boundary of the FP1.5_WNAT mesh has been refined to more closely follow the true coastline, where the WNAT-53K mesh utilizes a coarse resolution that does not sufficiently capture the intricate coastline geometry. The barrier islands protecting the Pascagoula River are described as no-flow boundaries in the WNAT-53K mesh. Meshing over the barrier islands in the FP1.5_WNAT mesh permits for the storm surge to overtop the barrier islands. It is argued that the no-flow boundaries used by the WNAT-53K mesh allows for the storm surge to accumulate to greater heights because the flow is more confined by the no-flow boundaries, whereas the FP1.5_WNAT mesh permits for the storm surge to propagate over the barrier islands and into the estuary (Salisbury and Hagen, 2007).

Figure 6.7 to Figure 6.17 show calculated storm surge hydrographs at ten boundary nodes by both Experiments. Since the landfall position of Hurricane Katrina located west of the study area, the modeled surge height is the highest at the position 1, which is about 3.5 m (Figure 6.7). Then the modeled height of the storm surge gradually decreases toward east (i.e. number 1 to 99). Each result shows the modeled surge level of 53K domain (in red line) is higher than the level of FP1.5_WNAT (in blue dash line). The difference is caused by: 1) entire mesh resolution: FP1.5_WNAT, a high-resolution flood plain mesh,

is able to incorporate Katrina's winds and pressures more accurately; 2) coastline geometry captured in the mesh: FP1.5_WNAT has refined coastline and some estuary features (i.e. bays); 3) no-flow boundaries: The 53K domain does not include the Pascagoula River and has a land boundary instead. Also Mississippi barrier islands located at the south of the Port of Pascagoula are assigned as no-flow island boundary. Therefore, the estuary is closely assumed it has a vertical wall at the boundary of coastline and barrier islands, so the water level increases.

Figure 6.18 shows the maximum envelopes of water (i.e. maximum height of the storm surge) determined in the WNAT-53K and FP1.5_WNAT mesh applications. A small water surface variance is observed along the hurricane track (visible in Figure 6.18 as the white-colored trail) and both applications (WNAT-53K; FP1.5_WNAT) show a maximum storm surge height of 6.5 m near the Biloxi Bay. Also, it becomes apparent that the barrier islands and local Pascagoula features influence the Gulf Coast storm surge dynamics.

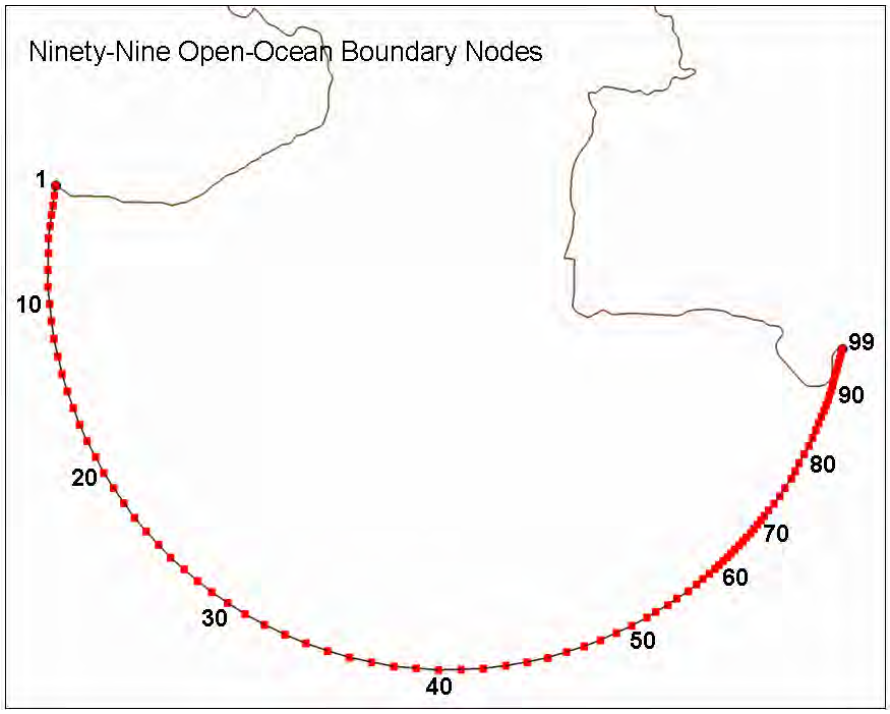

Figure 6.6 Ninety-nine Open Ocean Boundary Nodes of FP1.5_INLET Model

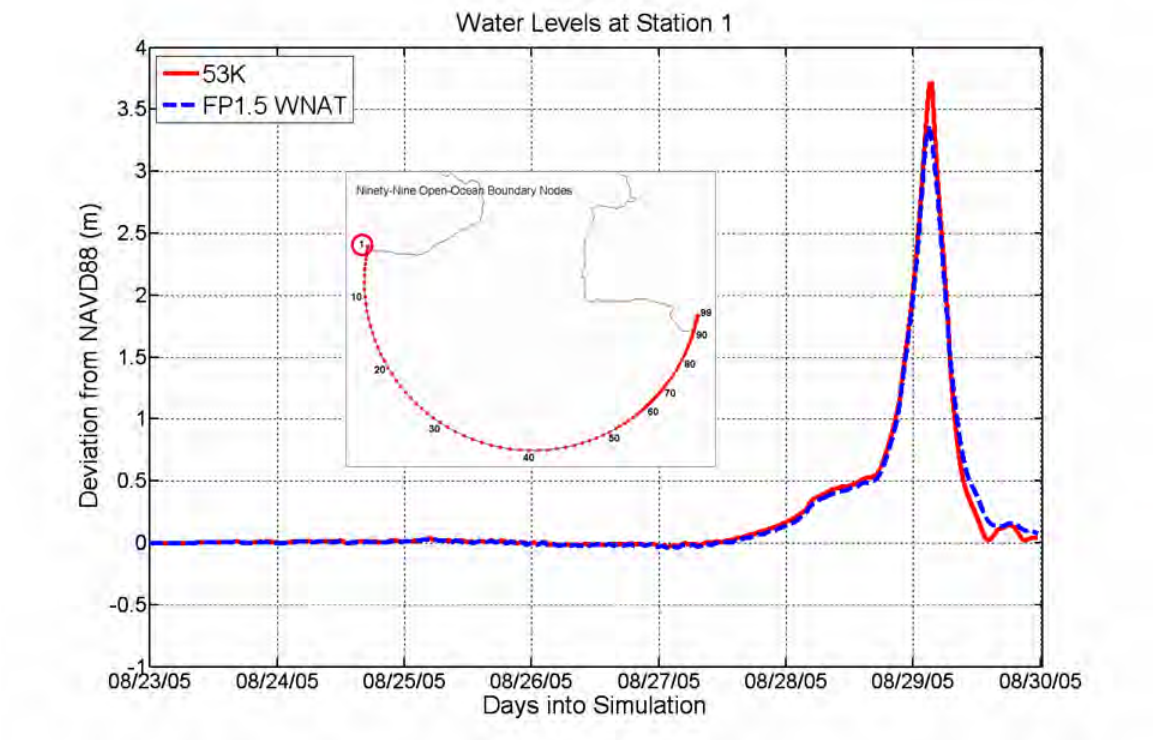

Figure 6.7 Storm Surge Hydrograph at Open-ocean Boundary Node 1

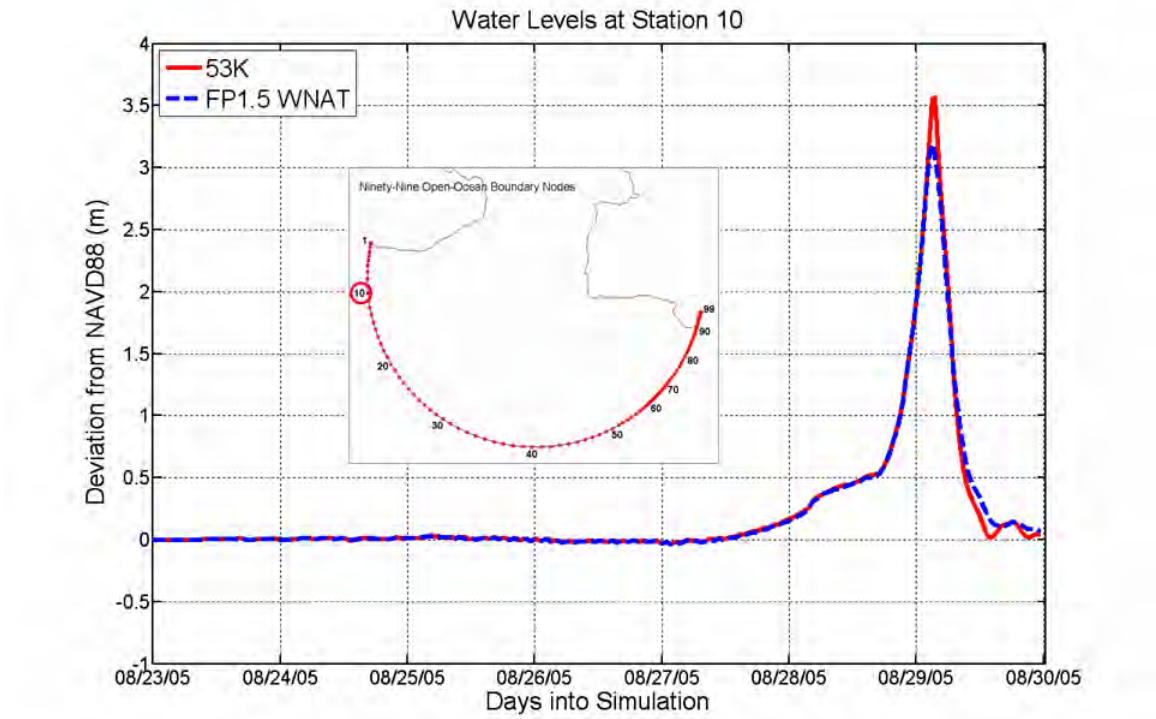

Figure 6.8 Storm Surge Hydrograph at Open-ocean Boundary Node 10

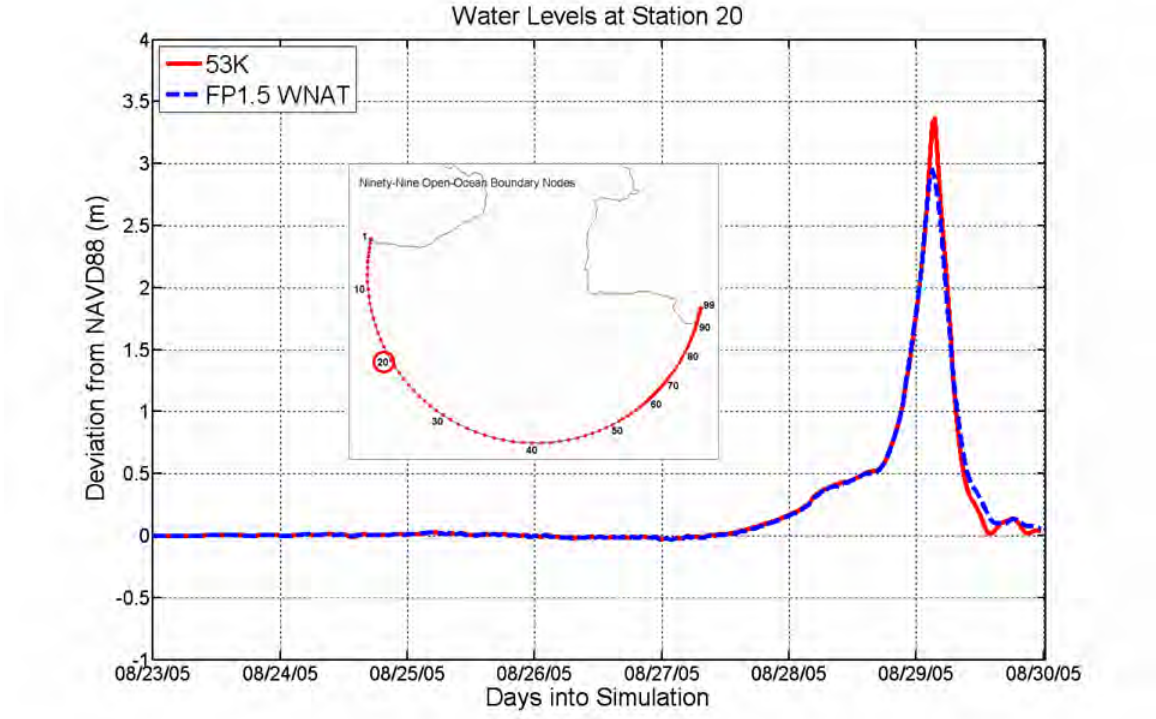

Figure 6.9 Storm Surge Hydrograph at Open-ocean Boundary Node 20

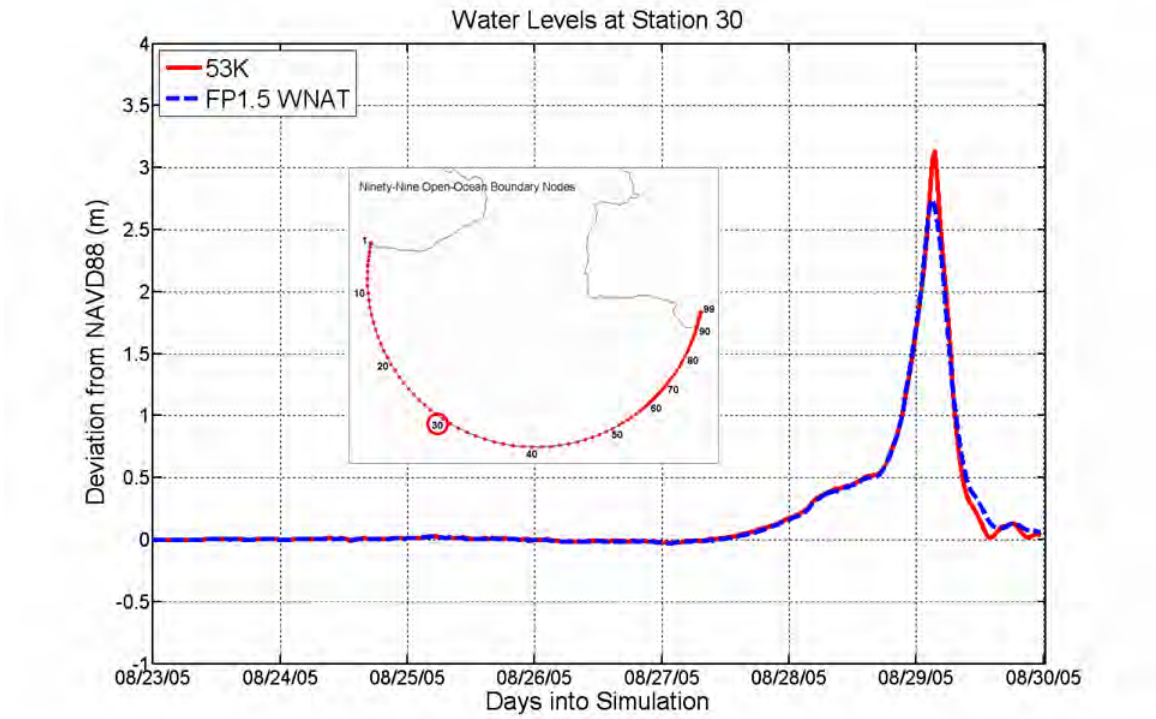

Figure 6.10 Storm Surge Hydrograph at Open-ocean Boundary Node 30

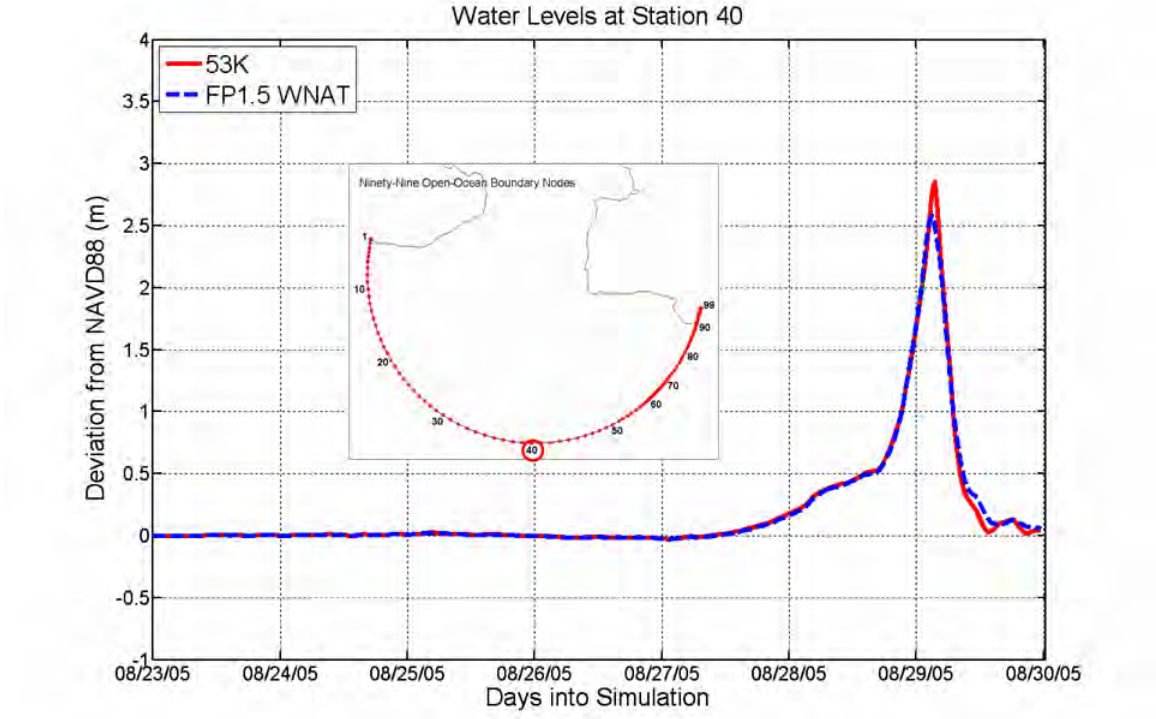

Figure 6.11 Storm Surge Hydrograph at Open-ocean Boundary Node 40

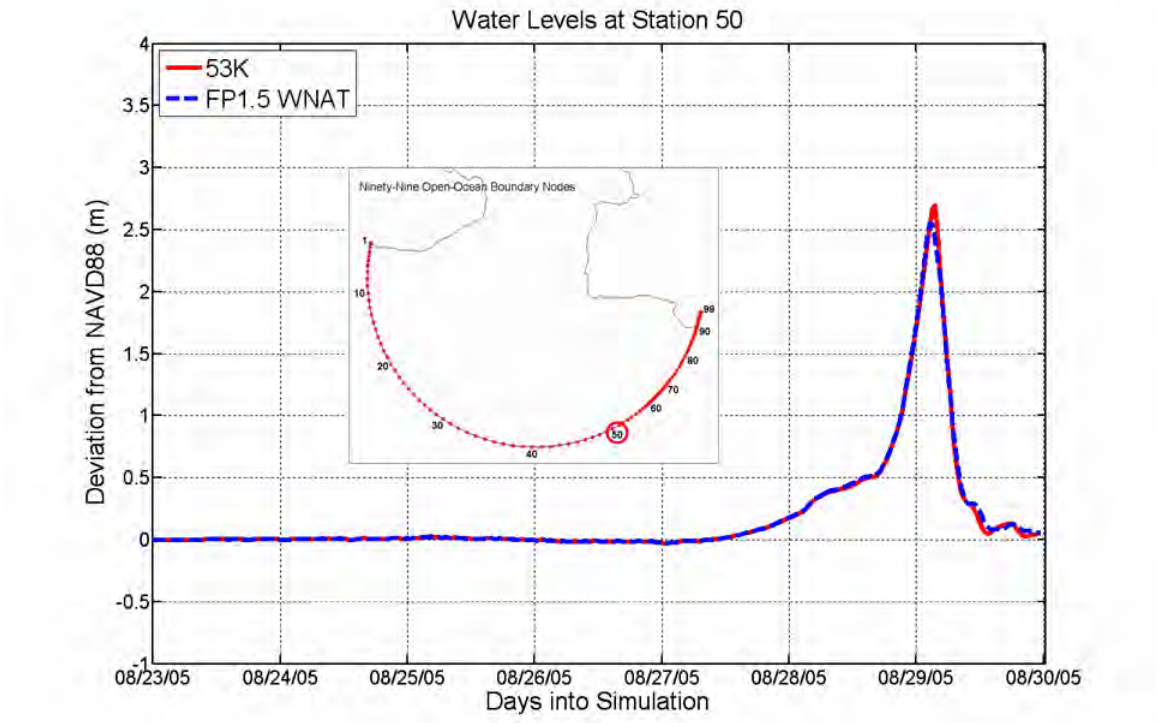

Figure 6.12 Storm Surge Hydrograph at Open-ocean Boundary Node 50

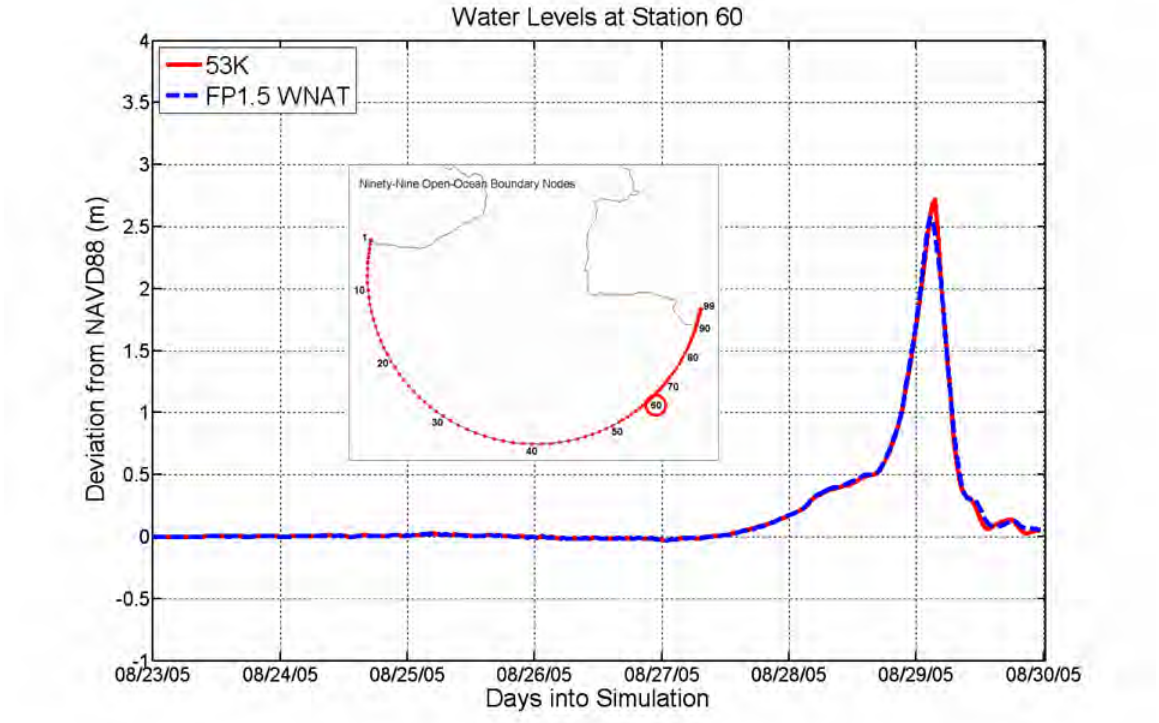

Figure 6.13 Storm Surge Hydrograph at Open-ocean Boundary Node 60

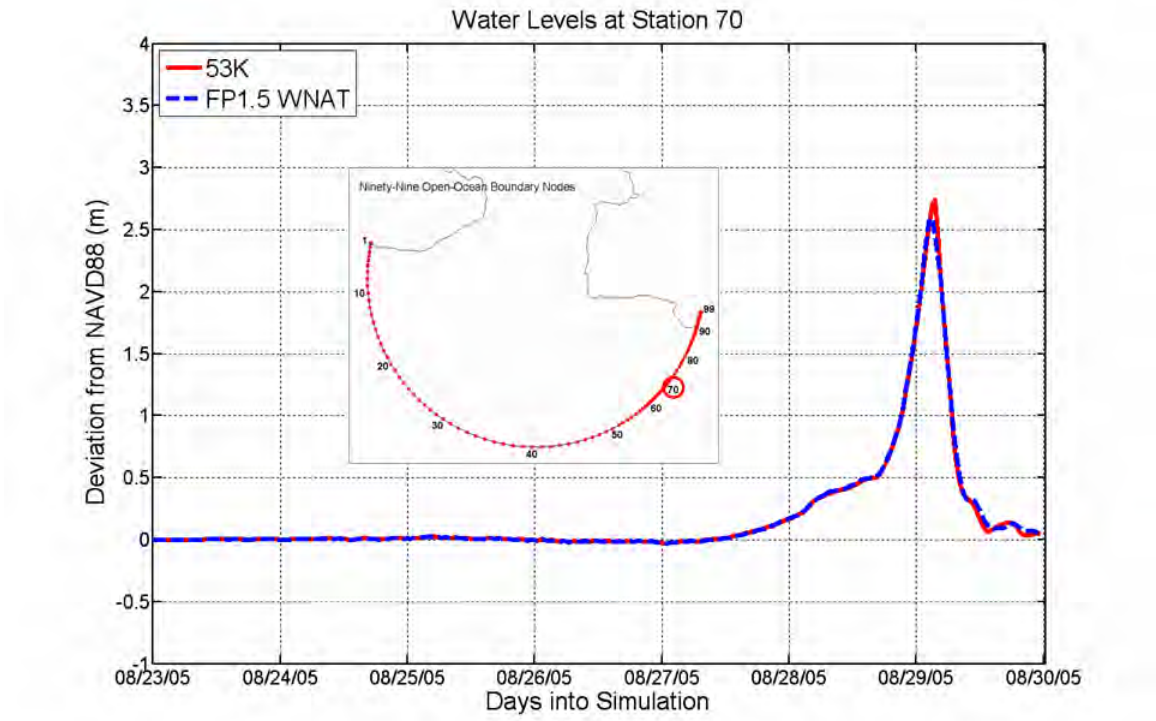

Figure 6.14 Storm Surge Hydrograph at Open-ocean Boundary Node 70

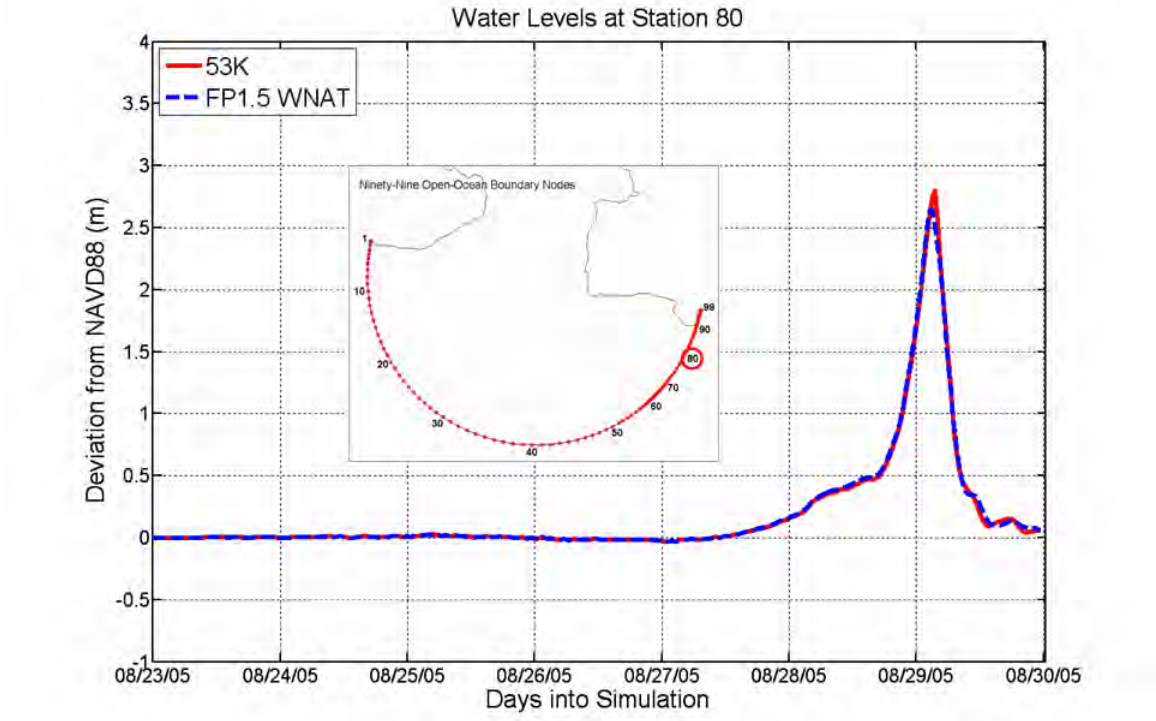

Figure 6.15 Storm Surge Hydrograph at Open-ocean Boundary Node 80

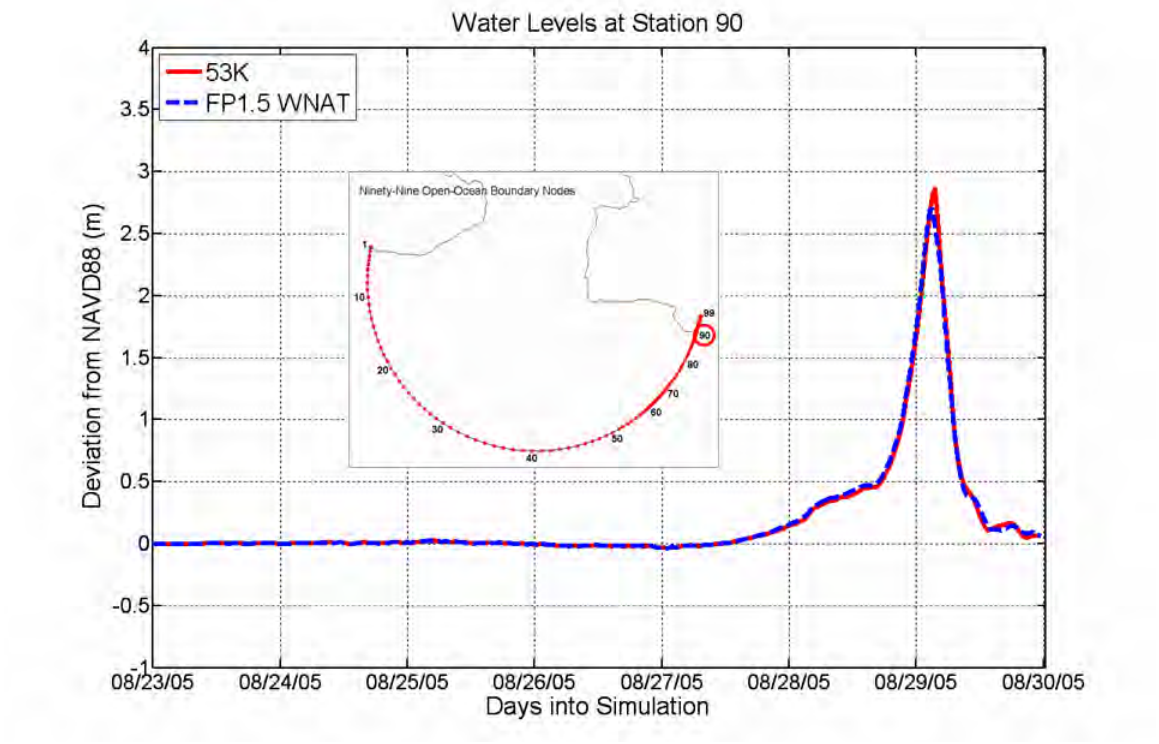

Figure 6.16 Storm Surge Hydrograph at Open-ocean Boundary Node 90

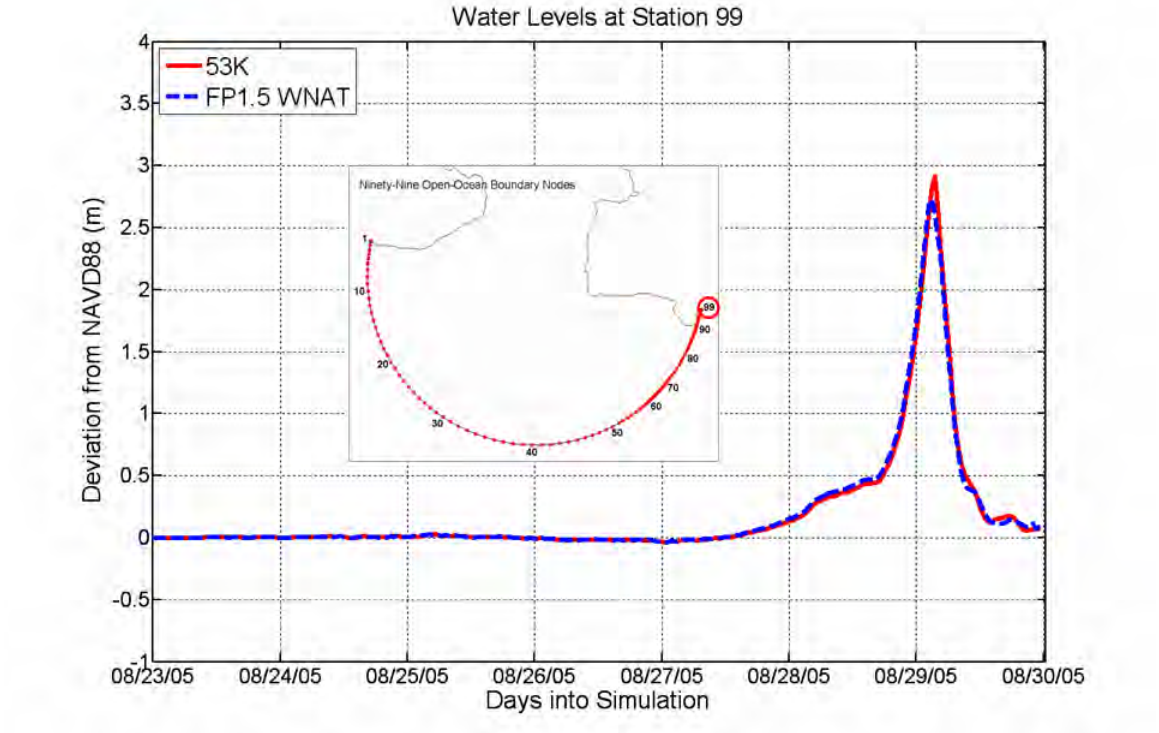

Figure 6.17 Storm Surge Hydrograph at Open-ocean Boundary Node 99

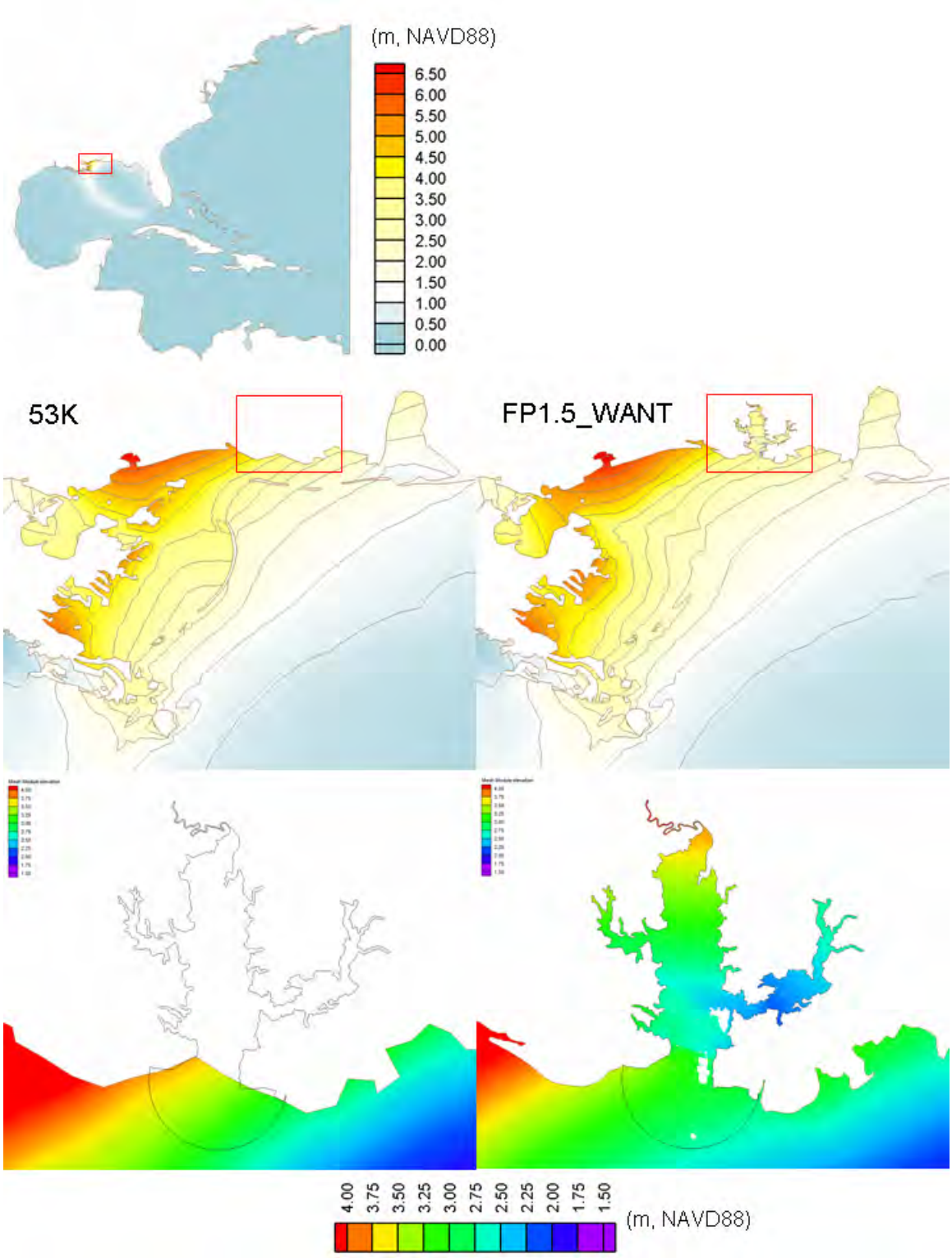

Figure 6.18 Maximum Envelop of Water (Top) FP1.5_WNAT model forced by global wind and pressure; (Middle left& right) Insets of Gulf Coast in 53K and FP1.5_WNAT model; (Bottom left& right) Insets of Pascagoula Estuary in 53K and FP1.5_WNAT model

6.2.2 Inlet-based Model with Storm Surge Hydrographs (Experiments 5 and 6)

Experiments 5 and 6 utilize the inlet-based domain, FP1.5_INLET, which has ninety-nine nodes on its open-ocean boundary and is forced by storm surge hydrographs calculated by the previous experiments (Nos. 3 and 4) involving the large-scale domains. Model output from the FP1.5_INLET mesh applications (see Experiments 5 and 6 of

Table 6.1) is provided for ten stations (see Figure 6.19 to Figure 6.28). The FP1.5_INLET model output (for when it is forced by a hydrograph calculated by the WNAT-53K mesh) is represented by a red solid line and the FP1.5_INLET model output (for when it is forced by a hydrograph calculated by the FP1.5_WNAT mesh) is represented by a blue dashed line. For each station, the FP1.5_INLET model result (for when it is forced by a hydrograph calculated by the WNAT-53K mesh) over-predicts relative to the FP1.5_INLET model result (for when it is forced by a hydrograph calculated by the FP1.5_WNAT mesh), where it is clear that this observation results from the boundary condition.

Figure 6.29 shows the maximum envelopes of water (i.e. maximum height of the storm surge) for the FP1.5_INLET mesh applications, for when the model is forced by the two different hydrographs (that generated by the WNAT-53K mesh application and that generated by the FP1.5_WNAT mesh application). For both cases, maximum elevations are obtained on the west side of the model domain where the greatest influence from Hurricane Katrina is located. A difference between the two maximum envelopes of water is calculated to highlight regions where the solutions differ. The difference image indicates positive values in warm (yellow) color, indicative of regions where the FP1.5_INLET mesh application (for when it is forced by a hydrograph calculated by the WNAT-53K mesh) over-predicts relative to the FP1.5_INLET mesh application (for when it is forced by a hydrograph calculated by the FP1.5_WNAT mesh).

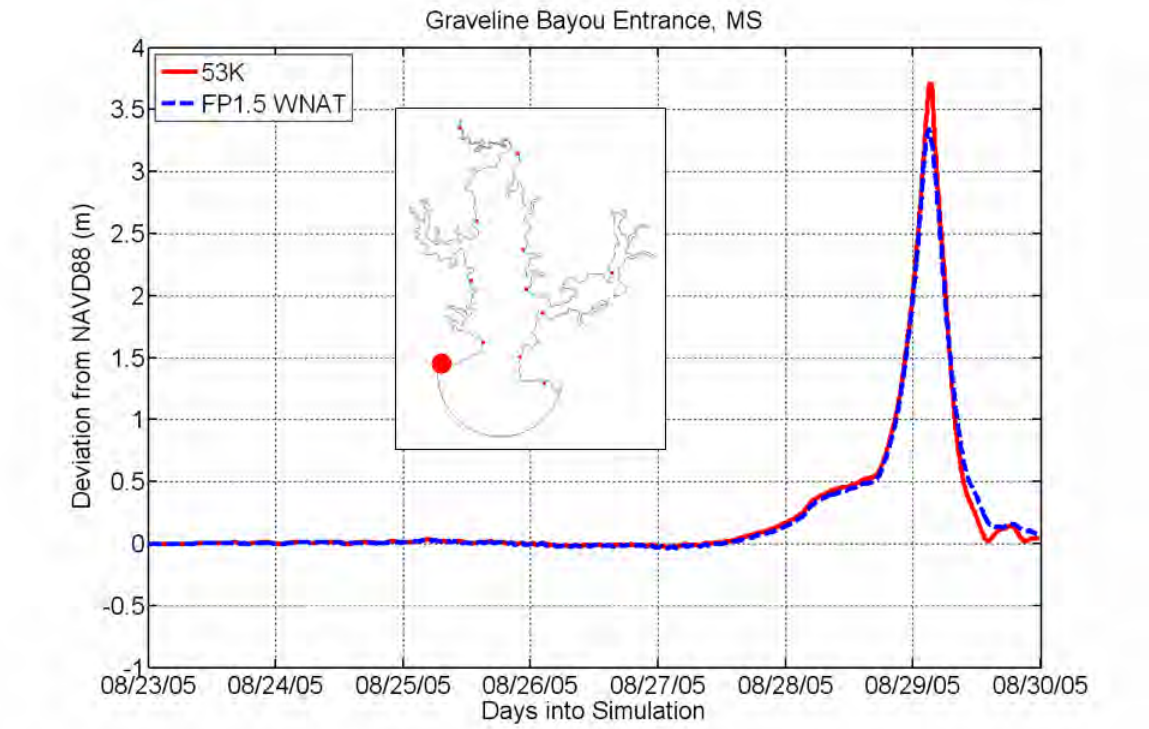

Figure 6.19 Model Storm Surge Hydrograph at Graveline Bayou Entrance, MS

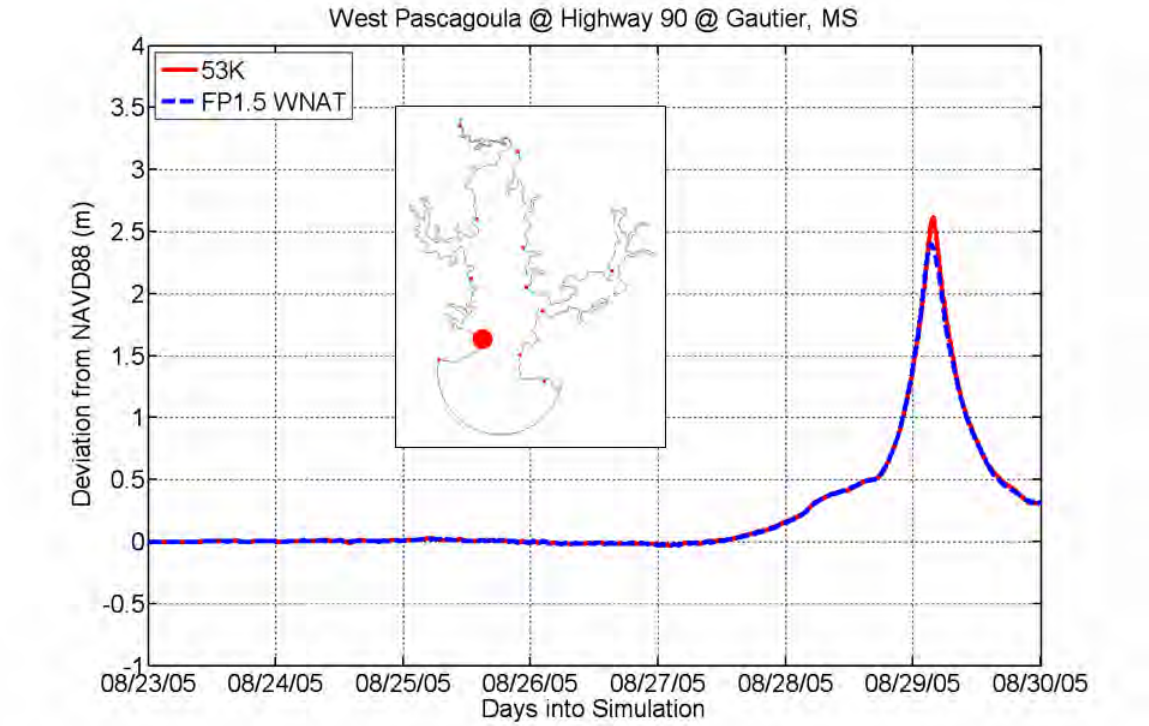

Figure 6.20 Model Storm Surge Hydrograph at West Pascagoula @ Highway 90 @ Gautier, MS

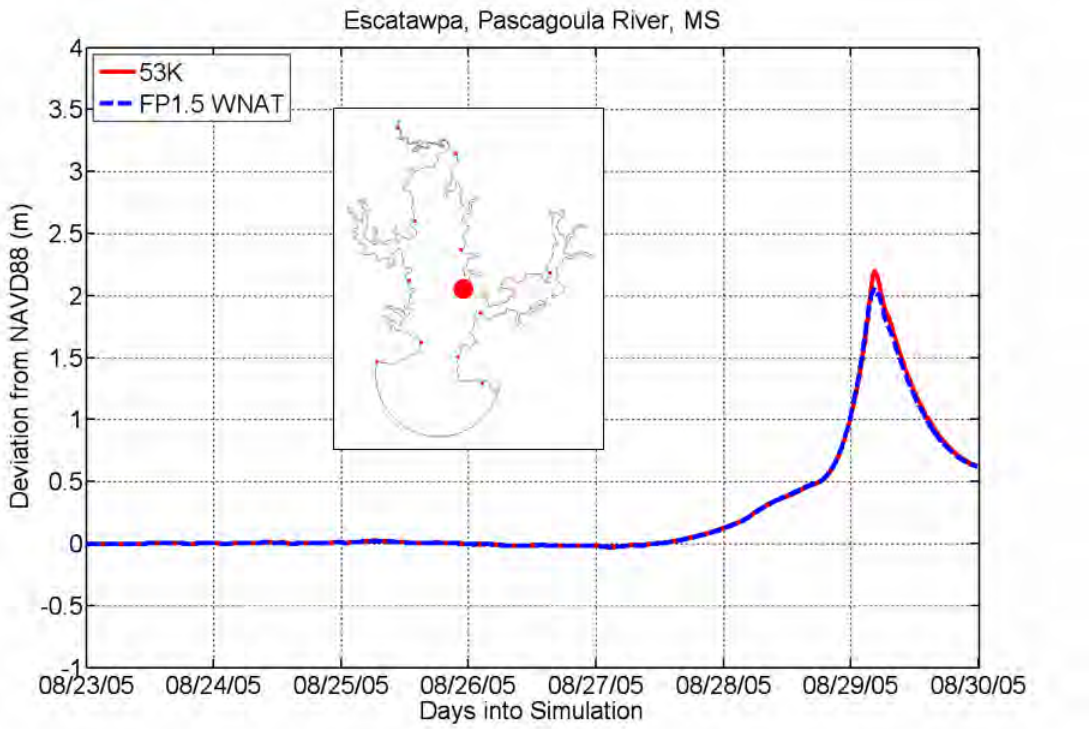

Figure 6.21 Model Storm Surge Hydrograph at Escatawpa, Pascagoula River, MS

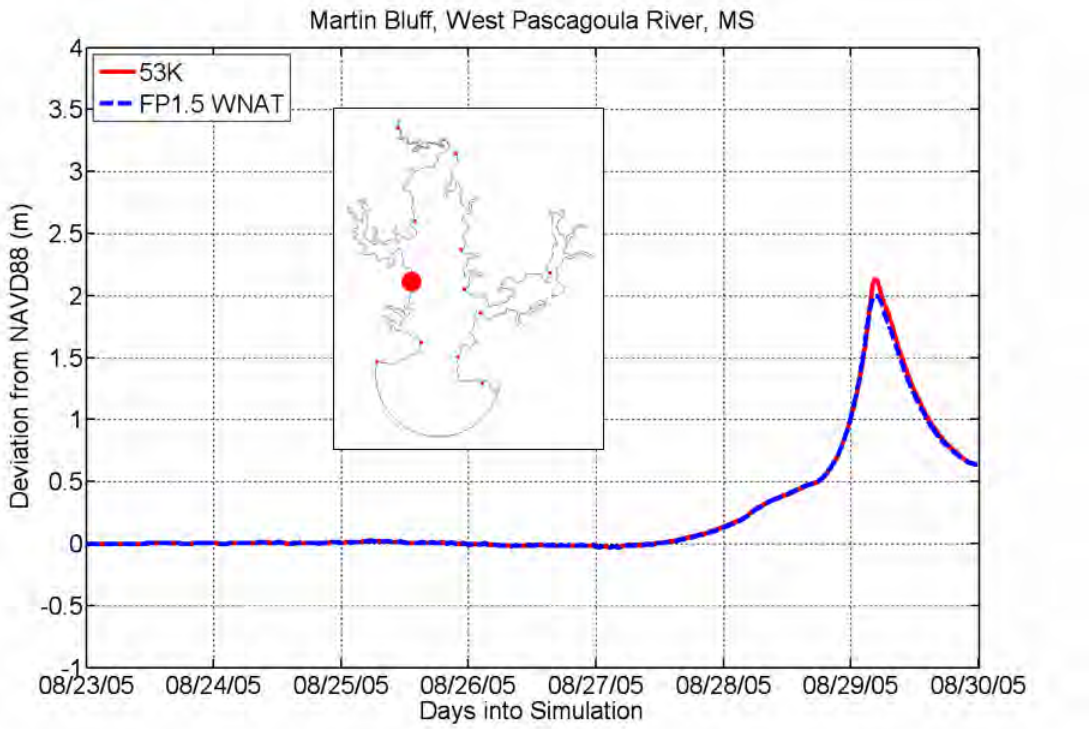

Figure 6.22 Model Storm Surge Hydrograph at Martin Bluff, West Pascagoula River, MS

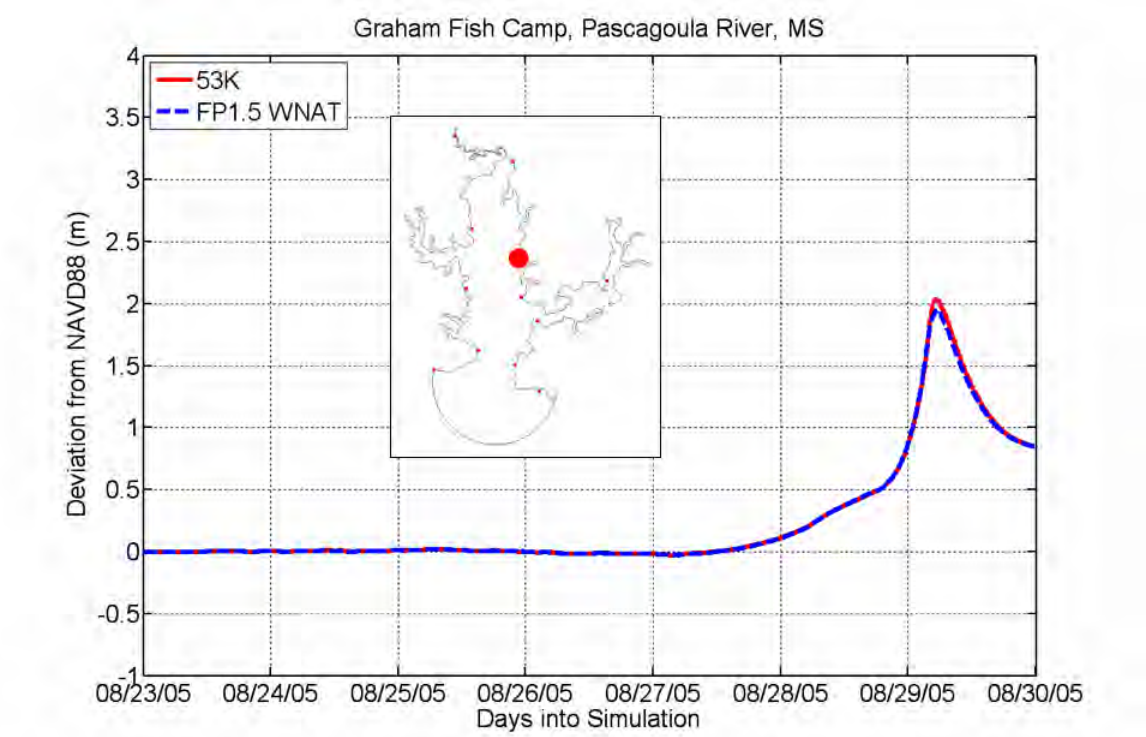

Figure 6.23 Model Storm Surge Hydrograph at Graham Fish Camp, Pascagoula River, MS

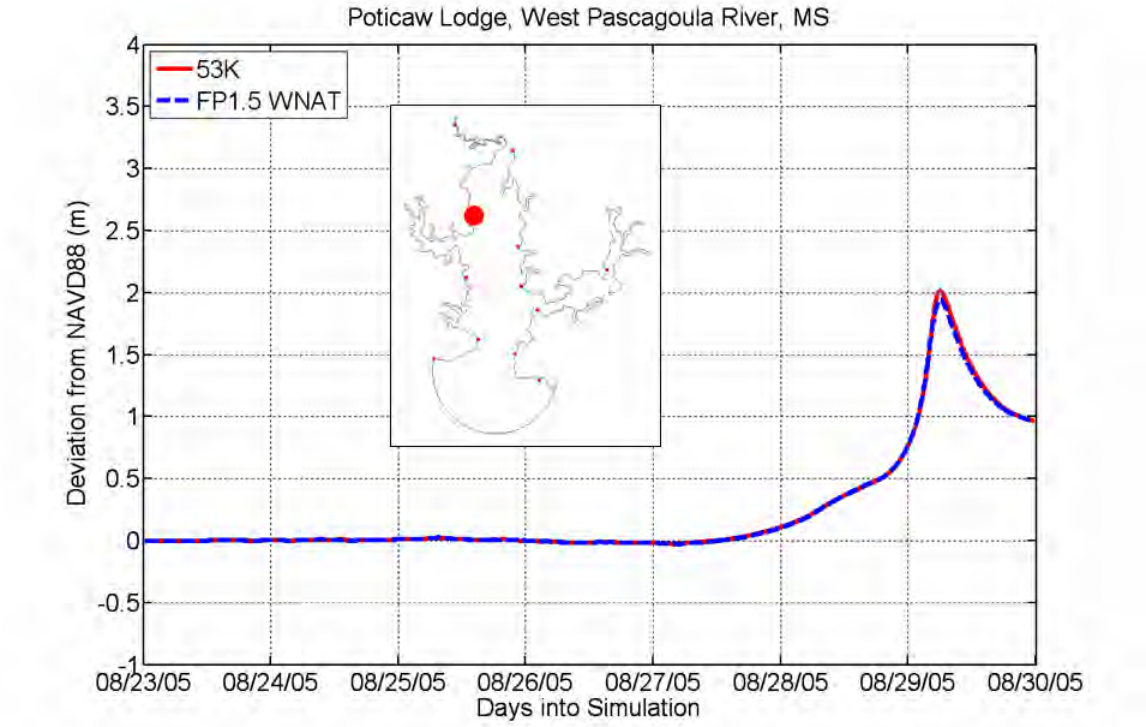

Figure 6.24 Model Storm Surge Hydrograph at Poticaw Lodge, West Pascagoula River, MS

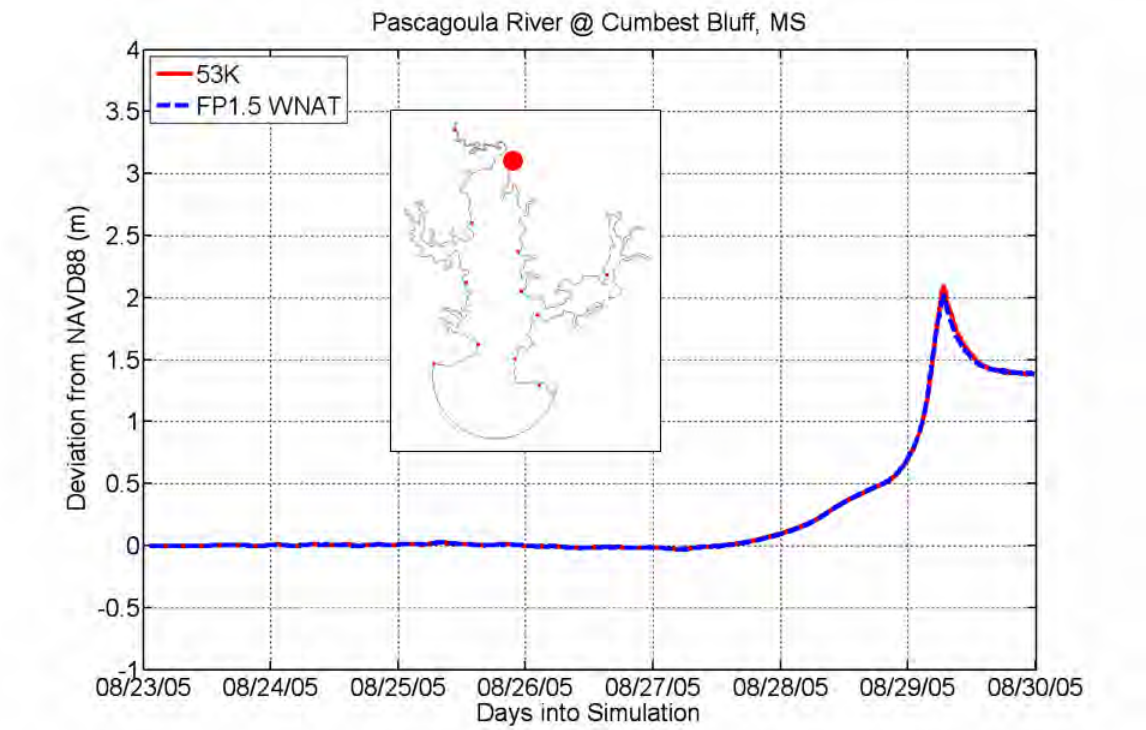

Figure 6.25 Model Storm Surge Hydrograph at Pascagoula River @ Cumbest Bluff, MS

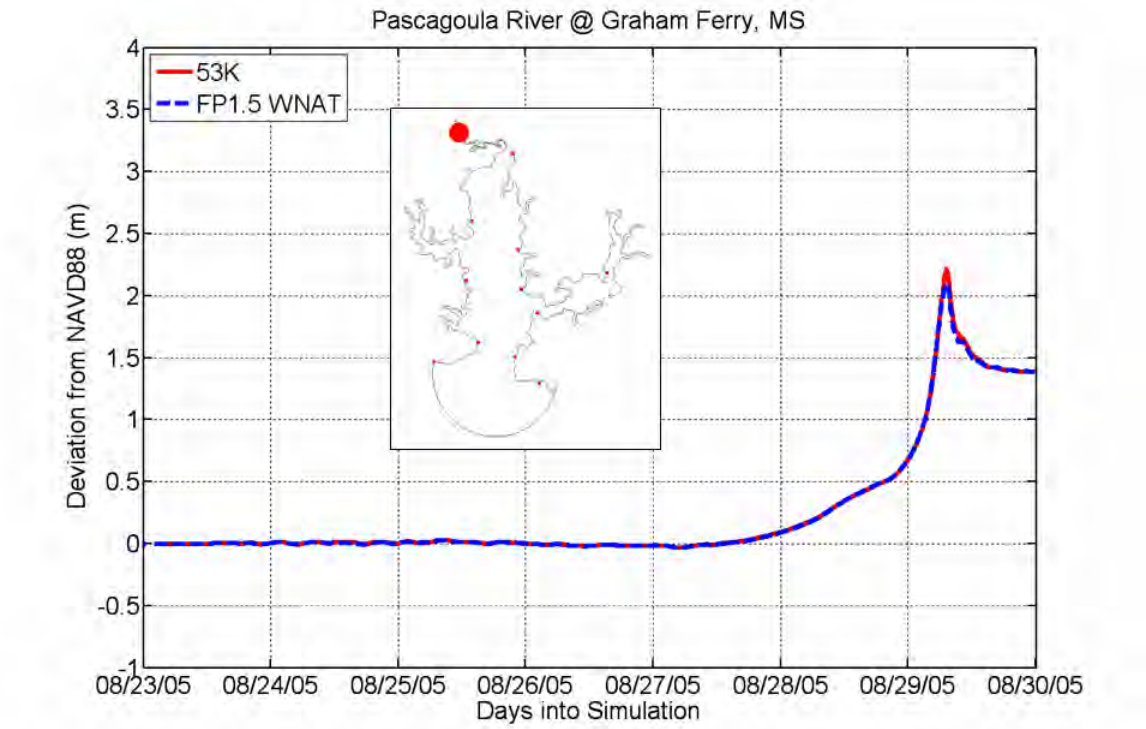

Figure 6.26 Model Storm Surge Hydrograph at Graham Ferry, Ascagoula River, MS

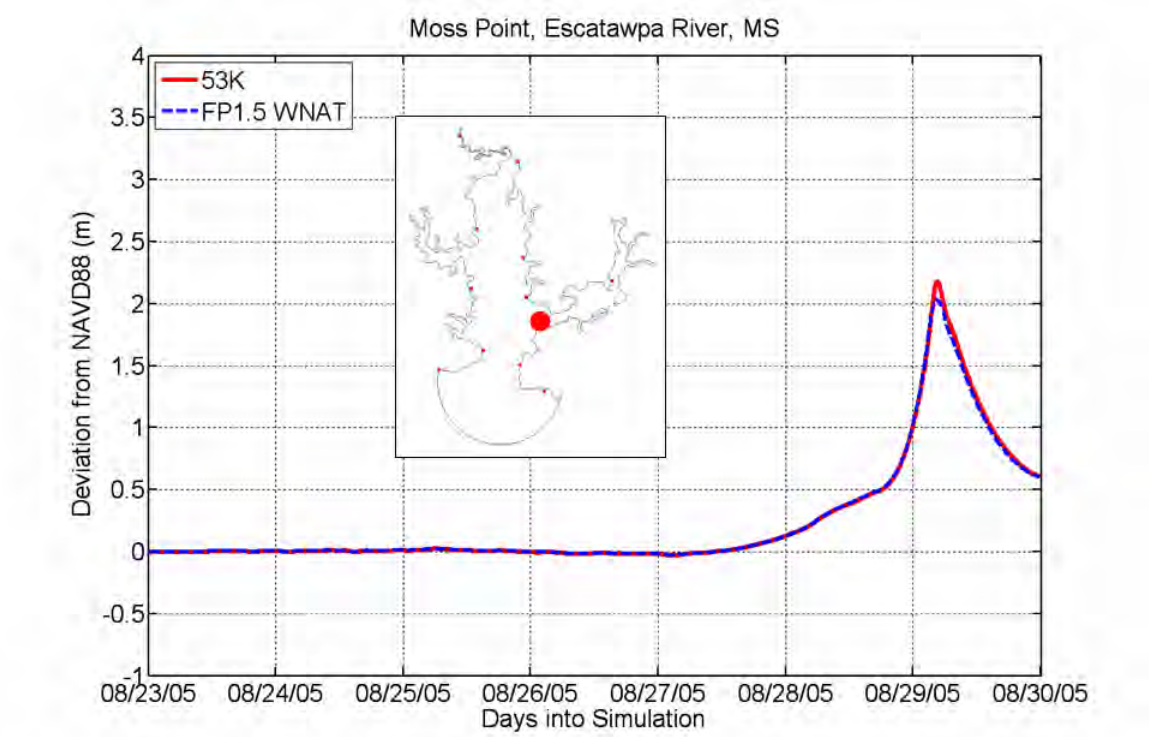

Figure 6.27 Model Storm Surge Hydrograph at Moss Point, Escatawpa River, MS

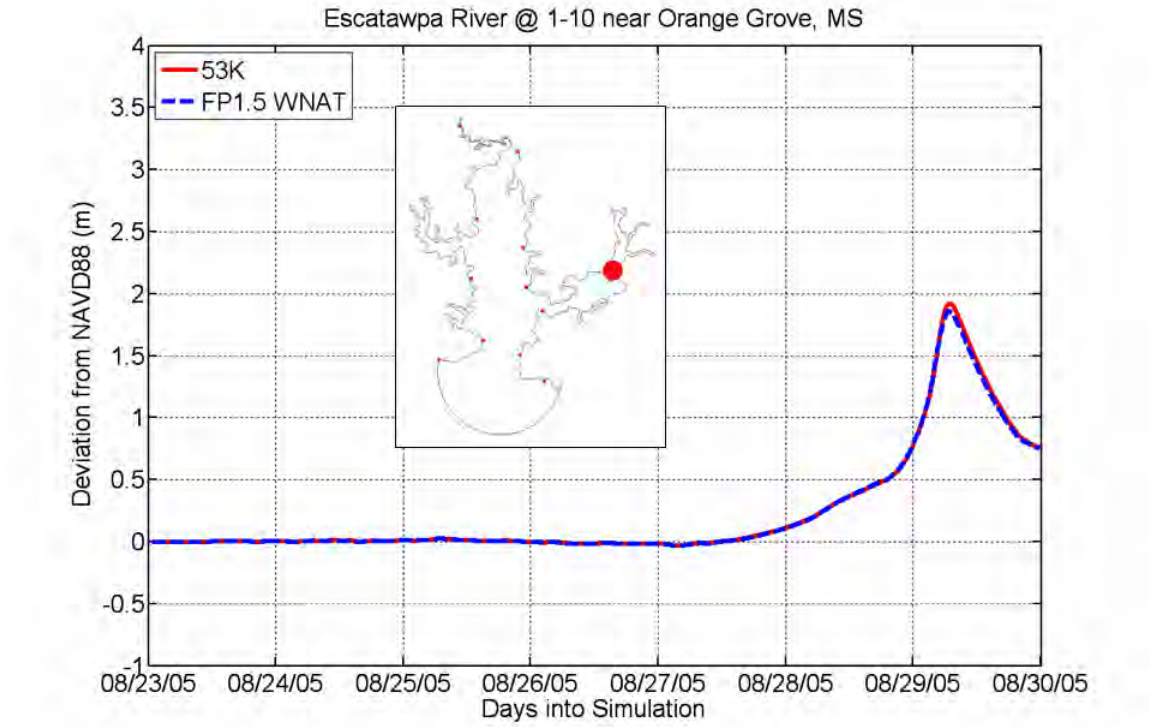

Figure 6.28 Model Storm Surge Hydrograph at Pascagoula River @ Mile 1 @ Pascagoula, MS

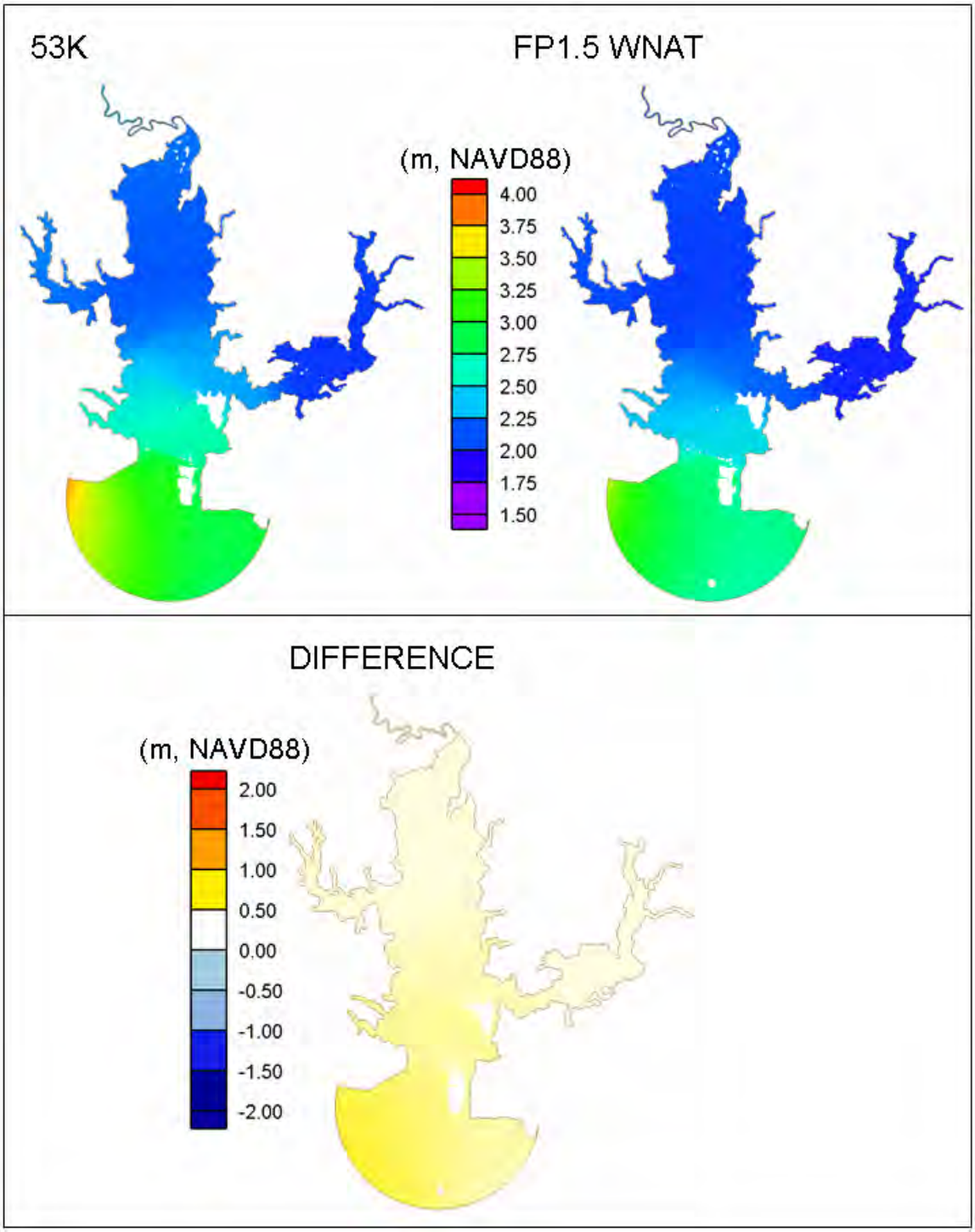

Figure 6.29 Maximum Envelop of Water (Top left) FP1.5_INLET model forced by storm surge hydrograph obtained from 53K mesh domain; (Top right) FP1.5_INLET model forced by storm surge hydrograph obtained from 53K mesh domain; (Bottom) Difference of two models

6.2.3 Inlet-based Model with Storm Surge Hydrograph and Meteorological Forcings (Experiments 7)

In order to examine local meteorological effects toward water surface elevations in the Pascagoula River, Experiment 7 applies winds and pressures over the inlet-based floodplain model (FP1.5_INLET). Also included in Experiment 7, the open-ocean boundary is forced by a storm surge hydrograph generated from the large-domain modeling approach (FP1.5_WNAT mesh application) so that the model results can be compared to those generated in the previous experiment forced by storm surge hydrograph only (see Experiment 6).

Model output from the FP1.5_INLET mesh applications of Experiments 6 and 7 is provided for ten stations (see Figure 6.30 to Figure 6.39). The FP1.5_INLET model output (for when it is forced by a hydrograph [calculated by the FP1.5_WNAT mesh] only) is represented by a blue solid line and the FP1.5_INLET model output (for when it is forced by a hydrograph [calculated by the FP1.5_WNAT mesh] and local winds and pressures) is represented by a green dashed line. The effect of local winds and pressures becomes apparent in different ways. For example, at the two most upstream locations in the Pascagoula River (see Figure 6.36 and Figure 6.37), the storm surge peak is greatly increased for when the local winds and pressures are considered. Considering the orientation of the estuary and the track of the storm, local winds and pressures appear to have accumulated water significantly in the upstream portions of the Pascagoula River. Also apparent at the upstream locations (e.g., see Figure 6.38 and Figure 6.39) is the setup and setdown of the water prior to the storm surge peak. The pressure effect causes a

minimal setup prior to the storm surge peak; the setdown effect is more prominent and can be explained by the wind direction (blowing water to the south) as the storm just begins to enter the model domain. The significant gradient in the rising limb of the storm surge hydrograph can be explained in the reversal of wind direction to blow water (over a sustained duration) to the north. Maximum envelopes of water (i.e. maximum height of the storm surge) are calculated for the FP1.5_INLET mesh applications (without and with local winds and pressures) (Figure 6.40). For when local winds and pressures are considered, significant amounts of water are allowed to accumulate in the upstream portions of the Pascagoula River. A difference between the two maximum envelopes of water is calculated to highlight regions where the solutions differ. In fact, in the upstream portions of the Pascagoula River, the local wind and pressure forcing attributes to nearly a 2-m rise in water levels.

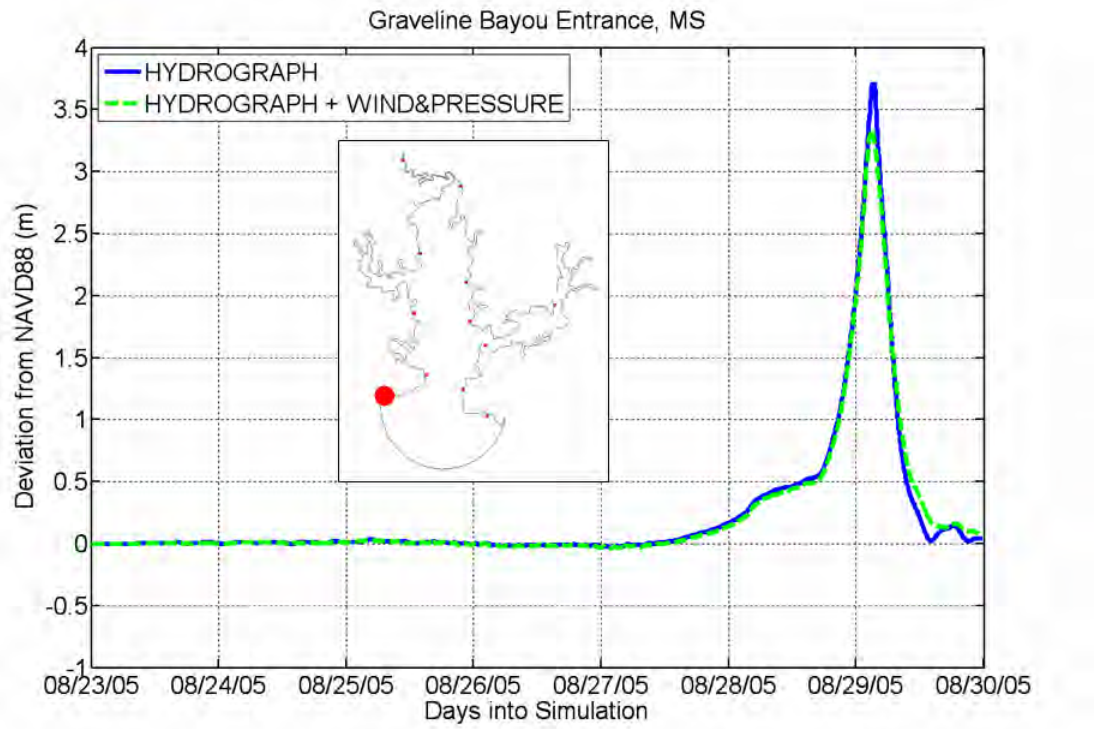

Figure 6.30 Model Storm Surge Hydrograph at Graveline Bayou Entrance, MS

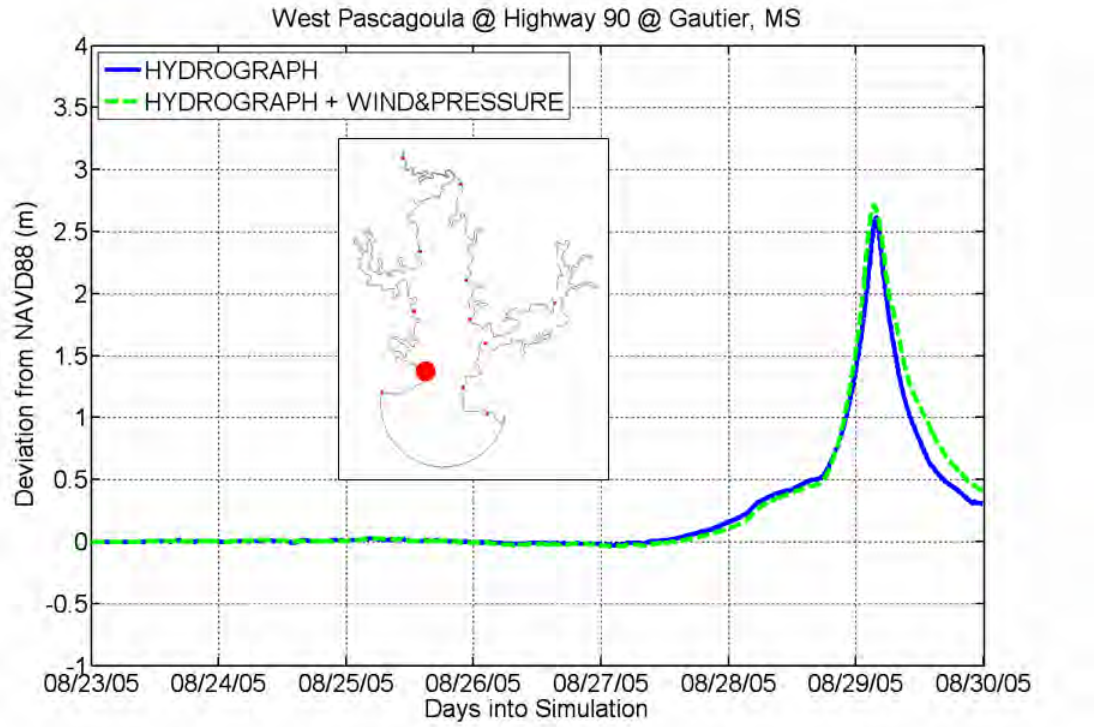

Figure 6.31 Model Storm Surge Hydrograph at West Pascagoula @ Highway 90 @ Gautier, MS

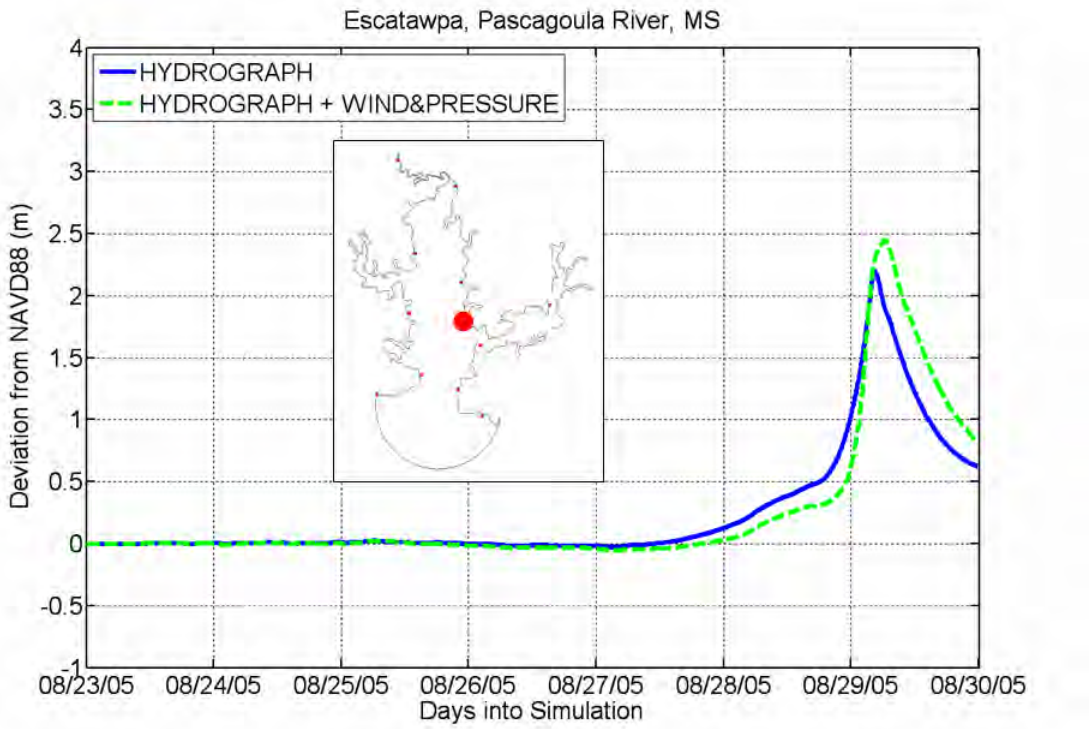

Figure 6.32 Model Storm Surge Hydrograph at Escatawpa, Pascagoula River, MS

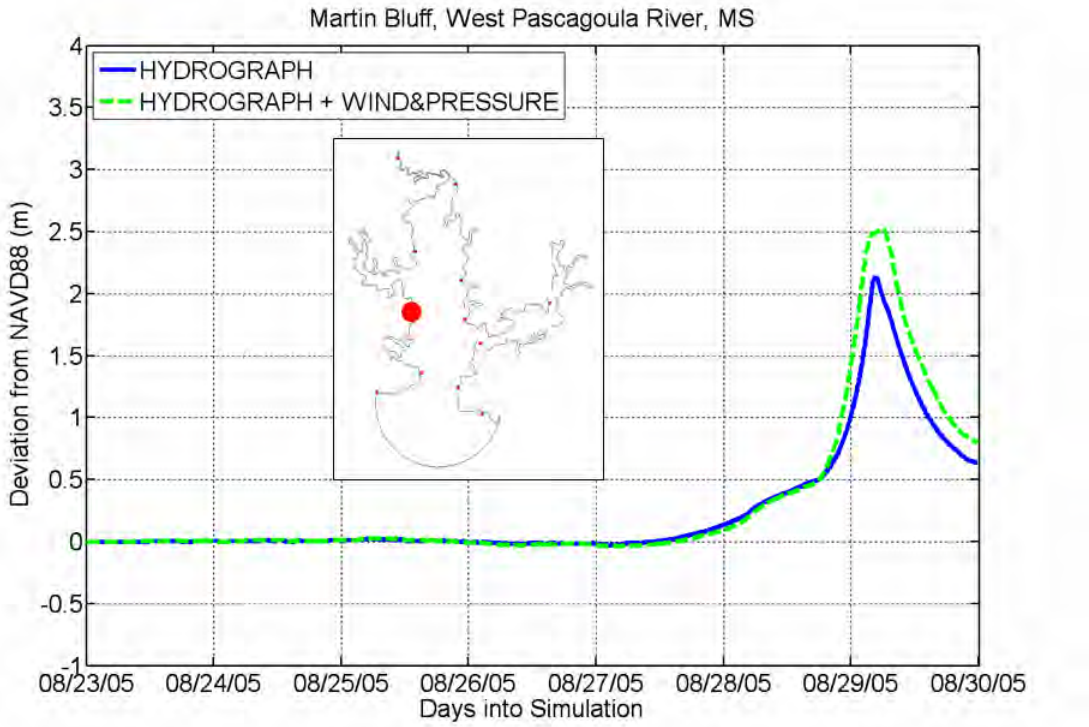

Figure 6.33 Model Storm Surge Hydrograph at Martin Bluff, West Pascagoula River, MS

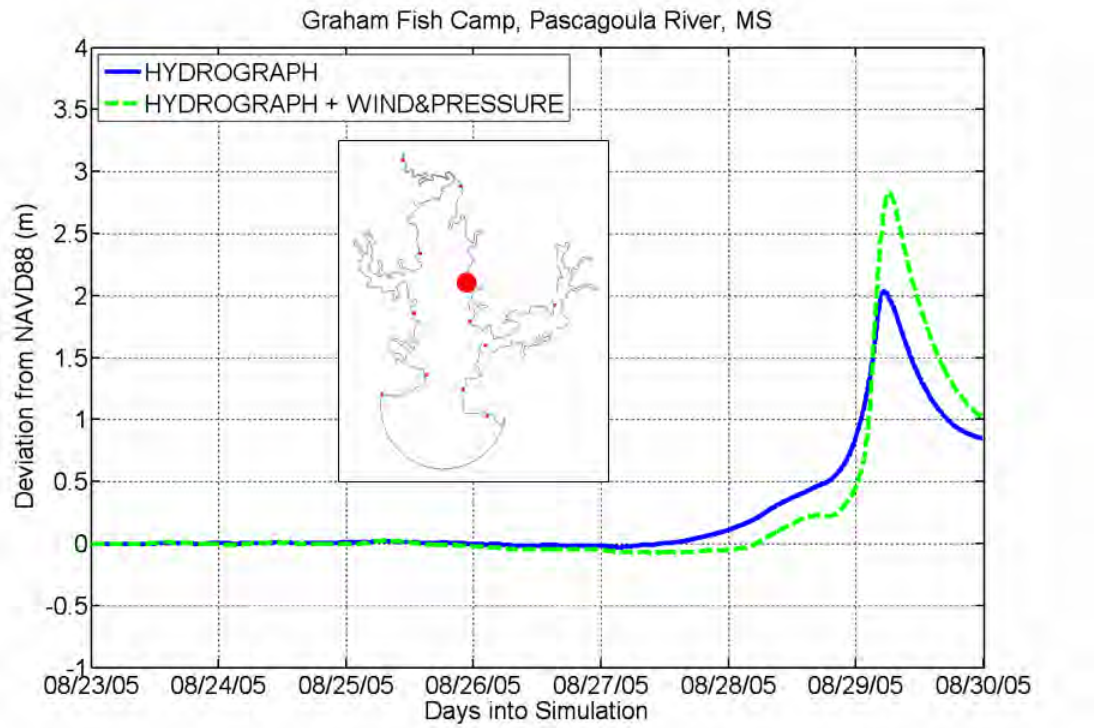

Figure 6.34 Model Storm Surge Hydrograph at Graham Fish Camp, Pascagoula River, MS

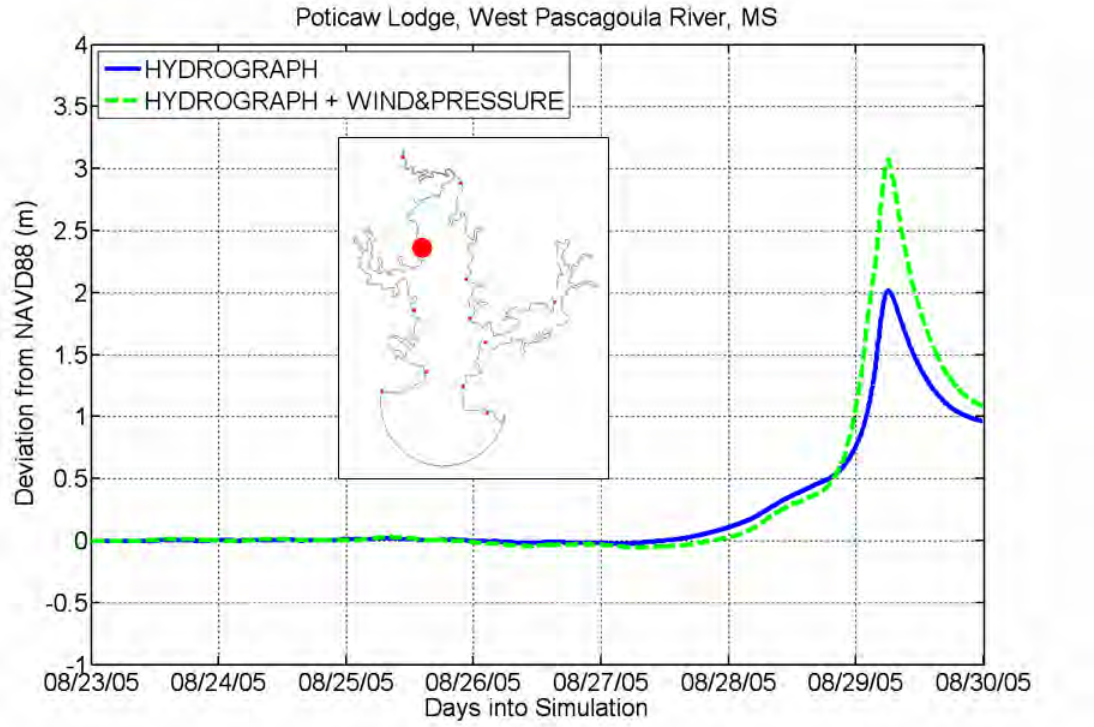

Figure 6.35 Model Storm Surge Hydrograph at Poticaw Lodge, West Pascagoula River, MS

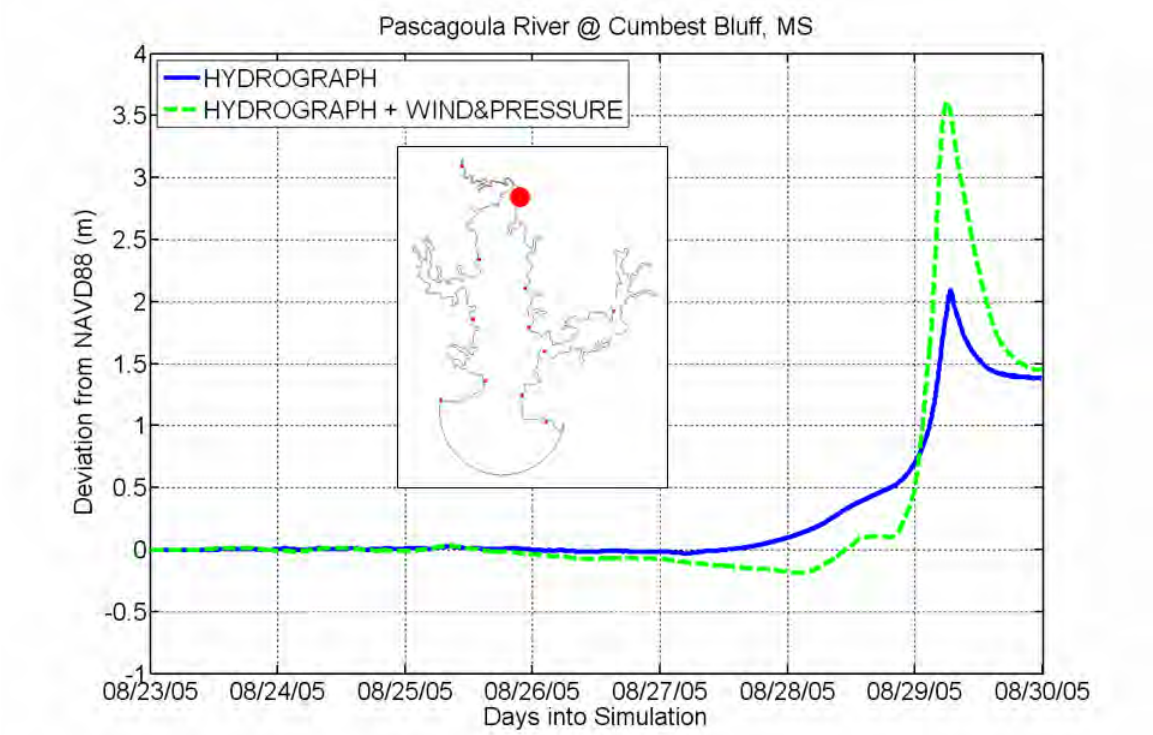

Figure 6.36 Model Storm Surge Hydrograph at Pascagoula River @ Cumbest Bluff, MS

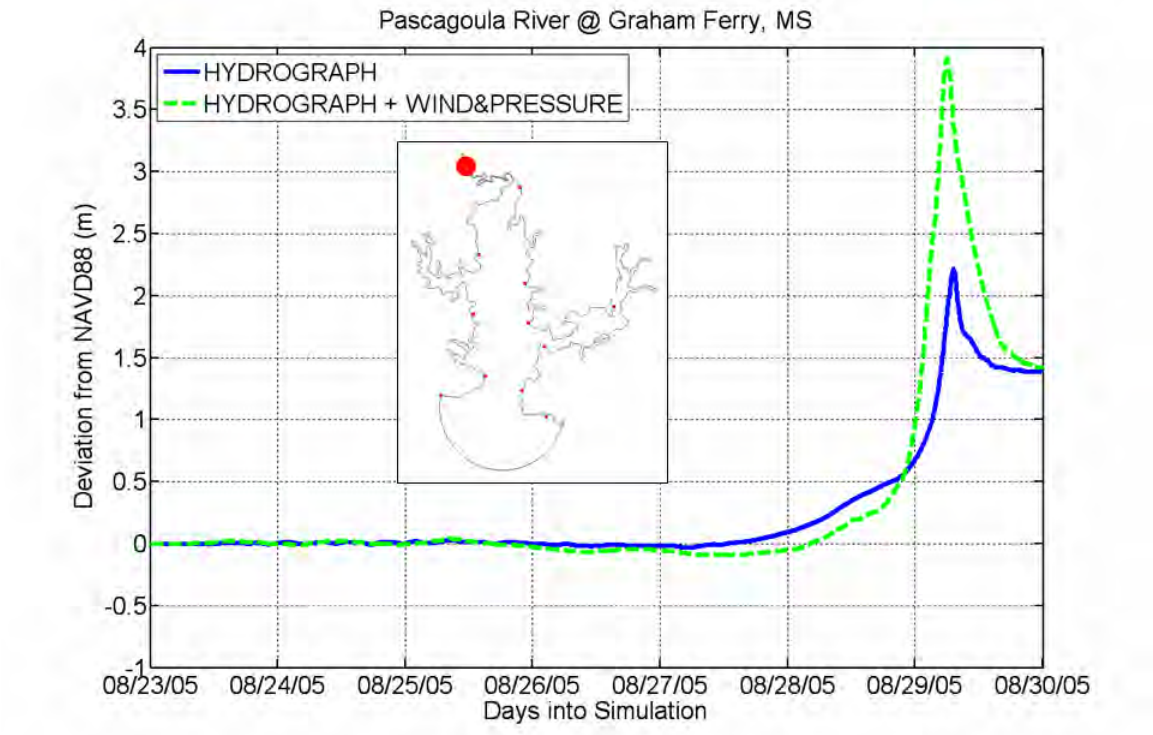

Figure 6.37 Model Storm Surge Hydrograph at Pascagoula River @ Graham Ferry, MS

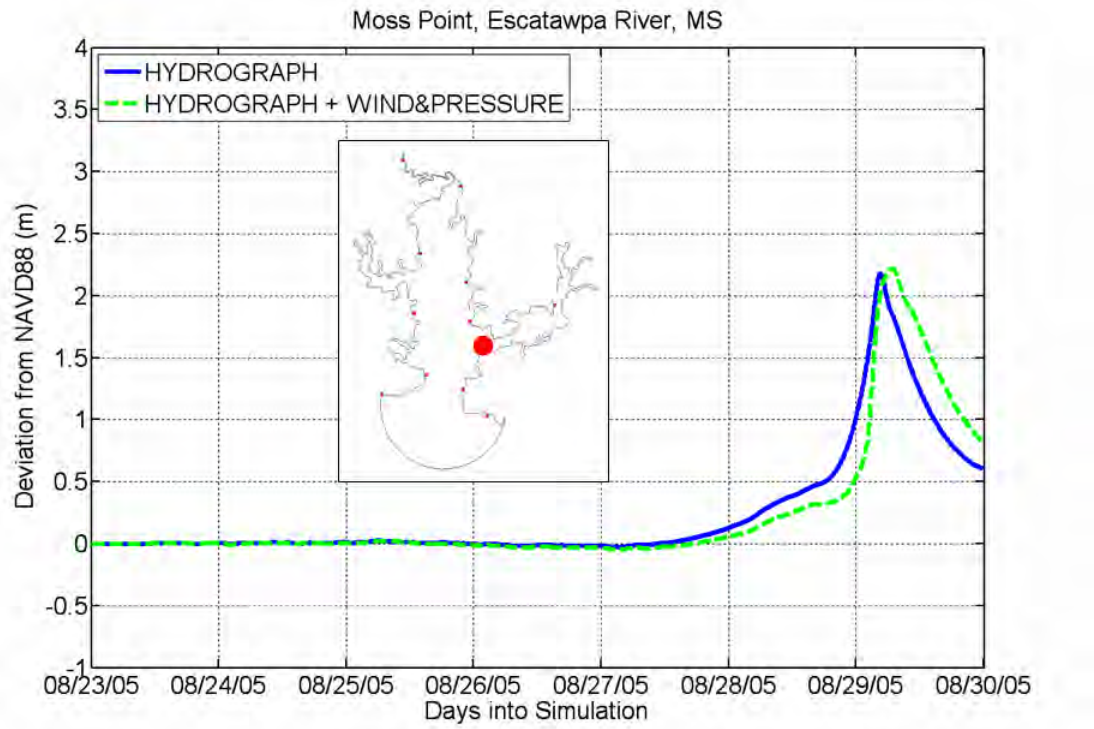

Figure 6.38 Model Storm Surge Hydrograph at Moss Point, Escatawpa River, MS

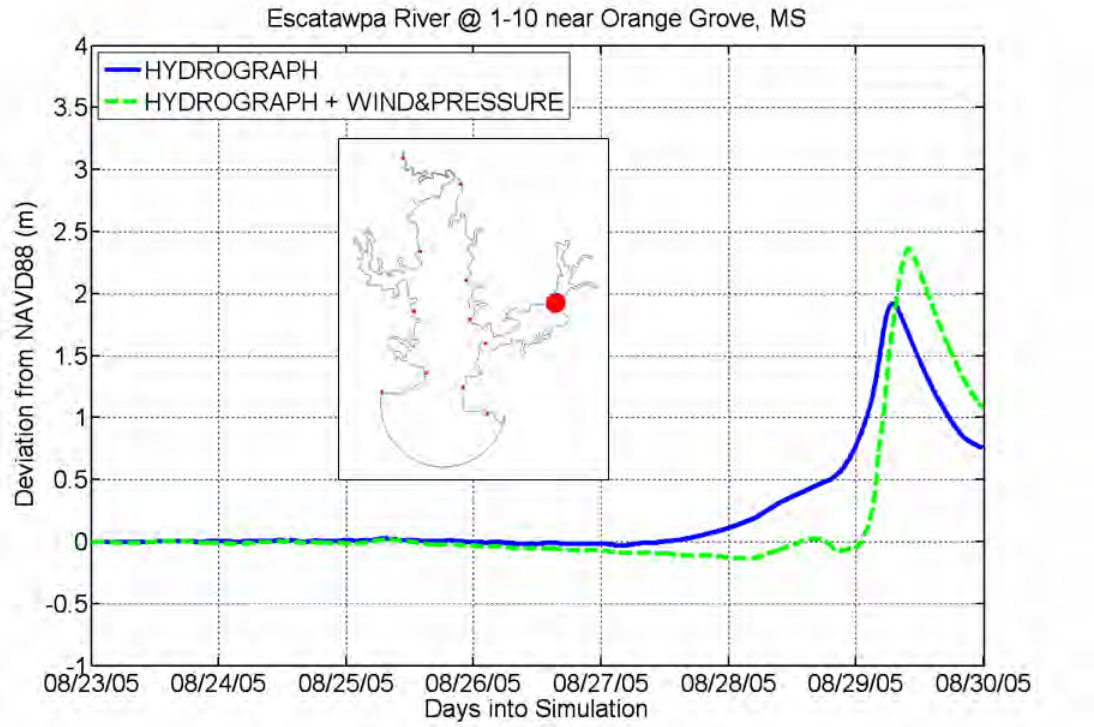

Figure 6.39 Model Storm Surge Hydrograph at Escatawpa River @ 1-10 near Orange Grove, MS

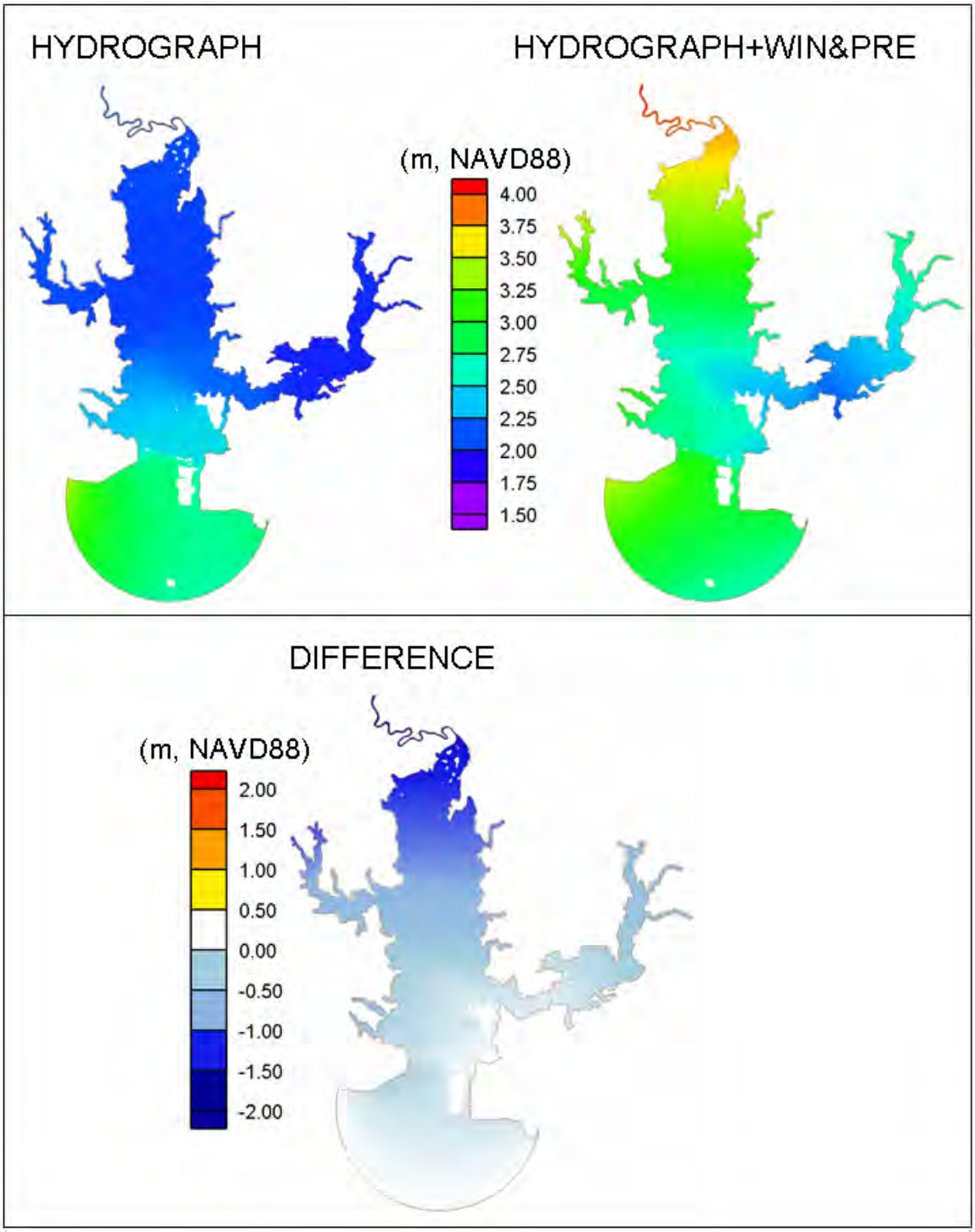

Figure 6.40 Maximum Envelop of Water (Top left) FP1.5_INLET model forced by storm surge hydrograph obtained from FP1.5_WNAT mesh domain; (Top right) FP1.5_INLET model forced by storm surge hydrograph obtained from FP1.5_WNAT mesh domain plus wind and pressure; (Bottom) Difference of two models

6.2.4 Comparison of WNAT-based Model (Experiment 4) and Inlet-based Model (Experiment 7)

In order to verify application of the inlet-based model with a combined forcing of a storm surge hydrograph and meteorological inputs, the inlet-based model output is compared to the that produced by the WNAT-based model, which is considered to be the most comprehensive mesh description. Model output from the FP1.5_INLET mesh application (Experiment 7) is compared to model output from the FP1.5_WNAT mesh application (Experiment 4) for ten stations (see Figure 6.41 to Figure 6.50). The FP1.5_WNAT model output (for when it is forced by winds and pressures) is represented by a red solid line and the FP1.5_INLET model output (for when it is forced by a hydrograph [calculated by the FP1.5_WNAT mesh] and local winds and pressures) is represented by a green dashed line. The similarity in the model results is expected and justifies application of the localized domain through use of the open-ocean hydrograph (generated by the large-scale model domain).

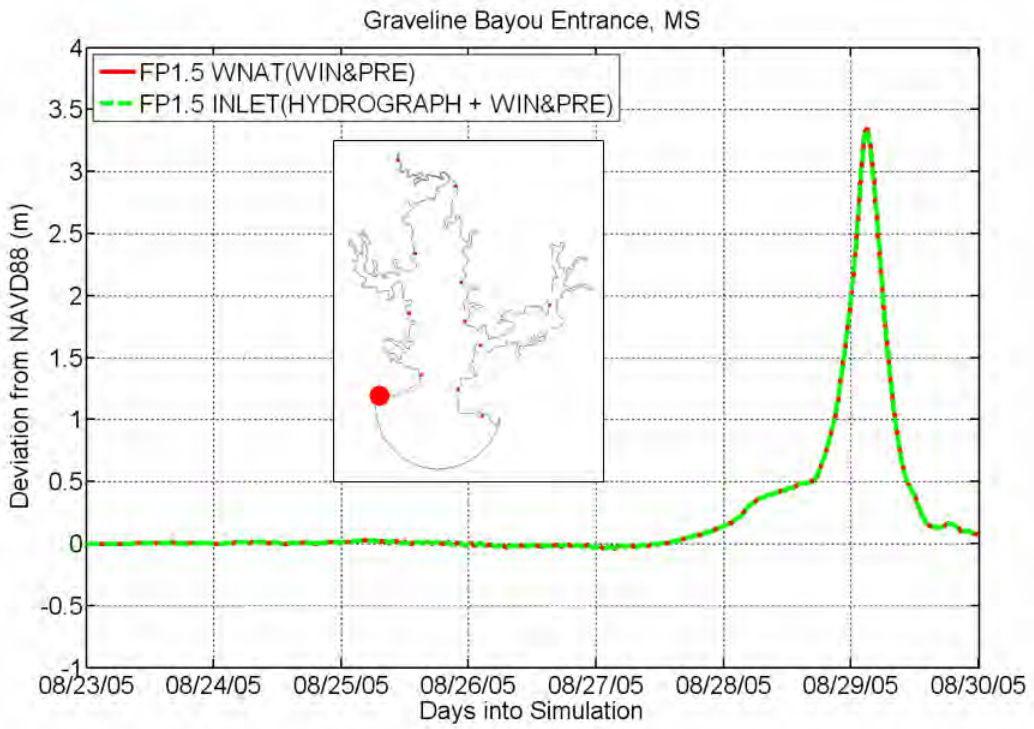

Figure 6.41 Model Storm Surge Hydrograph at Graveline Bayou Entrance, MS

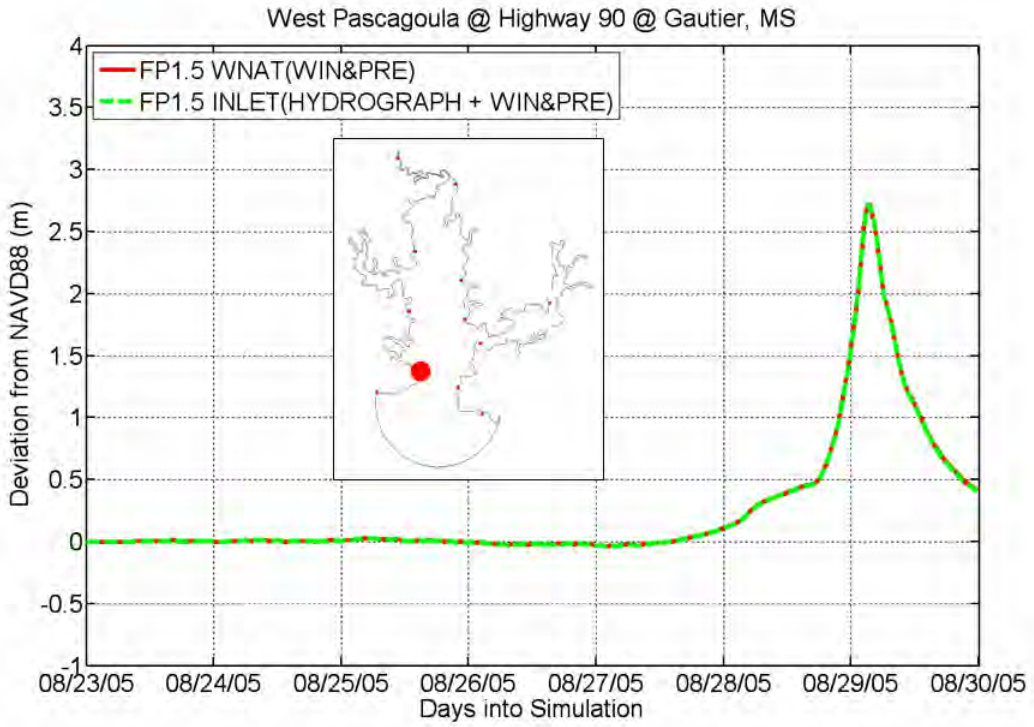

Figure 6.42 Model Storm Surge Hydrograph at West Pascagoula @ Highway 90 @ Gautier, MS

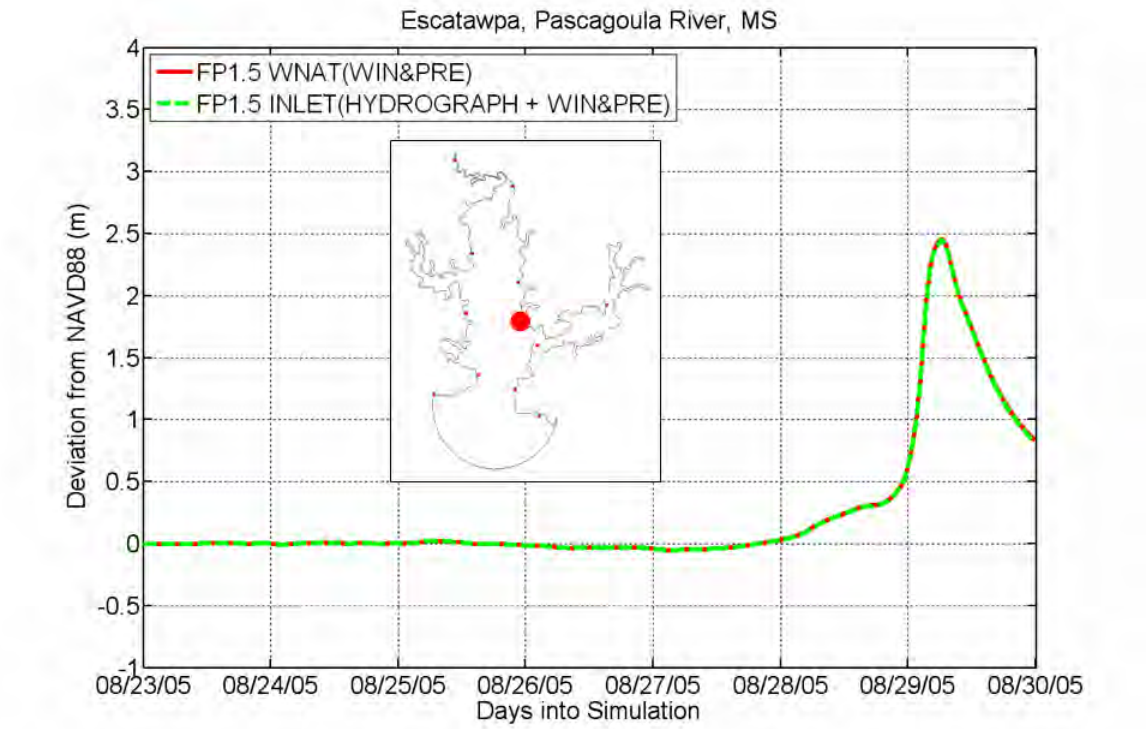

Figure 6.43 Model Storm Surge Hydrograph at Escatawpa, Pascagoula River, MS

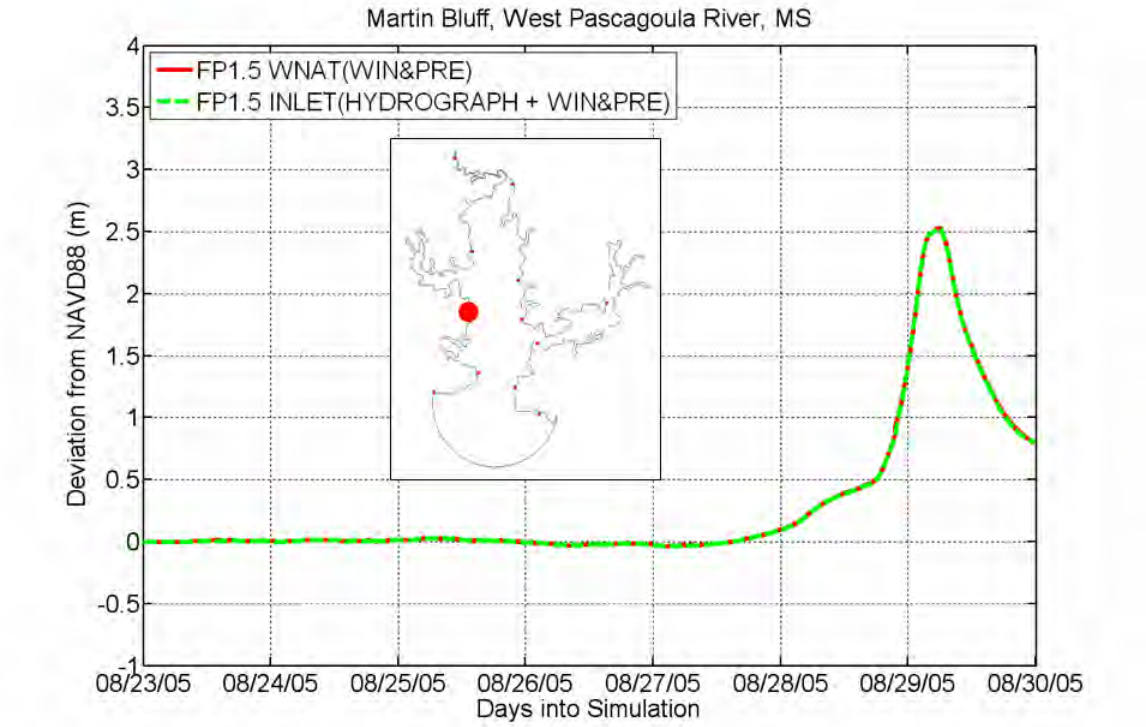

Figure 6.44 Model Storm Surge Hydrograph at Martin Bluff, West Pascagoula River, MS

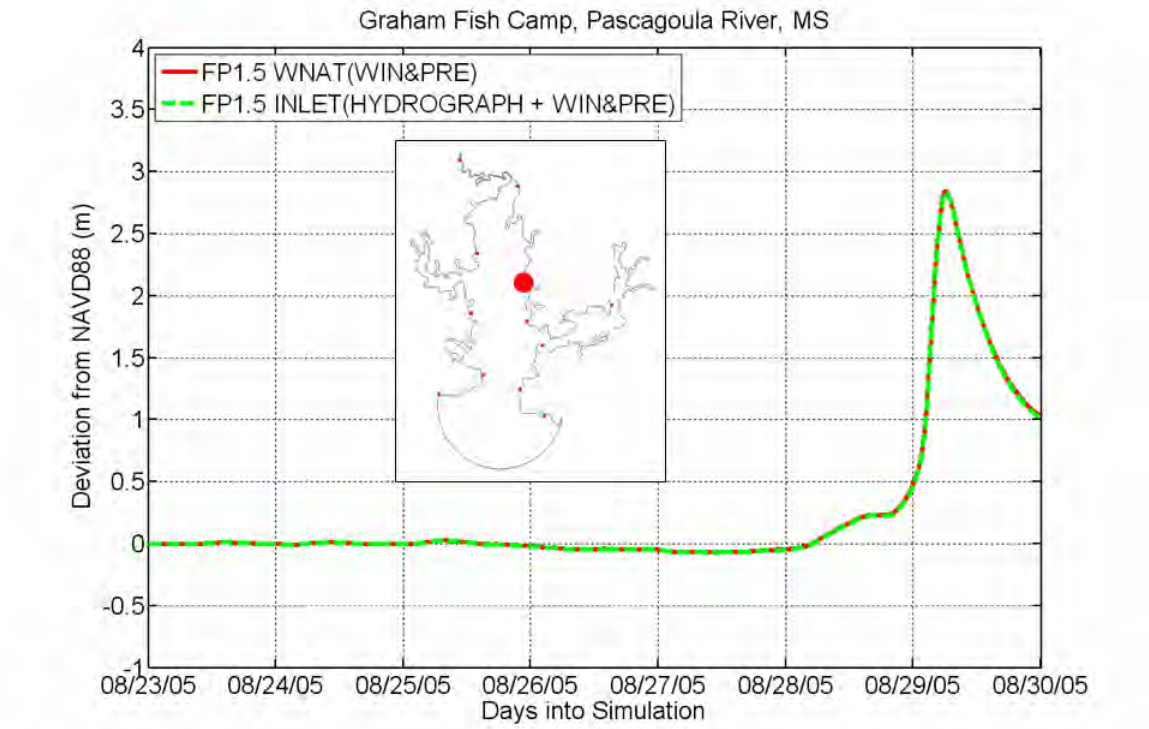

Figure 6.45 Model Storm Surge Hydrograph at Graham Fish Camp, Pascagoula River, MS

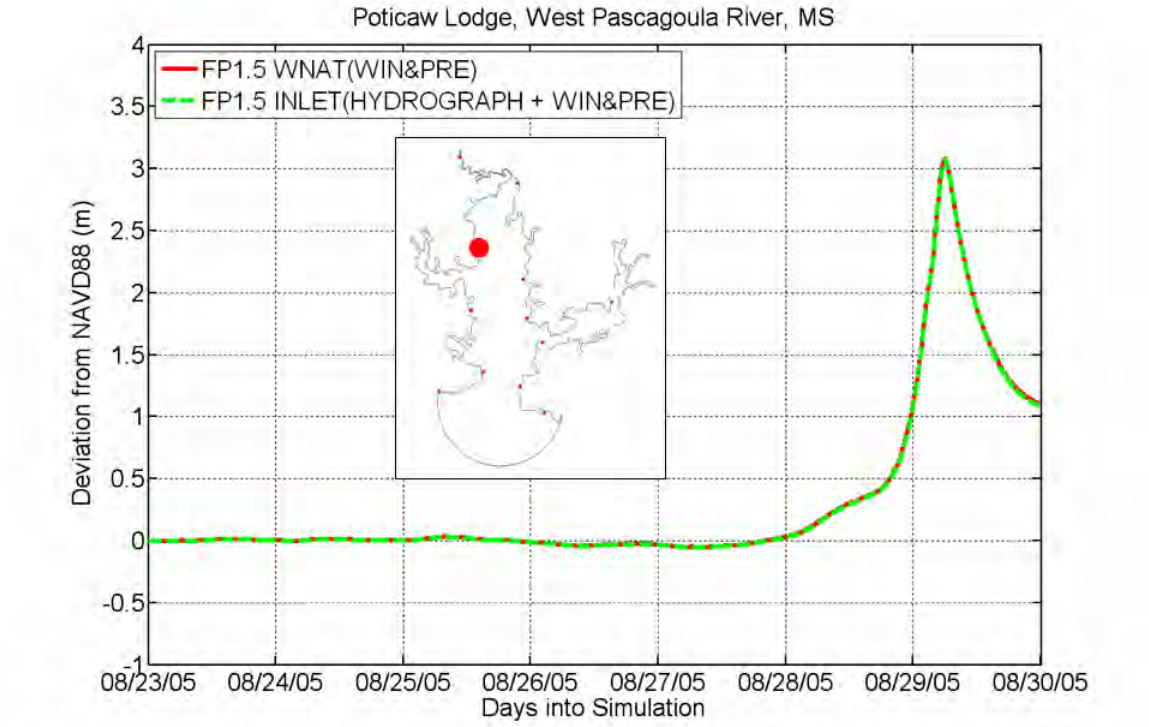

Figure 6.46 Model Storm Surge Hydrograph at Poticaw Lodge, West Pascagoula River, MS

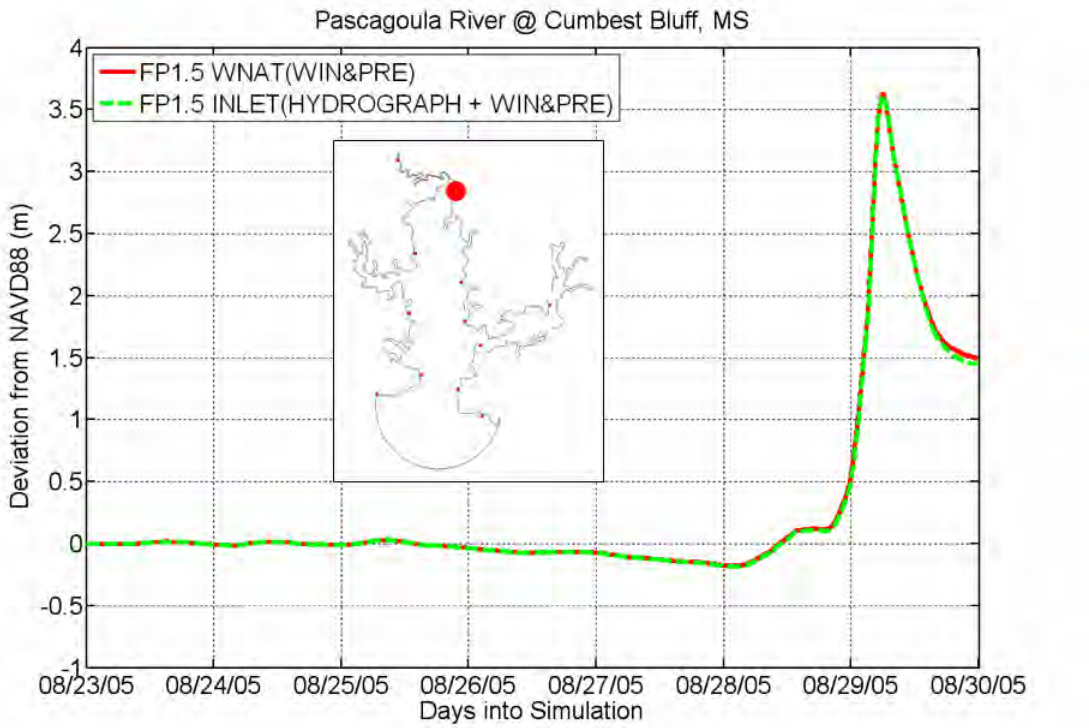

Figure 6.47 Model Storm Surge Hydrograph at Pascagoula River @ Cumbest Bluff, MS

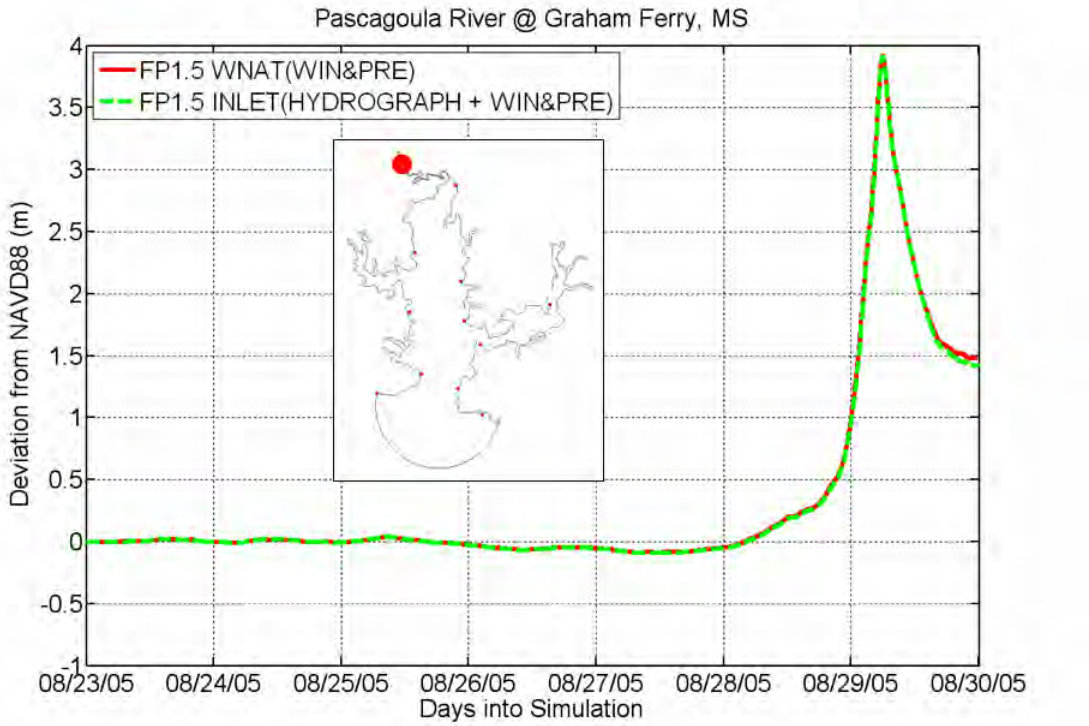

Figure 6.48 Model Storm Surge Hydrograph at Pascagoula River @ Graham Ferry, MS

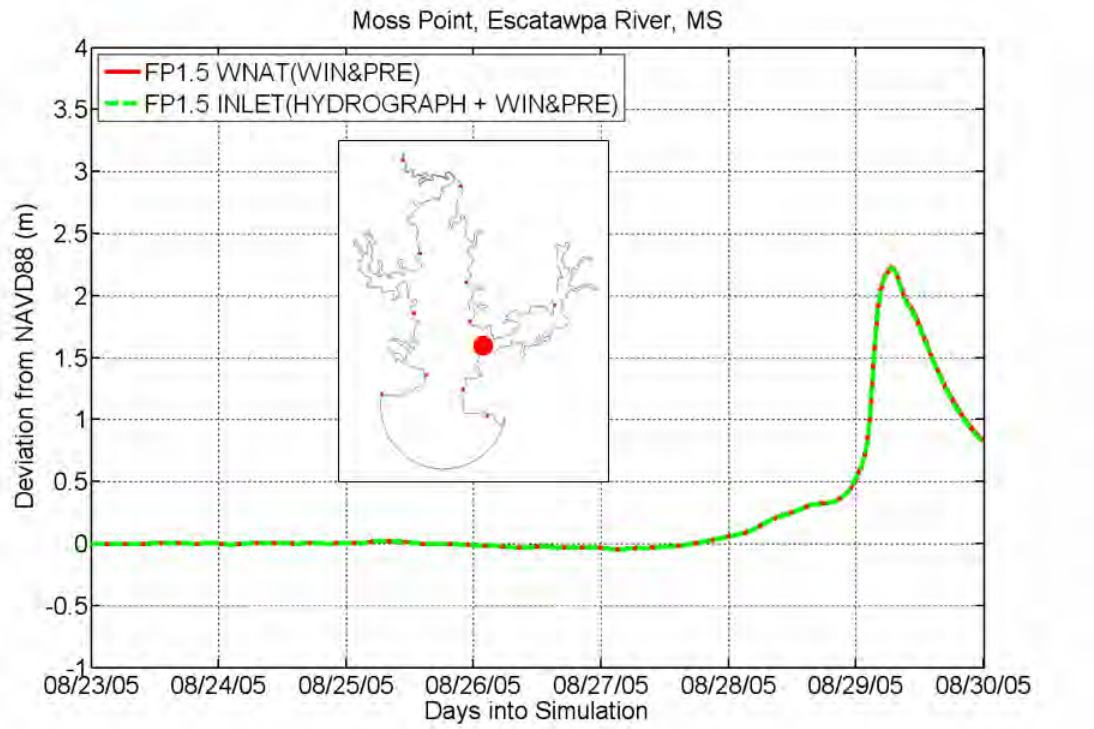

Figure 6.49 Model Storm Surge Hydrograph at Moss Point, Escatawpa River, MS

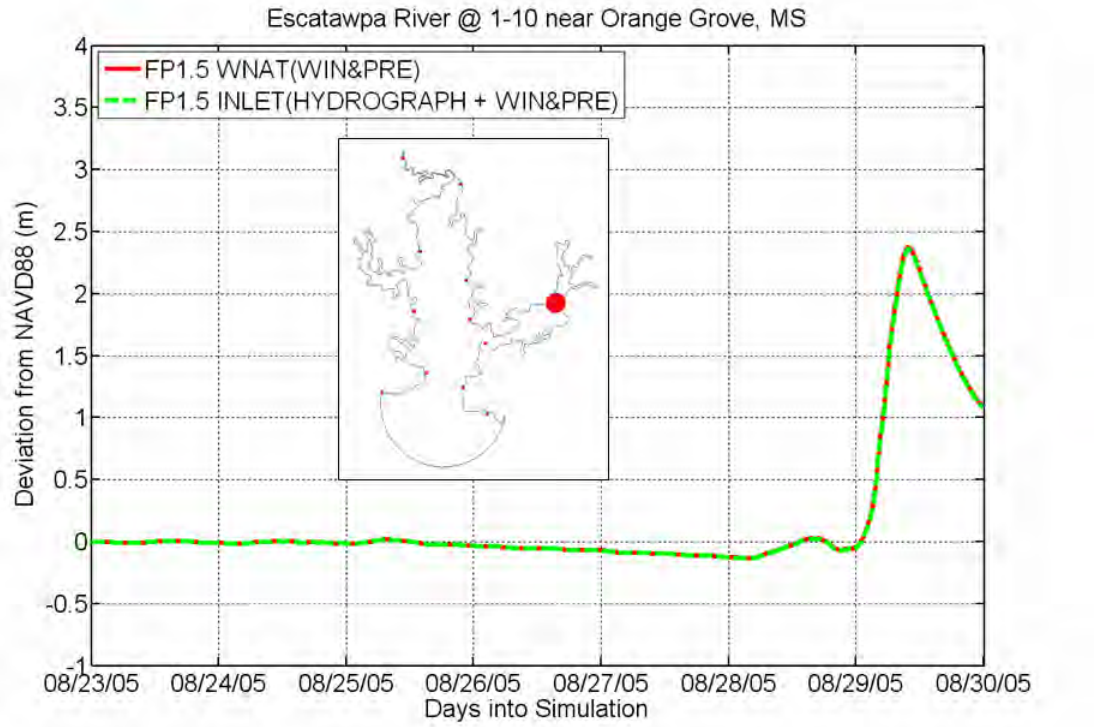

Figure 6.50 Model Storm Surge Hydrograph at Escatawpa River @ 1-10 near Orange Grove, MS

6.2.5 Historical Data Verification

Lastly, we compare the model output to historical data (Figure 6.51 to Figure 6.55). Recall that our interest is towards understanding the forcing mechanisms for storm surge elevations in the Pascagoula River; it is not being claimed that the numerical model presented herein should be used for a hindcast of Hurricane Katrina storm surge levels. In fact, we regard it as necessary to examine the boundary forcings and model implementations prior to any calibration to historical data. Otherwise, important physics of the system would be folded in the model calibration process and would go undetected.

Historical stage data are provided by the LMRFC for four gauge stations located within the Pascagoula region. The historical data are represented by the black solid line and the FP1.5_INLET model output (for when it is forced by a hydrograph produced by the FP1.5_WNAT mesh and local winds and pressures) is represented by the green dashed line. It is noted that the historical data relates to the full response of the water level due to astronomic tides, freshwater river inflow, wind-driven waves, etc., while the model output corresponds to storm surge only.

Overall, the model captures the time of peak and the peak water level adequately. At the first station (Figure 6.51), Pascagoula, MS, the model result is dry except for during the storm surge peak. At the upstream stations (Cumbest Bluff and Escatawpa River), the historical data show that water remained in the system for some time after the peak storm surge (Figure 6.53 and Figure 6.55). Clearly, freshwater river inflows played a role in the recession of the storm surge; while the timing and level of the storm surge peak was well-

simulated by the numerical model, the recession of the storm surge is much quicker in the model response due to the absence of freshwater river inflows. The setup and setdown prior to the peak storm surge is also well-captured in the numerical model (Figure 6.55), providing further justification to the modeling approach employed herein.

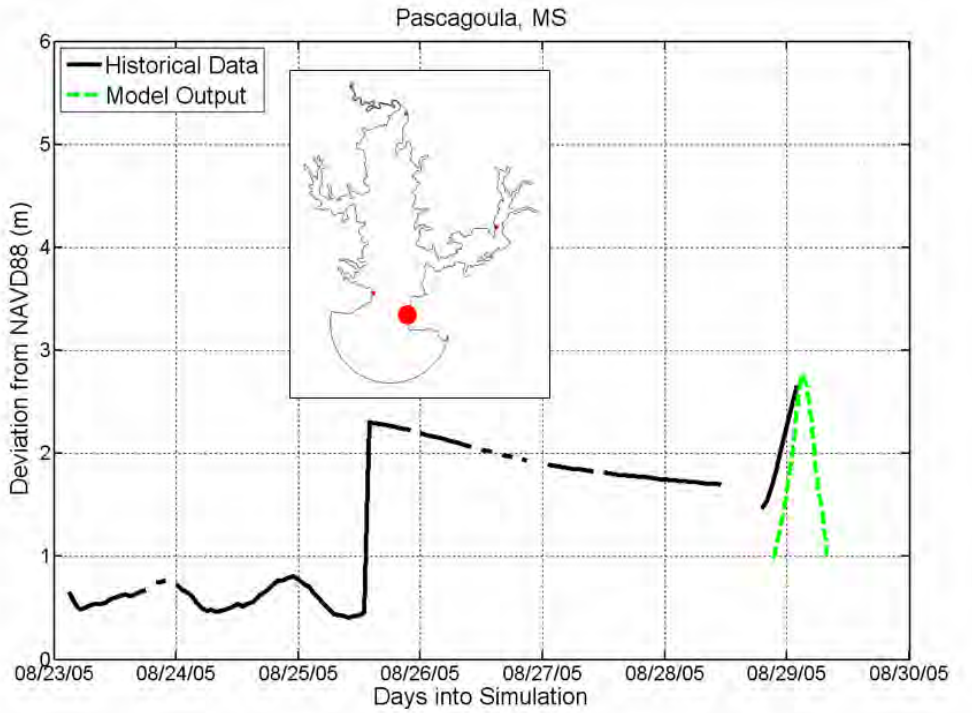

Figure 6.51 Historical Water Stage and Model Storm Surge Hydrograph Comparison at Pascagoula, MS

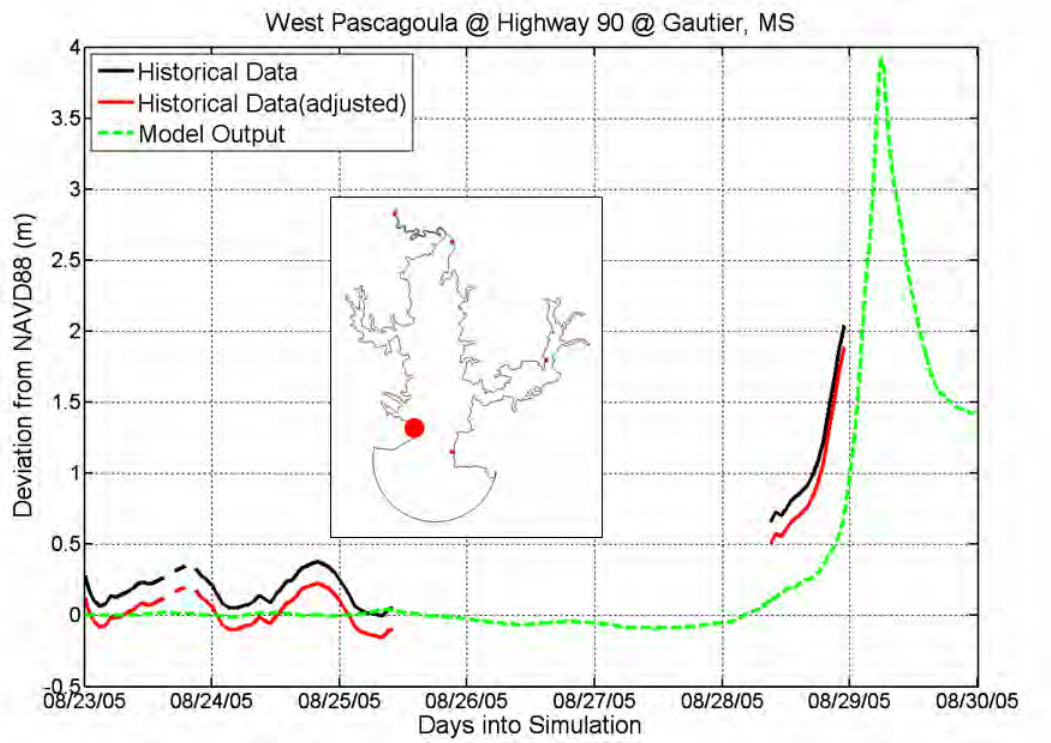

Figure 6.52 Historical Water Stage and Model Storm Surge Hydrograph Comparison at West Pascagoula @ Highway 90 @ Gautier, MS

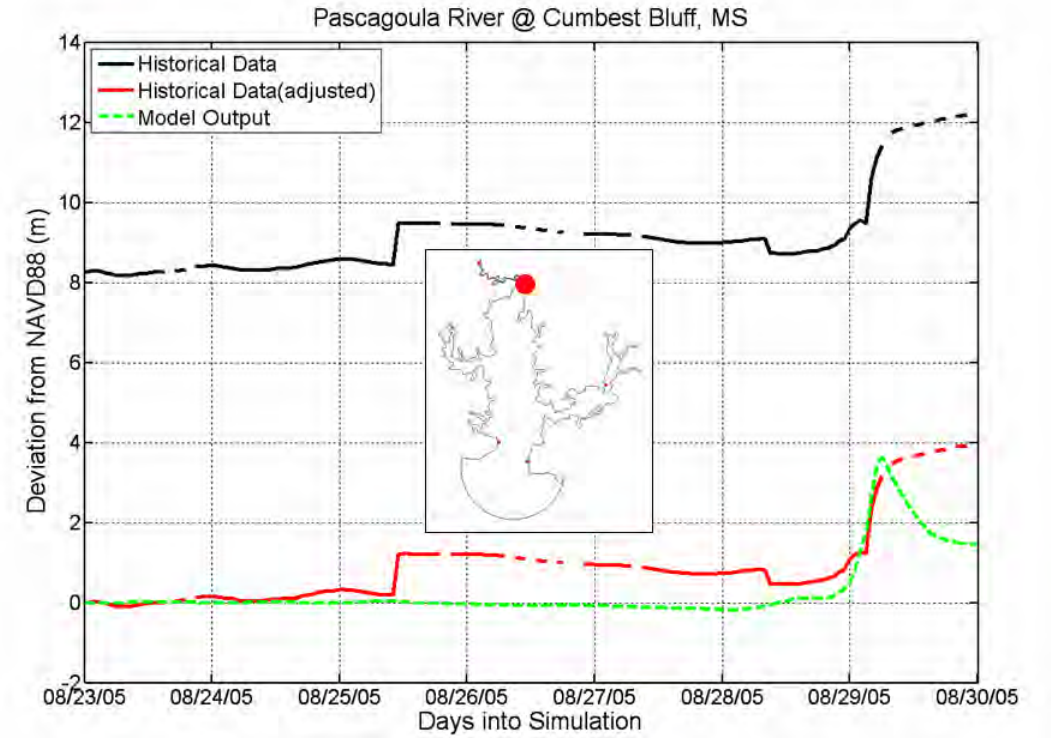

Figure 6.53 Historical Water Stage and Model Storm Surge Hydrograph Comparison at Pascagoula River @ Cumbest Bluff, MS

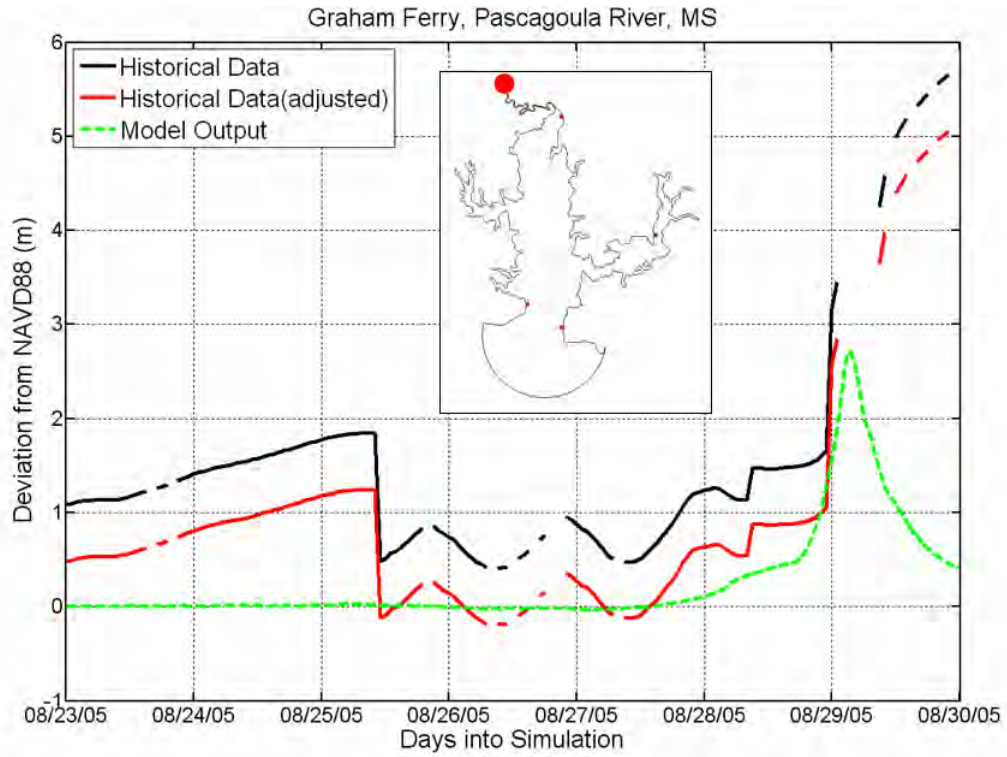

Figure 6.54 Historical Water Stage and Model Storm Surge Hydrograph Comparison at Graham Ferry, Pascagoula River, MS

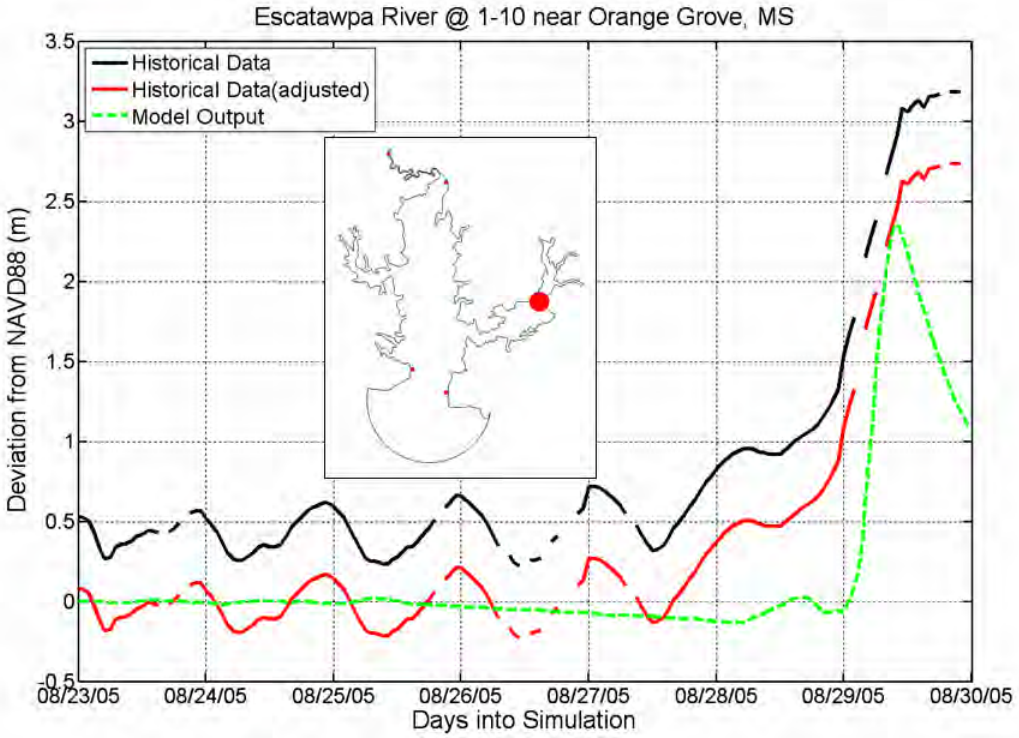

Figure 6.55 Historical Water Stage and Model Storm Surge Hydrograph Comparison at Escatawpa River @ 1-10 near Orange Grove, MS

CHAPTER 7. CONCLUSIONS AND FUTURE WORK

Chapter 7 presents the conclusions that resulted from conducting this research along with future efforts associated with the work. One objective of this study was to develop a floodplain DEM for the Pascagoula River in order to develop a numerical model that will allow for an understanding of the storm surge dynamics within the Pascagoula River. First, we developed a 1.5-m contour floodplain model domain which covers the marsh areas concerning the Lower Pascagoula and Escatawpa Rivers. Then the inlet-based floodplain model was incorporated into the large-scale (WNAT-53K) computational mesh. In this study, applications of the 53K, WNAT- and inlet-based floodplain meshes are performed under different forcing implementations, involving astronomic tides, storm surge hydrographs and meteorological forcing (winds and pressures) in isolation (i.e., as the single forcing mechanism) and collectively (i.e., together in combination).

7.1 Conclusions

First, a 1.5-m floodplain mesh was constructed to allow for the overtopping of the river banks. This floodplain model was applied in an astronomic tide simulation to show improvement upon earlier model results which involved an in-bank-only hydrodynamic description. It is learned from these model intercomparisons that the floodplains become important towards modeling astronomic tides within the Pascagoula River. It is further concluded that a 1.5-m boundary is sufficient to capture any tidally driven storage because of the minimal tidal amplitudes within the Pascagoula River (less than 1 m).

Next, the inlet-based floodplain mesh is incorporated into the WNAT-53K model domain to produce a large-scale computational mesh that focuses on the local region of interest. The resulting large-scale modeling domain employs a refined coastline and has the barrier islands located along the Gulf Coast meshed over in order to allow for the wetting and drying of elements. Winds and pressures associated with Hurricane Katrina (August 23 to 30, 2005) are applied over the large-scale computational mesh which includes the high resolution of the Pascagoula River (FP1.5_WNAT). Model output is specified at points located along a 2.5-km-radius semi-circular arc (centered on the Pascagoula River inlet entrances) in order to examine storm surge hydrographs that will be used to drive a localized domain of the Pascagoula River. The WNAT-53K mesh is applied in a similar simulation (winds and pressures) to provide model output at the same arc points. The two model solutions (FP1.5_WNAT; WNAT-53K) are compared to one another to determine that the barrier islands can impact flow. For the WNAT-53K mesh, the barrier islands are defined with no-flow boundary constraints which allows the water to accumulate to greater heights (relative to those produced by the FP1.5_WNAT mesh) behind the barrier islands and up to the coastline. On other hand, the FP1.5_WNAT mesh allows for the wetting and drying of those elements, which permits for the storm surge to overtop the barrier islands and approach the coastline directly.

It is then demonstrated that a hydrograph generated by the FP1.5_WNAT mesh can be applied on the open-ocean boundary of the localized floodplain mesh (FP1.5_INLET) in order to produce results in the interior that are identical to those produced by the

FP1.5_WNAT mesh. Finally, the localized domain is tested by imposing the hydrograph boundary condition together with local winds and pressures.

When interested in storm surge levels along the Gulf Coast of the United States, a numerical model must describe the barrier islands with elements that are allowed to wet and dry (as opposed to using a no-flow boundary constraint). For when a localized domain is demanded, it is necessary to account not only for the local wind and pressure forcing, but also for the remote effects of the wind and pressure forcing. These remote effects of the meteorological forcings can only be captured by a large-scale model domain. The remote meteorological effect can be incorporated into a localized domain through a storm surge hydrograph that is calculated by a large-scale computational domain. The local winds and pressures together with the hydrograph boundary forcing (generated by a large domain) then become sufficient to drive the localized mesh.

7.2 Future Work

The tasks completed in this thesis have provided valuable guidance that will allow one to expand on the overall work regarding the calculation of storm tide elevations in the Pascagoula River. First, the maximum envelopes of water presented in Figure 6.18, Figure 6.29, and Figure 6.40 all indicate maximum water levels at the floodplain boundary of at least 1.75 m. With a 1.5-m floodplain boundary, water levels in excess of 1.5 m are not allowed to spill out further into the floodplain as would occur in reality. While the 1.5-m floodplain mesh is shown to be a vast improvement upon the in-bank mesh by allowing for the overtopping of the river banks, future work associated with this

project will need to focus on extending the inundation areas to the 5-m contour (Figure 7.1) to permit for the additional storage.

Second, freshwater river inflows are identified as the next hydrodynamic forcing to be introduced to the numerical model. The contribution of freshwater river inflows would increase the volume of accumulated storm surge within the Pascagoula River and adjacent floodplains, and also might affect the recession of the storm surge as the increased volume exits the system through the two inlets. Once knowledge is gained with respect to the inclusion of freshwater river inflows in the numerical model, then all long-wave components (i.e., astronomic tides; freshwater river inflows, local and remote meteorological effects) of the storm tide can be modeled together in a single simulation.

Ultimately, a recreation of the water levels caused by Hurricane Katrina would require a description of the wind-driven waves and their effect on the overall storm tide. Only until short-wave effects are combined (and interacting) with the long-wave components of the storm tide can one begin a true hindcast of the Hurricane Katrina water levels.

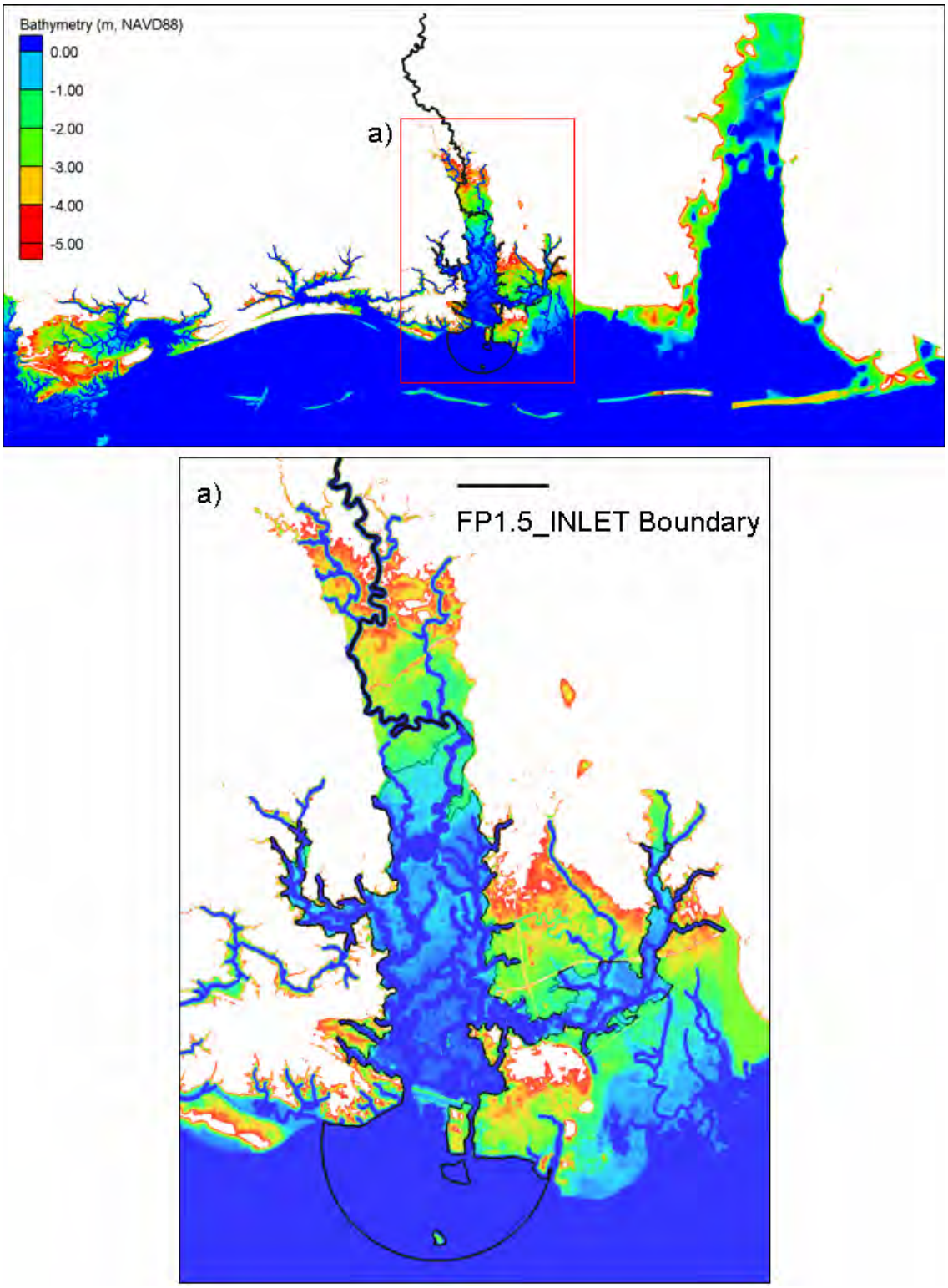

Figure 7.1 SL15: Up to 5.0 m above MSL Contours

APPENDIX A. SAFFIR SIMPSON HURRICANE SCALE

The Saffir-Simpson Hurricane Scale is a 1-5 rating based on the hurricane's present intensity. This is used to give an estimate of the potential property damage and flooding expected along the coast from a hurricane landfall. Wind speed is the determining factor in the scale, as storm surge values are highly dependent on the slope of the continental shelf and the shape of the coastline, in the landfall region. Note that all winds are using the U.S. 1-minute average.

Figure A.1 Saffir-Simpson Scale

Saffir-Simpson Scale

Category	Damage Level	Pressure (mbars)	Wind Speed (mph)	Surge (ft)
Tropical Discussion		--	< 39	--
Tropical Storm		--	39-73	--
1	Minimal	980 >	74-95	4-5
2	Moderate	965-980	96-110	6-8
3	Extensive	945-965	111-130	9-12
4	Extreme	920-945	131-155	13-18
5	Catastrophic	< 920	155 >	18 >

APPENDIX B. STORM SURGE HEIGHT DATA SET RECORDED BY THE SURVEY TEAM IN THE IMMEDIATE AFTERNOON OF HURRICANE KATRINA

Note: DT:damage trimline; MI:mudline inside; MO:mudline outside; RD:rafted debris; and TB:tree bark

No.	Location	Latitude	Longitude	Vertical survey (m)	Nature	Inland (m)	Date
1	AL Fort Morgan	30.23145	−87.95307	3.5	MO	74.5	Sept. 29, 2005
2	AL Fort Morgan	30.23283	−87.95338	3.5	MO	230.6	Sept. 29, 2005
3	AL Fort Morgan	30.23283	−87.95338	3.3	MI	230.6	Sept. 29, 2005
4	AL Fort Morgan	30.23374	−87.95312	3.3	RD	329.5	Sept. 29, 2005
5	AL Fort Morgan	30.23374	−87.95312	3.4	RD	329.5	Sept. 29, 2005
6	AL Fort Morgan	30.23374	−87.95312	3.4	RD	329.5	Sept. 29, 2005
7	AL Fort Morgan	30.23374	−87.95312	3.4	RD	329.5	Sept. 29, 2005
8	AL Fort Morgan	30.23374	−87.95312	3.1	RD	329.5	Sept. 29, 2005
9	AL Mobile	30.65569	−88.03317	3.8	RD	8.0	Oct. 5, 2005
10	AL Dauphin Island	30.25023	−88.15542	5.5	DT	0.0	Sept. 30, 2005
11	AL Dauphin Island	30.24932	−88.19169	3.3	DT	120.6	Sept. 30, 2005
12	AL Dauphin Island	30.25038	−88.18017	4.3	MI	151.0	Sept. 30, 2005
13	AL Camden	30.37195	−88.23352	4.9	TB	27.9	Oct. 4, 2005
14	MS West Ship Island	30.21213	−88.97209	9.2	RD	417.0	Oct. 1, 2005
15	MS West Ship Island	30.21230	−88.97227	5.6	MI	437.5	Oct. 1, 2005
16	MS West Ship Island	30.21262	−88.96632	6.7	RD	59.8	Oct. 1, 2005
17	MS East Ship Island	30.23470	−88.89082	5.5	TB	55.9	Oct. 1, 2005
18	MS East Ship Island	30.23517	−88.88997	6.7	TB	53.9	Oct. 1, 2005
19	MS East Ship Island	30.23585	−88.88815	8.1	TB	40.1	Oct. 1, 2005
20	MS East Ship Island	30.23584	−88.88831	7.7	TB	49.9	Oct. 1, 2005
21	MS East Ship Island	30.23591	−88.88845	6.6	TB	65.4	Oct. 1, 2005
22	MS East Ship Island	30.23663	−88.88674	8.2	TB	37.5	Oct. 1, 2005
23	MS East Ship Island	30.23735	−88.88557	7.0	TB	35.8	Oct. 1, 2005
24	MS East Ship Island	30.23735	−88.88557	7.2	TB	35.8	Oct. 1, 2005
25	MS East Ship Island	30.23622	−88.88956	8.0	TB	171.1	Oct. 1, 2005
26	MS Ocean Springs	30.38810	−88.79090	6.3	RD	0.0	Oct. 1, 2005
27	MS Ocean Springs	30.38882	−88.79118	7.1	TB	0.0	Oct. 1, 2005
28	MS Ocean Springs	30.38890	−88.79143	3.9	RD	0.0	Oct. 1, 2005
29	MS Lakeview	30.23828	−89.42984	8.2	DT	487.0	Oct. 2, 2005
30	MS Buccaneer State Park	30.26302	−89.40391	8.7	MO	233.8	Oct. 2, 2005
31	MS Buccaneer State Park	30.26302	−89.40391	8.6	DT	233.8	Oct. 2, 2005
32	MS Buccaneer State Park	30.26382	−89.40324	8.1	DT	247.5	Oct. 2, 2005
33	MS Buccaneer State Park	30.26569	−89.40468	7.5	RD	497.3	Oct. 2, 2005
34	MS Waveland	30.26440	−89.39262	8.4	TB	92.3	Oct. 2, 2005
35	MS Waveland	30.26494	−89.39298	9.4	RD	146.6	Oct. 2, 2005
36	MS Waveland	30.26891	−89.38410	9.1	DT	99.8	Oct. 2, 2005
37	MS Waveland	30.26899	−89.38372	10.1	RD	95.6	Oct. 2, 2005
38	MS Waveland	30.26904	−89.38396	7.3	RD	107.0	Oct. 2, 2005
39	MS Bay St. Louis	30.31867	−89.32418	8.5	DT	151.3	Oct. 2, 2005
40	MS Bay St. Louis	30.29215	−89.36561	7.6	MI	692.4	Oct. 2, 2005
41	MS Bay St. Louis	30.33974	−89.33723	6.4	RD	113.0	Oct. 2, 2005
42	MS Bay St. Louis	30.30623	−89.32839	9.3	RD	45.7	Oct. 2, 2005
43	MS Long Beach	30.35296	−89.13303	6.9	MI	201.4	Oct. 3, 2005
44	MS Long Beach	30.35046	−89.13714	7.0	DT	128.5	Oct. 3, 2005
45	MS Long Beach	30.35249	−89.14015	5.1	DT	494.8	Oct. 3, 2005
46	MS Long Beach	30.33904	−89.17281	7.7	TB	313.6	Oct. 3, 2005
47	MS Pass Christian	30.33334	−89.18897	7.2	DT	277.0	Oct. 3, 2005
48	MS Pass Christian	30.31534	−89.24503	7.2	DT	217.9	Oct. 3, 2005
49	MS Pass Christian	30.31534	−89.24503	7.1	MI	217.9	Oct. 3, 2005
50	MS Pass Christian	30.31732	−89.29047	7.1	TB	7.7	Oct. 3, 2005
No.	Location	Latitude	Longitude	Vertical survey (m)	Nature	Inland (m)	Date

No.	Location	Latitude	Longitude	Vertical survey (m)	Nature	Inland (m)	Date
51	MS Pass Christian	30.31732	−89.29047	7.5	TB	7.7	Oct. 3, 2005
52	MS Pass Christian	30.31655	−89.29003	7.6	TB	25.0	Oct. 3, 2005
53	MS Gulfport	30.36216	−89.10132	8.8	DT	0.0	Oct. 3, 2005
54	MS Gulfport	30.36034	−89.09424	6.0	DT	0.0	Oct. 4, 2005
55	MS Gulfport	30.36282	−89.09689	7.8	DT	405.4	Oct. 3, 2005
56	MS Gulfport	30.35162	−89.09016	8.4	DT	36.8	Oct. 4, 2005
57	MS Gulfport	30.35374	−89.09288	7.4	DT	0.0	Oct. 4, 2005
58	MS Gulfport	30.35639	−89.08685	9.7	DT	50.0	Oct. 4, 2005
59	MS Gulfport	30.36963	−89.08227	7.2	DT	154.9	Oct. 3, 2005
60	MS Biloxi	30.38934	−88.99214	6.9	DT	124.7	Oct. 3, 2005
61	MS Biloxi	30.39105	−88.97612	8.8	DT	57.9	Oct. 3, 2005
62	MS Biloxi	30.39055	−88.95620	8.5	DT	0.0	Oct. 3, 2005
63	MS Biloxi	30.39096	−88.95507	7.6	DT	0.0	Oct. 3, 2005
64	MS Biloxi	30.39067	−88.95586	8.5	DT	0.0	Oct. 3, 2005
65	MS Biloxi	30.39148	−88.89053	9.1	DT	0.0	Oct. 3, 2005
66	MS Biloxi	30.39161	−88.89362	10.4	DT	0.0	Nov. 18, 2005
67	MS Biloxi	30.39297	−88.87193	9.8	DT	86.1	Oct. 3, 2005
68	MS Biloxi	30.39305	−88.86223	7.2	DT	202.4	Oct. 3, 2005
69	MS Pascagoula	30.34175	−88.52238	6.3	DT	92.2	Oct. 4, 2005
70	MS Pascagoula	30.34425	−88.53822	5.8	DT	57.7	Oct. 4, 2005
71	MS Gautier	30.36112	−88.64513	5.2	MI	97.7	Oct. 4, 2005
72	MS Ocean Springs	30.40768	−88.84382	8.9	DT	379.0	Oct. 4, 2005
73	MS Ocean Springs	30.40429	−88.82331	6.4	DT	49.5	Oct. 4, 2005
74	MS Petit Bois Island	30.20505	−88.43348	3.9	RD	246.6	Feb. 3, 2006
75	MS Petit Bois Island	30.20419	−88.43345	4.6	RD	339.3	Feb. 3, 2006
76	MS Petit Bois Island	30.20419	−88.43345	4.7	TB	339.3	Feb. 3, 2006
77	MS Petit Bois Island	30.20457	−88.43240	3.8	TB	295.0	Feb. 3, 2006
78	MS Petit Bois Island	30.20295	−88.42802	3.8	TB	116.1	Feb. 3, 2006
79	MS Petit Bois Island	30.20386	−88.42663	4.9	TB	213.0	Feb. 3, 2006
80	MS Petit Bois Island	30.20386	−88.42663	4.6	TB	213.0	Feb. 3, 2006
81	MS Petit Bois Island	30.20404	−88.42659	4.3	TB	232.5	Feb. 3, 2006
82	MS Petit Bois Island	30.20404	−88.42659	4.4	TB	232.5	Feb. 3, 2006
83	MS Horn Island	30.22374	−88.59161	5.3	TB	192.0	Feb. 3, 2006
84	MS Horn Island	30.22374	−88.59161	5.5	TB	192.0	Feb. 3, 2006
85	MS Horn Island	30.22391	−88.59285	5.7	TB	232.1	Feb. 3, 2006
86	MS Horn Island	30.23431	−88.68197	4.4	RD	146.7	Nov. 18, 2005
87	MS Horn Island	30.23431	−88.68197	4.6	TB	146.7	Nov. 18, 2005
88	MS Horn Island	30.23247	−88.67136	3.4	RD	219.2	Nov. 18, 2005
89	MS Horn Island	30.23379	−88.66912	4.7	DT	465.1	Nov. 18, 2005
90	MS Cat Island	30.22568	−89.08950	6.6	DT	38.1	Jan. 20, 2006
91	MS Cat Island	30.22553	−89.08951	6.9	DT	16.1	Jan. 20, 2006
92	MS Cat Island	30.22513	−89.08777	5.6	RD	8.4	Jan. 20, 2006
93	MS Cat Island	30.22462	−89.08581	5.5	TB	7.9	Jan. 20, 2006
94	MS Cat Island	30.22462	−89.08581	5.6	TB	7.9	Jan. 20, 2006
95	MS Cat Island	30.22465	−89.08522	6.3	RD	17.9	Jan. 20, 2006
96	MS Cat Island	30.22487	−89.08524	6.9	RD	42.8	Jan. 20, 2006
97	MS Cat Island	30.22480	−89.08502	6.5	TB	39.5	Jan. 20, 2006
98	MS Cat Island	30.22508	−89.08528	6.7	RD	66.3	Jan. 20, 2006
99	MS Cat Island	30.22518	−89.08548	6.7	RD	81.0	Jan. 20, 2006
100	MS Cat Island	30.22560	−89.08530	5.9	RD	123.6	Jan. 20, 2006
No.	Location	Latitude	Longitude	Vertical survey (m)	Nature	Inland (m)	Date

No.	Location	Latitude	Longitude	Vertical survey (m)	Nature	Inland (m)	Date
101	MS Cat Island	30.22140	−89.07941	5.6	RD	131.6	Jan. 20, 2006
102	MS Cat Island	30.22219	−89.07888	5.2	RD	198.6	Jan. 20, 2006
103	MS Cat Island	30.22277	−89.07834	6.8	RD	185.1	Jan. 20, 2006
104	MS Cat Island	30.22277	−89.07834	5.9	TB	185.1	Jan. 20, 2006
105	FL Pensacola	30.32627	−87.17912	1.9	RD	139.0	Sept. 29, 2005
106	LA Venice	29.23837	−89.36441	4.0	MI		Oct. 26, 2005
107	LA Venice	29.24000	−89.36461	3.9	RD		Oct. 26, 2005
108	LA Venice	29.26331	−89.35313	4.2	DT	33.9	Oct. 26, 2005
109	LA Venice	29.28078	−89.36013	2.4	MO		Oct. 26, 2005
110	LA Venice	29.28060	−89.35936	3.2	MI		Oct. 26, 2005
111	LA Venice	29.28060	−89.35936	2.5	MO		Oct. 26, 2005
112	LA Buras	29.34838	−89.51062	1.6	MI		Oct. 26, 2005
113	LA Buras	29.34838	−89.51062	3.6	DT		Oct. 26, 2005
114	LA Buras	29.34932	−89.52148	4.0	RD		Oct. 26, 2005
115	LA Empire	29.36657	−89.56668	5.7	MI		Oct. 26, 2005
116	LA Empire	29.38621	−89.59976	5.0	MI		Oct. 26, 2005
117	LA Port Sulphur	29.47964	−89.69441	5.0	MI		Oct. 26, 2005
118	LA Port Sulphur	29.47964	−89.69441	5.5	MO		Oct. 26, 2005
119	LA Port Sulphur	29.49802	−89.71313	5.3	TB		Oct. 26, 2005
120	LA Port Sulphur	29.49802	−89.71313	5.5	TB		Oct. 26, 2005
121	LA Shell Beach	29.85480	−89.67839	6.9	TB	35.8	Oct. 26, 2005
122	LA Shell Beach	29.85179	−89.68067	5.6	RD		Oct. 26, 2005
123	LA Shell Beach	29.85125	−89.67990	6.5	DT		Oct. 26, 2005
124	LA Shell Beach	29.85191	−89.68013	6.3	TB		Oct. 26, 2005
125	LA Shell Beach	29.85376	−89.67760	6.9	DT		Oct. 26, 2005
126	LA Chef Menteur Pass, NO	30.06716	-89.80640	5.2	MI	20.7	Oct. 27, 2005
127	LA Chef Menteur Pass, NO	30.06600	−89.80501	5.7	DT		Oct. 27, 2005
128	LA Chef Menteur Pass, NO	30.06565	−89.80435	5.3	DT		Oct. 27, 2005
129	LA Chef Menteur Pass, NO	30.06565	−89.80435	4.8	RD		Oct. 27, 2005
130	LA Chef Menteur Pass, NO	30.06900	−89.80858	5.2	DT		Oct. 27, 2005
131	LA Chef Menteur Pass, NO	30.07243	−89.83909	4.6	DT	46.6	Oct. 27, 2005
132	LA Irish Bayou Canal, NO	30.13497	−89.86595	4.5	DT		Oct. 27, 2005
133	LA Irish Bayou Canal, NO	30.14410	−89.86195	4.2	DT		Oct. 27, 2005
134	LA Lake St. Catherine Marina, NO	30.14960	−89.74075	5.1	DT	17.9	Oct. 5, 2005
135	LA Lake St. Catherine Marina, NO	30.16253	−89.73963	4.4	DT	56.0	Oct. 5, 2005
136	LA Slidell	30.19652	−89.75541	4.7	DT		Oct. 5, 2005
137	LA Slidell	30.19891	−89.75461	4.8	DT		Oct. 5, 2005
138	LA Slidell	30.21831	−89.82354	4.8	DT		Oct. 27, 2005
139	LA Slidell	30.21934	−89.82248	5.1	DT		Oct. 27, 2005
140	LA Lacombe	30.26518	−89.95647	2.7	MI		Oct. 27, 2005
141	LA Lacombe	30.28161	−89.95373	3.1	DT		Oct. 27, 2005
142	LA Mandeville	30.34974	−90.06025	3.2	DT	75.3	Oct. 27, 2005
143	LA Mandeville	30.35381	−90.07047	3.4	DT	0.0	Oct. 27, 2005
144	LA Madisonville	30.38273	−90.15940	2.8	DT		Oct. 27, 2005
145	LA Wallace Landing	30.40588	−90.26198	1.6	MO		Oct. 27, 2005
146	LA Galva	30.28132	−90.40018	1.6	RD		Oct. 27, 2005
147	LA Laplace	30.10677	−90.42276	2.4	MO		Oct. 27, 2005
148	LA Kenner	30.03944	−90.23476	2.9	DT	32.1	Oct. 27, 2005
149	LA Lakeshore, NO	30.02663	−90.11218	4.8	RD	36.9	Oct. 27, 2005
150	LA Lakeshore, NO	30.02649	−90.11207	4.0	RD	55.9	Oct. 27, 2005
151	LA Lakeshore, NO	30.02619	−90.11184	4.5	RD	95.7	Oct. 27, 2005
152	LA Grand Isle	29.26381	−89.95533	1.8	RD		Oct. 28, 2005
153	LA Grand Isle	29.26335	−89.95725	2.4	DT		Oct. 28, 2005
No.	Location	Latitude	Longitude	Vertical survey (m)	Nature	Inland (m)	Date

APPENDIX C. TIDAL CONSTITUENTS EMPLOYED BY ADCIRC-2DDI

Table C.1 23 Tidal constituents applied in ADCIRC harmonic analysis

Constituent	Description	Frequency (rad/s)	Degrees per solar hour
STEADY	Principal water level	0.000000000000000	0.0000
MN4	Lunar monthly constituent	0.000000420111582	0.5445
SM	Lunisolar synodic fortnightly constituent	0.000000783620452	1.0156
O1	Lunar diurnal constituent	0.000010756574418	13.9405
K1	Lunar diurnal constituent	0.000011608900776	15.0451
MNS2	Arising from interaction between MN and S2	0.000021159184779	27.4223
2MS2	Variational constituent	0.000021593421780	27.9851
N2	Larger lunar elliptic semi-diurnal constituent	0.000021962189894	28.4630
M2	Principal lunar semi-diurnal constituent	0.000022343772344	28.9575
2MN2	Smaller lunar elliptic semi-diurnal constituent	0.000022783610382	29.5276
S2	Principal solar semi-diurnal constituent	0.000023148148148	30.0000
2SM2	Shallow-water semi-diurnal constituent	0.000023913376186	30.9917
MN4	Shallow-water quarter diurnal constituent	0.000044345111395	57.4713
M4	Shawllow-water overtides of principal lunar constituent	0.000044687544688	57.9151
MS4	Shallow-water quarter diurnal constituent	0.000045567220764	59.0551
2MN6	Shallow-water twelfth diurnal constituent	0.000066517667092	86.2069
M6	Shawllow-water overtides of principal lunar constituent	0.000066902162278	86.7052
MSN6	Arising from interaction between M2, N2 and S2	0.000067291128338	87.2093
M8	Shallow-water eighth diurnal constituent	0.000089721504450	116.2791
M10	Shallow-water tenth diurnal constituent	0.000111289173789	144.2308
P1	Solar diurnal constituent	0.000011539455707	14.9551
K2	Lunisolar semi-diurnal constituent	0.000025777447826	33.4076
Q1	Larger lunar elliptic diurnal constituent	0.000010333994709	13.3929

Table C.2 37 Tidal constituents used in the resynthesis of the historical tidal records for the NOS stations.

Constituent	Tidal species	Frequency (rad/s)	Degrees per solar hour
SA	long-period	0.000000199106190	0.2580
SSA	long-period	0.000000398212870	0.5161
MM	long-period	0.000002639203000	3.4204
MSF	long-period	0.000004925201800	6.3831
MF	long-period	0.000005323414700	6.8991
2Q1	diurnal	0.000062319338000	80.7659
Q1	diurnal	0.000064958541000	84.1863
RHO1	diurnal	0.000065311745000	84.6440
O1	diurnal	0.000067597744000	87.6067
M1	diurnal	0.000070281955000	91.0854
P1	diurnal	0.000072522946000	93.9897
S1	diurnal	0.000072722052000	94.2478
K1	diurnal	0.000072921158000	94.5058
J1	diurnal	0.000075560361000	97.9262
OO1	diurnal	0.000078244573000	101.4050
2N2	semi-diurnal	0.000135240500000	175.2717
MU2	semi-diurnal	0.000135593700000	175.7294
N2	semi-diurnal	0.000137879700000	178.6921
NU2	semi-diurnal	0.000138232900000	179.1498
M2	semi-diurnal	0.000140518900000	182.1125
LDA2	semi-diurnal	0.000142804900000	185.0752
L2	semi-diurnal	0.000143158110000	185.5329
T2	semi-diurnal	0.000145245010000	188.2375
S2	semi-diurnal	0.000145444100000	188.4956
R2	semi-diurnal	0.000145643200000	188.7536
K2	semi-diurnal	0.000145842320000	189.0116
2SM2	semi-diurnal	0.000150369310000	194.8786
2MK3	terdiurnal	0.000208116650000	269.7192
M3	terdiurnal	0.000210778350000	273.1687
MK3	terdiurnal	0.000213440060000	276.6183
MN4	fourth-diurnal	0.000278398600000	360.8046
M4	fourth-diurnal	0.000281037810000	364.2250
MS4	fourth-diurnal	0.000285963010000	370.6081
S4	fourth-diurnal	0.000290888210000	376.9911
M6	sixth-diurnal	0.000421556710000	546.3375

Constituent	Tidal species	Frequency (rad/s)	Degrees per solar hour
S6	sixth-diurnal	0.000436332310000	565.4867
M8	eighth-diurnal	0.000562075610000	728.4500

Table C.3 35 Tidal constituents at the USGS stations extracted by T_TIDE

Constituent	Tidal species	Frequency (rad/s)	Degrees per solar hour
MM	long-period	0.000002639286895	3.4205
MSF	long-period	0.000004925144616	6.3830
ALP1	diurnal	0.000060033392149	77.8033
2Q1	diurnal	0.000062319424403	80.7660
Q1	diurnal	0.000064958536765	84.1863
O1	diurnal	0.000067597823660	87.6068
NO1	diurnal	0.000070281965517	91.0854
K1	diurnal	0.000072921077879	94.5057
J1	diurnal	0.000075560364774	97.9262
OO1	diurnal	0.000078244506630	101.4049
UPS1	diurnal	0.000080883793525	104.8254
EPS2	semi-diurnal	0.000132954470028	172.3090
MU2	semi-diurnal	0.000135593756923	175.7295
N2	semi-diurnal	0.000137879614644	178.6920
M2	semi-diurnal	0.000140518901539	182.1125
L2	semi-diurnal	0.000143158188434	185.5330
S2	semi-diurnal	0.000145444046155	188.4955
ETA2	semi-diurnal	0.000148481442652	192.4319
MO3	terdiurnal	0.000208116725199	269.7193
M3	terdiurnal	0.000210778352309	273.1687
MK3	terdiurnal	0.000213439979418	276.6182
SK3	terdiurnal	0.000218365298567	283.0014
MN4	fourth-diurnal	0.000278398516183	360.8045
M4	fourth-diurnal	0.000281037803078	364.2250
SN4	fourth-diurnal	0.000283323835332	367.1877
MS4	fourth-diurnal	0.000285962947694	370.6080
S4	fourth-diurnal	0.000290888266843	376.9912
2MK5	fifth-diurnal	0.000353958880957	458.7307
2SK5	fifth-diurnal	0.000363809344722	471.4969
2MN6	sixth-diurnal	0.000418917592255	542.9172
M6	sixth-diurnal	0.000421556704617	546.3375
2MS6	sixth-diurnal	0.000426481849233	552.7205
2SM6	sixth-diurnal	0.000431407168382	559.1037
3MK7	seventh-diurnal	0.000494477782496	640.8432
M8	eighth-diurnal	0.000562075606156	728.4500

APPENDIX D. ADCIRC-2DDI INPUT FILE: SINGLE METROLOGICAL INPUT FILE (FORT.22) USED FOR WNAT-53K MESH DOMAIN (TOTAL COMPUTATINAL NODES: 52774)

Table 7.1 Legend for Fort.22

Parameter name	**JN**	**WSX,**	**WSY**	**PRN**
Definition	Node number	Applied horizontal wind stress in the x, y directions divided by the reference density of water		Applied atmospheric pressure at the free surface.
Unit	Dimensionless	m/s	m/s	mb

pmin= 985. v = 32.22(m/s)

....begining of fort.22

```
    1 -0.25688E-04  0.24949E-04  0.10025E+02
    2 -0.26035E-04  0.25231E-04  0.10025E+02
    3 -0.26384E-04  0.25515E-04  0.10025E+02
    4 -0.26737E-04  0.25800E-04  0.10025E+02
    5 -0.27092E-04  0.26088E-04  0.10025E+02
    6 -0.27450E-04  0.26378E-04  0.10025E+02
    7 -0.27812E-04  0.26669E-04  0.10025E+02
    8 -0.28176E-04  0.26963E-04  0.10025E+02
    9 -0.28542E-04  0.27258E-04  0.10025E+02
   10 -0.28906E-04  0.27551E-04  0.10025E+02
   11 -0.29273E-04  0.27846E-04  0.10025E+02
   12 -0.29642E-04  0.28142E-04  0.10025E+02
   13 -0.30014E-04  0.28441E-04  0.10025E+02
   14 -0.30433E-04  0.28777E-04  0.10025E+02
   15 -0.30855E-04  0.29115E-04  0.10025E+02
```

....This portion of the input has been eliminated

```
52747  0.83155E-04  0.31627E-04  0.10003E+02
52748  0.83700E-04  0.31223E-04  0.10002E+02
52749  0.84466E-04  0.31158E-04  0.10002E+02
52750  0.85392E-04  0.31298E-04  0.10002E+02
52751  0.86290E-04  0.31688E-04  0.10002E+02
52752  0.86990E-04  0.31348E-04  0.10002E+02
52753  0.87738E-04  0.31488E-04  0.10002E+02
52754  0.88500E-04  0.31635E-04  0.10002E+02
52755  0.89278E-04  0.31794E-04  0.10002E+02
52756  0.90068E-04  0.32046E-04  0.10001E+02
52757  0.90812E-04  0.32408E-04  0.10001E+02
52758  0.91147E-04  0.33027E-04  0.10001E+02
52759  0.91586E-04  0.33194E-04  0.10001E+02
52760  0.82527E-04  0.32941E-04  0.10003E+02
52761  0.82101E-04  0.32597E-04  0.10003E+02
52762  0.82222E-04  0.32085E-04  0.10003E+02
52763  0.82302E-04  0.31557E-04  0.10003E+02
52764  0.82571E-04  0.31106E-04  0.10003E+02
52765  0.83026E-04  0.30795E-04  0.10003E+02
52766  0.83557E-04  0.30564E-04  0.10002E+02
52767  0.84184E-04  0.30483E-04  0.10002E+02
52768  0.84867E-04  0.30639E-04  0.10002E+02
52769  0.85547E-04  0.30942E-04  0.10002E+02
52770  0.86256E-04  0.31200E-04  0.10002E+02
52771  0.82024E-04  0.33130E-04  0.10003E+02
52772  0.82173E-04  0.33293E-04  0.10003E+02
52773  0.81989E-04  0.33671E-04  0.10003E+02
52774  0.82276E-04  0.33785E-04  0.10003E+02
```

....End of fort.22

LIST OF REFERENCES

Bacopoulos, P. (2006).
"Analysis, modeling, and simulation of the tides in the Loxahatchee River estuary (Southeastern Florida)." University of Central Florida, Orlando, FL. Master's Thesis.

Bacopoulos, P., Y. Funakoshi, S. C. Hagen, A. T Cox, and V. J. Cardone (2008).
"The role of meteorological forcing on the St. Johns River (Northeastern Florida)." Journal of Hydrology (in press).

Blain, C. A., J. J. Westerink, and R. A. Jr. Luettich, (1994).
"The influence of domain size on the response characteristics of a hurricane storm surge model." Journal of Geophysical Research 99(C9): 18467-18479.

Blain, C. A., J. J. Westerink, and R. A. Jr. Luettich, (1998).
"Grid convergence studies for the prediction of hurricane storm surge." International Journal for Numerical Methods in Fluids 26: 369-401.

Bode, L. and T. A. Hardy (1997).
"Progress and recent developments in storm surge modeling." Journal of Hydraulic Engineering 123(4): 315-331.

Ceyhan, E., P. Basuchowdhuri, T. Judeh, S. Ou, B. Estrade, and T. Kosar (2007).
"Towards a faster and improved ADCIRC (ADvanced Multi-Dimensional CIRCulation) model." Journal of Coastal Research, Special Issue 50

Chen, Q., L. Wang, H. Zhao, and S. L. Douglass (2007).
"Prediction of Storm Surges and Wind Waves on Coastal Highways in Hurricane-Prone Areas." Journal of Coastal Research 23(5): 1304-1317

Department of the Army; U.S. Army Corps of Engineers (2007).
"Intent to prepare a draft supplemental environmental impact statement to evaluate construction of authorized improvements to the federal Pascagoula Harbor navigation project in Jackson County, MS."

Dietsche, D., S. C. Hagen, and P. Bacopoulos (2007).
"Storm surge simulations for Hurricane Hugo (1989): On the significance of inundation areas." Journal of Waterway, Port, Coastal, and Ocean Engineering 133(3): 183-191.

Droppo, Ian G. (2003).
"Preserving the Pascagoula: D.G. Schueler." University Press of Mississippi.

Fritza, H. M., C. Blounta, R. Sokoloskia, J. Singletona, A. Fuggleb, B.G. McAdooc, A. Moored, C. Grassa and B. Tate (2007).
"Hurricane Katrina storm surge distribution and field observations on the Mississippi Barrier Islands Estuarine." Coastal and Shelf Science 74(1-2): 12-20

Funakoshi, Y. (2006).
"Coupling of hydrodynamic and wave models for storm tide simulations: A case study for Hurricane Floyd (1999)." University of Central Florida. Orlando, FL. Ph.D. Dissertation.

Graber, H. C., V. J. Cardone, R. E. Jensen, D. N. Slinn, S. C. Hagen, A. T. Cox, M. D. Powell, and C. Grassl (2006).
"Coastal forecasts and storm surge predictions for tropical cyclones: A timely partnership program." Oceanography 19(1): 130-141.

Hagen, S. C. and D. M Parrish (2004).
"Meshing requirements for tidal modeling in the western North Atlantic." International Journal of Computational Fluid Dynamics 18(7): 585-595.

Hagen, S. C., J. J. Westerink, et al. (2000).
"One-dimensional finite element grids based on a localized truncation error analysis." International Journal for Numerical Methods in Fluids 32: 241-261.

Hagen, S. C., J. J. Westerink, et al. (2001).
"Two-dimensional, unstructured mesh generation for tidal models." International Journal for Numerical Methods in Fluids 35: 669-686.

Hagen, S.C., A.K. Zundel, et al. (2006).
"Automatic, Unstructured Mesh Generation for Tidal Calculations in a Large Domain." International Journal of Computational Fluid Dynamics 20(8): 593-608.

IPET Force - U.S. Army Corps. of Engineers (2007).
"Performance evaluation of the New Orleans and Southeast Louisiana Hurricane Protection System." Vicksburg, MS.

Kohut, J. T., S. M. Glenn, and J. D. Paduan, (2006).
"Inner shelf response to Tropical Storm Floyd." Journal of Geophysical Research 111(C09S91): 1-18.

Kolar, R. L., W. G. Gray, et al. (1994).
"Shallow water modeling in spherical coordinates: Equation formulation, numerical implementation, and application." Journal of Hydraulic Research 32(1): 3-24.

Kolar, R. L., J. J. Westerink, et al. (1994).

"Aspects of non-linear simulations using shallow water models based on the wave continuity equation." Computers and Fluids 23(3): 523-538.

Luettich, R. A. Jr. and J. J Westerink (2000).
"ADCIRC: A (parallel) advanced circulation model for oceanic, coastal and estuarine waters." Users manual,
http://www.marine.unc.edu/C_CATS/adcirc/adcirc.htm.

Luettich, R.A., S.D. Carr, et al. (2002).
"Semi-diurnal seiching in a shallow, micro-tidal lagoonal estuary." Continental Shelf Research 22: 1669-1681.

Massey, W. G., J. W. Gangai, E. Drei-Horgan, and K. J. Slover (2007).
"History of Coastal Inundation Models." Marine Technology Society Journal 41(1): 7-17

Mossa, J. and D. Coley (2004).
"Planform charge rates in rivers with and without instream and floodplain sand and gravel mining: Assessing instability in the Pascagoula River and Tributaries, Mississippi." Gainesville, FL, University of Florida.

Murray, R. R. (2003).
"A sensitivity analysis for a tidally-influenced riverine system." University of Central Florida. Orlando, FL. Master's Thesis.

Oldham, M. B. Jr. and J. W. Rushing (1970).
"Water resuorces planning for Pascagoula Basin." Journal of the Waterways and Harbors Division, Proceedings of the America Society of Civil Engineers 96(WW1): 65-85.

Parrish, D. M. (2001).
"Development of a tidal constituent database for the St. Johns River Water Management District." University of Central Florida. Orlando, FL. Master's Thesis.

Parrish, D.M. and S. C. Hagen (2007).
"2D, unstructured mesh generation for oceanic and coastal tidal models from a localized truncation error analysis with complex derivatives." International Journal of Computational Fluid Dynamics 21(7&8): 277-296.

Pascagoula Harbor (1997).
"Pascagoula Harbour, Mississippi - condition of improvement on 30 September 1997."

Pawlowicz, R., B. Beardsley, et al. (2002).

"Classical tidal harmonic analysis including error estimates in MATLAB using T_TIDE." Computers and Geosciences 28: 929-937.

Peng, M., L. Xie, and L. J. Pietrafesa, (2006).
"A numerical study on hurricane-induced storm surge and inundation in Charleston Harbor, South Carolina." Journal of Geophysical Research 111(C8): 1-22.

Reid, R. O. (1990).
"Waterlevel changes, tides and storm surges." Handbook of Ciastal and Ocean Engineering. Pulisher. Houston, Texas, J. Herbich.

Reid, R. O. and B. R. Bodine (1968).
"Numerical Model for Storm Surges in Galveston Bay," American Society of Civil Engineers: Journal of the Harbors and harbors Division 94(WW1): 33-57.

Salisbury, M. B. and S. C. Hagen (2007).
"The Effect of Tidal Inlets on Open Coast Storm Surge Hydrographs." Coastal Engineering 54: 377-391.

Shen, J., H.Wang, M. Sisson, and W. Gong (2006).
"Storm tide simulation in the Chesapeake Bay using an unstructured grid model." Estuarine, Coastal and Shelf Science 68:1-16.

Shen, J, K. Zhang, C. Xiao, and W. Gong (2006).
"Improved Prediction of Storm Surge Inundation with a High-Resolution Unstructured Grid Model." Journal of Coastal Research 22(6): 1309-1319

Smith, J. M. (2006).
"Modeling Nearshore Waves for Hurricane Katrina" 9th Internatinal Workshop on Wave hindcasting and forecasting, Victoria, B.C., Canada.

The Port of Pascagoula. (2008).
"The history of the Port of Pascagoula."
Retrieved May 13th, 2008 from http://www.portofpascagoula.com/.

Turnipseed, D. P. and J. B. Storm (1995).
"Streamflow characteristics of the Lower Pascagoula River, Mississippi." Proceedings of the Twenth-fifth Mississippi Water Resources Conference, Jaskson, MS.

U.S. Army Corps of Engineers (1968).
"Pascagoula River comprehensive basin study." Mobile, Alabama.

Valle-Levinson, A., K. C.Wong, and K. T. Bosley (2002).

"Response of the lower Chesapeake Bay to forcing from Hurricane Floyd." Continental Shelf Research 22: 1715-1729.

Veeramony, J. and C.A. Blain (2001).
"Barotropic flow in the vicinity of an idealized inlet – Simulations with the ADCIRC model." Washington, D.C., Naval Research Laboratory.

Walters, R. A. and R. T. Cheng (1979).
"A two-dimensional hydrodynamic model of a tidal estuary." Advances in Water Resources 2: 177-184.

Wang, Qing (2008).
"Finite element modeling of tides and currents of the Pascagoula River." MS thesis, University of Central Florida, Orlando, Florida.

Warner, J. C., W. R. Geyer, et al. (2005).
"Numerical modeling of an estuary: A comprehensive skill assessment." Journal of Geophysical Research-Oceans 110(C5): 1-13.

Westerink, J. J., C. A. Blain, et al. (1994).
"ADCIRC: An advanced three-dimensional circulation model for shelves, coasts, and estuaries, II: User's manual for ADCIRC-2DDI. Technical Report DRP-92-6." U.S. Army Corps of Engineers, Waterways Experiment Station, Vicksburg, Mississippi.

Westerink, J. J., R. A. Jr. Luettich, et al. (1994).
"Modeling tides in the western North Atlantic using unstructured graded grids." Tellus 46A: 178-199.

Westerink, J. J., R. A. Tr. Luettich, A. M. Baptista, N. W. Scheffner, and P. Farrar (1992).
"Tide and storm surge predictions using finite element model." Journal of Hydraulic Engineering 118: 1373-1390.

Westerink et al. (2004).
"A New Generation Hurricane Storm Surge Model for Southern Louisiana" ADCIRC Development Group Publications.

Wright, J. (2000).
"Waves, tides and shallow-water processes." Butterworth-Heinemann/Open University, Oxford, UK.